PARKINSON, Claire Lucille, 1948-
A NUMERICAL SIMULATION OF THE ANNUAL CYCLE OF SEA ICE IN THE ARCTIC AND ANTARCTIC.

The Ohio State University,
Ph.D., 1977
Physical Geography

University Microfilms International, Ann Arbor, Michigan 48106

A NUMERICAL SIMULATION OF THE ANNUAL CYCLE

OF SEA ICE IN THE ARCTIC AND ANTARCTIC

DISSERTATION

Presented in Partial Fulfillment of the Requirements for

the Degree Doctor of Philosophy in the Graduate

School of The Ohio State University

By

Claire Lucille Parkinson, B.A., M.A.

* * * * *

The Ohio State University

1977

Reading Committee:

A. John Arnfield
John N. Rayner
Edward J. Taaffe
Warren M. Washington

Approved By

Adviser
Department of Geography

ACKNOWLEDGEMENTS

The work reported here was carried out at the National Center for Atmospheric Research (NCAR) under a National Science Foundation grant (NSF grant #ATM76-08492) through The Ohio State University. I gratefully acknowledge the financial support of NSF and the research support of many departments of the NCAR staff, including the computing facility, the Graphics Department, the Publications Office, the Print Shop, the Photographics Department, and the library staff.

Individually, my prime acknowledgement goes to my supervisor at NCAR, Warren M. Washington. He contributed to the construction of the model, provided much encouragement throughout, and was always available for comments and suggestions. I also thank my thesis adviser, Professor John N. Rayner, for encouraging me to visit NCAR, for helping to obtain funding from NSF, and for offering comments at various stages of the project.

Many other people contributed to the final output. A. John Arnfield, Thomas Mayer, and Elmer Armstrong provided useful comments on the manuscript, while Ellen Thompson, Harry van Loon, and John Walsh are all thanked for numerous scientific

discussions and much encouragement. Ellen is further thanked for frequently sending material from Ohio State, Harry for his suggestions on data sources, and John for the loan of his unpublished work on Arctic ice drift.

I also thank Albert Semtner, Jr. for use of his thermodynamic model, which was the initial base for this work; Ann Modahl for much secretarial assistance throughout my stay at NCAR; Roy Jenne for providing access to magnetic tapes of atmospheric data; Arnold Gordon for maps of the dynamic topography of the Southern Ocean; Louise Morrison for aid with the initial programming; Gerald Meehl for contributing, along with the NCAR Graphics Department, to the drafting of the diagrams; and Ruby Fulk for typing the final manuscript. In addition I feel I benefitted from conversations with James Deardorff, William Kellogg, Igor Kulakov, Eric Leavitt, Gary Maykut, Thomas Seliga, Lonnie Thompson, and Norbert Untersteiner. Finally, I sincerely thank George Demko and Gloria Williamson for their moral support, and I both thank and apologize to any contributor who has not yet been mentioned.

VITA

March 21, 1948 . . . . Born - Bay Shore, New York

1970 . . . . B.A., Department of Mathematics, Wellesley College, Wellesley, Massachusetts

1970-1972 . . . . Counselor-Tutor, Burlington Probation Department, Burlington, Vermont

1973-1976 . . . . Teaching Assistant, Department of Geography, The Ohio State University, Columbus, Ohio

1974 . . . . M.A., Department of Geography, The Ohio State University, Columbus, Ohio

1976-1977 . . . . Research Assistant, National Center for Atmospheric Research, Boulder, Colorado

PUBLICATIONS

Harton, L., Jr., C. L. Parkinson, and L. Brown, 1974: *Annotated Bibliography of Geographic Diffusion Studies,* Studies in the Diffusion of Innovations, Discussion Paper No. 11, Department of Geography, The Ohio State University, 44pp.

Hughes, T., C. Parkinson, and H. Brecher, 1974: Ice dynamics study of a glacial surge induced by the August 1970 eruption on Deception Island, Antarctica. *Proceedings of the Symposium on Andean and Antarctic Volcanology Problems,* Santiago, Chile, September 1974. International Association of Volcanology and Chemistry of the Earth's Interior, 112-133.

Parkinson, C., 1973: Ambivalence in alternating symmetric groups. *The American Mathematical Monthly,* 80, 190-192.

Parkinson, C. L. and W. M. Washington, 1977: Summary of a large-scale sea-ice model. *A Symposium on Sea Ice Processes and Models, September 6-9, 1977,* vol. II, University of Washington, Seattle, 128-136.

Washington, W. M., A. J. Semtner, Jr., C. L. Parkinson, and L. Morrison, 1976: On the development of a seasonal change sea-ice model. *Journal of Physical Oceanography,* 6, 679-685.

TABLE OF CONTENTS

Page

LIST OF TABLES

LIST OF FIGURES

FIGURE Page

FIGURE		Page
22	Simulated half-yearly cycle of sea ice in the Arctic, July-December. Contours show ice thickness in meters, while shading indicates ice compactness above 90%	99
23	Simulated half-yearly cycle of sea ice in the Antarctic, January-June. Contours show ice thickness in meters, while shading indicates ice compactness above 90%	100
24	Simulated half-yearly cycle of sea ice in the Antarctic, July-December. Contours show ice thickness in meters, while shading indicates ice compactness above 90%	101
25	Satellite-observed Antarctic sea ice extents for the months October and December of 1967 and 1968. Abbreviated and redrawn from Budd (1975, p. 421)	105
26	Arctic ice boundaries off northern Alaska, September 1-5, for four separate years. The 1953, 1954, and 1955 edges are from Winchester and Bates (1958, p. 332); the 1968 edge is from J. Walsh (personal communication, 1976)	107
27	Ice borders around Spitsbergen in August for the five years 1957, 1958, 1960, 1961, and 1962. Abbreviated and redrawn from Blindheim and Ljoen (1972, p. 40)	107
28	Simulated contours of ice concentration (%) in the Arctic, March and September . . .	115
29	Simulated contours of ice concentration (%) in the Antarctic, March and August	116
30	Simulated Arctic ice drift for January and July	119
31	Simulated Antarctic ice drift for January and July	120
32	Schematic diagram of the major observed features of Arctic ice drift	121
33	January and July ice thicknesses for the first four years of the Arctic simulation . .	124

FIGURE | Page

CHAPTER I

INTRODUCTION

Sea ice covers roughly 7% of the earth's oceans and its extent shows large variations both seasonally and interannually. However, although interest has intensified recently, there has been far less research on sea ice than on many other physical phenomena of comparable geographic extent. Of particular importance here, only limited attempts have been made to insert ice interactively into large-scale atmospheric or oceanic numerical models. The purpose of this thesis is to construct a large-scale model of both Arctic and Antarctic sea ice which will be suitable for eventual coupling with general circulation models of the atmosphere and/or oceans.

The presence of ice in the Arctic and Antarctic engenders numerous climatic consequences. For instance, the ice cover creates a winter climate closer to that of continental ice sheets than to other marine environments. One prominent effect of this is the reduced absorption of solar radiation: with an ice cover, only 30-50% of the incident shortwave radiation is absorbed, while without the ice, this percentage range would rise to 85-95%. Although part of the reflected radiation does help warm the atmosphere, the largest portion passes through, thereby becoming lost to the earth-atmosphere system. Hence the ice reduces the availability of shortwave radiative energy to the polar regions.

Another prominent effect of the ice is the significant lessening of heat transfer between ocean and atmosphere, the slow process of molecular conduction being the primary transfer mechanism through the ice cover. Since the oceans have a large heat storage capacity and the temperature contrast between ocean and atmosphere can be great, the effects of this relative thermal insulation are significant. In the Arctic winter, air temperatures vary roughly from $-20^{o}C$ to $-40^{o}C$, while water temperatures vary from $-1^{o}C$ to $-2^{o}C$. The magnitude of this contrast creates a heat transfer of 10^2 to 10^3 W m^{-2} from the ocean to the atmosphere wherever the two meet directly (Lindsay, 1976), but where direct contact is prevented by 1 or 2 meters of ice this heat transfer reduces to only 10 to 20 W m^{-2} (Fletcher, 1969). This suggests that the ice cover strengthens the net polar atmospheric cooling in winter, creating larger average temperature gradients from pole to equator and leading to a more intense general circulation. However, the stronger circulation might then advect more warm air into the polar regions, with the negative feedback of increasing polar atmospheric temperatures and reducing equatorward gradients. Hence the net overall effect not only on the large-scale circulation but also on the polar temperatures remains uncertain.

In summer, the insulating effect of the ice reduces sensible heat transfer from atmosphere to ocean rather than *vice versa*. This combined with the albedo effect greatly suppresses summer heat gain by the polar oceans (Fletcher, 1969).

Another consequence of the ice is the lessened evaporative transfer to the atmosphere and the resultant reduction of moisture available for cloud formation, rain, or snow. Should the Arctic ice melt, the increased evaporation could reasonably be expected to increase snowfall not only over the Arctic Ocean itself but over all surrounding land areas. This reasoning plays a major role in the Ewing and Donn (1956) theory of ice ages, a northern-hemisphere glaciation being presumed a likely consequence of an ice-free Arctic. On the other hand, evidence suggests that the Arctic has not been ice-free at any time during the past 150,000 years (Ku and Broecker, 1967), and alternate theories to that of Ewing and Donn hypothesize increased sea ice coverage in the Arctic during widespread glaciation rather than decreased coverage (e.g., Brooks, 1949; Mercer, 1970). Muller (1972) presents a review of objections to the Ewing and Donn theory.

It is hardly necessary though to consider the extremes of ice *versus* no ice or to decide on actual sea ice extents in the past before recognizing at least the potential of a strong influence on climate from variations in global sea ice extent. Such variations are frequently mentioned as likely candidates for causal mechanisms producing large-scale climatic change (Brooks, 1949; Ewing and Donn, 1956, 1958; Wilson, 1964; Donn and Shaw, 1966; Budyko, 1972; Fletcher, 1969). Although most of these theories stress sea ice in the Arctic, Wilson (1964) hypothesizes that a northern-hemisphere ice age could be triggered by the formation of an extended ice shelf around Antarctica.

On smaller time scales, yearly variations in ice extent have been correlated with storm tracks and midlatitude rainfall patterns in the northern hemisphere (Zubov, 1944; Brooks, 1949; Lamb, 1966), and increased winter storm activity in 1973 in the southern hemisphere has been related to the increased ocean-to-atmosphere heat flux produced by the abnormally low ice coverage of the Southern Ocean (Ackley and Keliher, 1976). Similarly, diminished summer ice coverage in the Barents Sea has been positively correlated with increased winter snow coverage of the northern hemisphere continents (Kukla, 1976), a correlation to be expected from the reasoning of Ewing and Donn. As a final illustration, Fletcher (1969) has extrapolated from ice data of one station in the South Orkneys that increased winter iciness coincides with a more vigorous global circulation of the atmosphere and with warmer temperatures in the tropics and midlatitudes.

Although most such correlations are spurious, the increase of world population heightens the importance of understanding legitimate ones. A small fluctuation in a climatic pattern can result in fantastic suffering on a large human scale, and this tends to intensify as population, food, and energy pressures increase. In addition to the dangers from the continual small fluctuations, many scientists now believe that much larger climatic fluctuations can occur in a far shorter time span than had formerly been thought possible. For instance, both Dansgaard *et al.* (1973) and Thompson (1977) have presented evidence from deep ice cores for extremely rapid transitions from interglacial to glacial phases; Wilson (1964) has postulated the inherent instability of the Antarctic ice sheet; and Hughes (1973, 1974) has hypothesized from mathematical analyses of stable contours the possibility of a glacial surge of the West Antarctic ice sheet in particular.

On a seasonal basis, the freezing and melting of ice affects climate by releasing energy (during freezing) in the winter season and absorbing it in the summer, thus lessening seasonal temperature extremes (Baker, 1976). Furthermore, the presence of the ice magnifies the warming effect of the incoming ocean currents in the subarctic since as the warm currents melt the snow and ice they thereby lessen the surface albedo (Manabe *et al.*, 1975). At the same time though, this absorption of energy during ablation does contribute toward cooling the currents themselves.

The importance of the ice is hence fairly well-established, although, as with the case of every suggested cause of climatic change, the precise nature of its role remains uncertain. In fact far less scientific attention has been directed to the ice and other portions of the cryosphere than to either the atmosphere or oceans. Yet, as will be detailed more fully for sea ice in Chapter V, the cryosphere also is a variable part of the earth's climatic system and covers a considerable proportion of the horizontal area at the air-surface interface. From satellite data averaged for seven years, snow, land ice, and sea ice spread over 58.4×10^6 km^2 of the northern hemisphere in January and 14.3×10^6 km^2 in July, while the corresponding figures for the southern hemisphere are 18.0×10^6 km^2 and 25.0×10^6 km^2 (Untersteiner, 1975).

One method of seeking an understanding of this ice mass is through numerical modeling. Another possibility is laboratory experimentation, but it would be difficult to devise an experiment which could show the scale desired. Numerical modeling has its limitations also, among them being restrictions in terms of horizontal resolution and the impossib lity of including all potentially relevant aspects. Nonetheless, the modeling method is attempted here and the emphasis is on the large spatial scale. This necessitates a low-resolution format, with the selected horizontal grid spacing being on the order of 200 km. In spite of the limited amount known about sea ice, enough is known to assure us that its growth, decay, transport, structure, and spatial distribution are far more complicated than could be fully explained by the relatively small number of factors that can reasonably be incorporated into any numerical model, whether high or low resolution. Thus any expectation of complete success would be unrealistic.

However, it should be borne in mind that meteorologists and oceanographers deal with fully as complicated phenomena, and yet over the past three decades both these groups have developed low-resolution numerical models which have broadened the base of their understanding of the atmosphere and oceans, respectively. Their models of course cannot reproduce all the intricacies of the real world. Nevertheless, they have reproduced the large-scale features of jet streams, monsoons, and the Hadley circulation. It is at this broad macro-level that the sea ice model to be developed here is addressed, hopefully filling an existing gap in macro-level modeling.

In fact the large-scale numerical models of the atmosphere and of the oceans have both reached the stage where it is felt that a coupling of the two is among the major steps now needed to improve the ability of the models to reproduce atmospheric and oceanic phenomena and thereby to further our understanding of the climate system and its interactions. That is, the sophistication of these models has increased to the point where the inadequacy of a primitive specification of the boundary conditions has emerged as a major obstacle to further progress. As the models become coupled, it will be imperative that the interface be given adequate consideration.

A portion of the earth-atmosphere system as large as that of sea ice should not be neglected, especially when the insulation and albedo effects ensure the importance of the location of the ice boundary. All elements of the system interact; thus for a full numerical treatment, atmosphere, hydrosphere, and cryosphere must eventually be modeled together.

The development and testing of an accurate sea ice model are both hindered by the above-mentioned scarcity of basic ice research. Even the mere plotting of changing large-scale ice distributions has occurred only recently, particularly with the advent of satellite imagery, though locally, countries bordering the Arctic have somewhat longer histories of regular ice observations, mainly in support of local shipping and fishery interests. Regular ice observations were begun by Finland in 1846, Sweden in 1870, Denmark and Germany in the 1890s, and Japan in 1892. The largest observational system has been developed in the Soviet Union over the past several decades, while interest from the United States and Canada did not begin on a large scale until the 1950s (Heap, 1972). Much of the increased interest in ice in the 1970s stems from the discovery of oil in the Arctic. The importance of understanding ice stresses in designing offshore structures and the importance of accurately predicting ice motions for passenger and supply transport are both well-recognized (Ralston, 1977; Brown, 1976; Weeks, 1976b; Pritchard, 1975; Nikiforov *et al.*, 1970). Partly for these practical reasons, as well as the scientific ones, massive observational efforts are now underway to improve our knowledge not only of the spatial distributions of ice but of the mechanisms and stresses involved.

Most notable among these recent observational efforts are the Arctic Ice Dynamics Joint Experiment (AIDJEX) established in 1970 and based at the University of Washington in Seattle, the Polar Experiment (POLEX) proposed by the Soviet Union and designed as part of the First GARP (Global Atmospheric Research Programme) Global Experiment (FGGE), and efforts by various groups to analyze satellite information. Each of these studies can be expected to increase our sea ice data base, provide further understanding of relevant processes, and presumably thereby suggest useful refinements in the numerical model to be presented in Chapter IV. Such combined efforts should eventually contribute to a coupled atmosphere-hydrosphere-cryosphere model with more sophistication and correspondingly more forecast and evaluative capabilities for atmospheric, oceanic, and ice phenomena than are possible with the current non-coupled models.

For reader convenience, maps are included locating relevant place names in both Arctic and Antarctic regions (Figures 1 and 2).

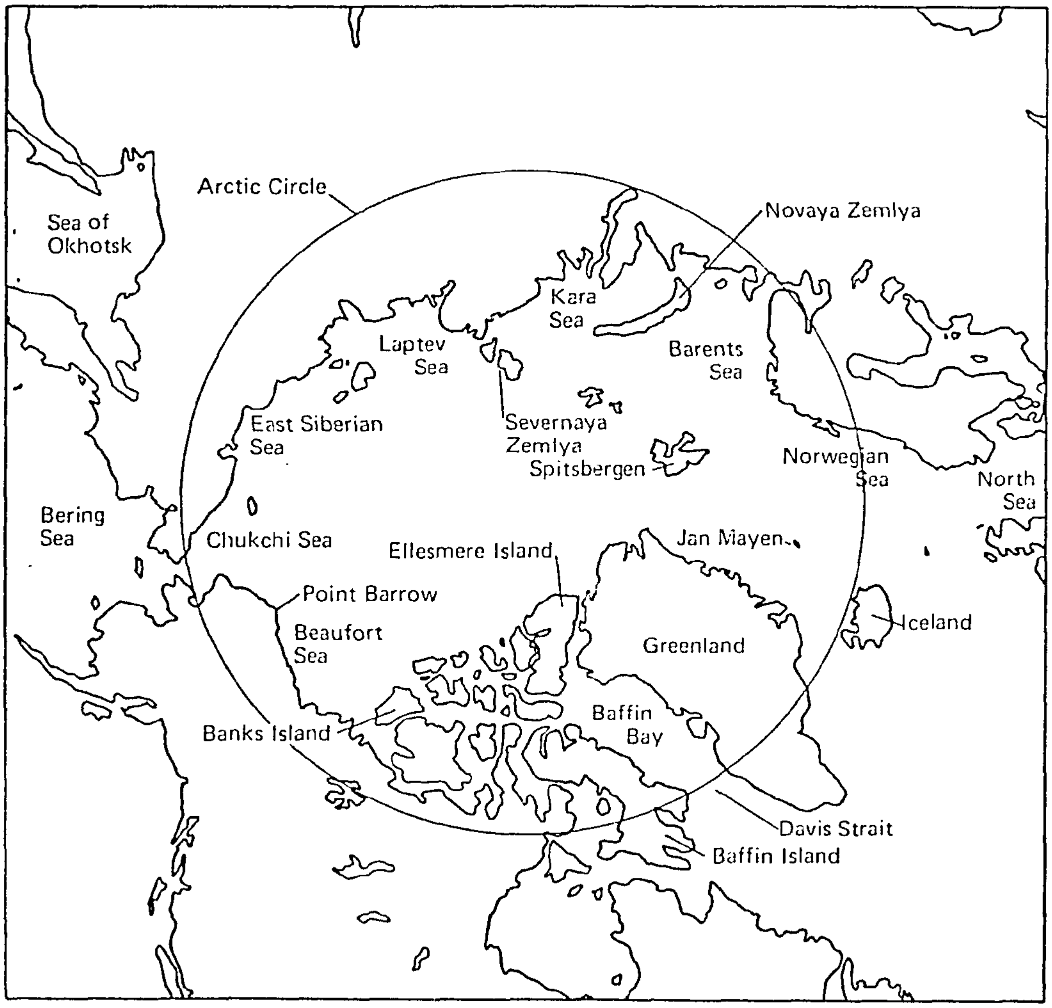

Figure 1. Map of relevant place names in the northern hemisphere.

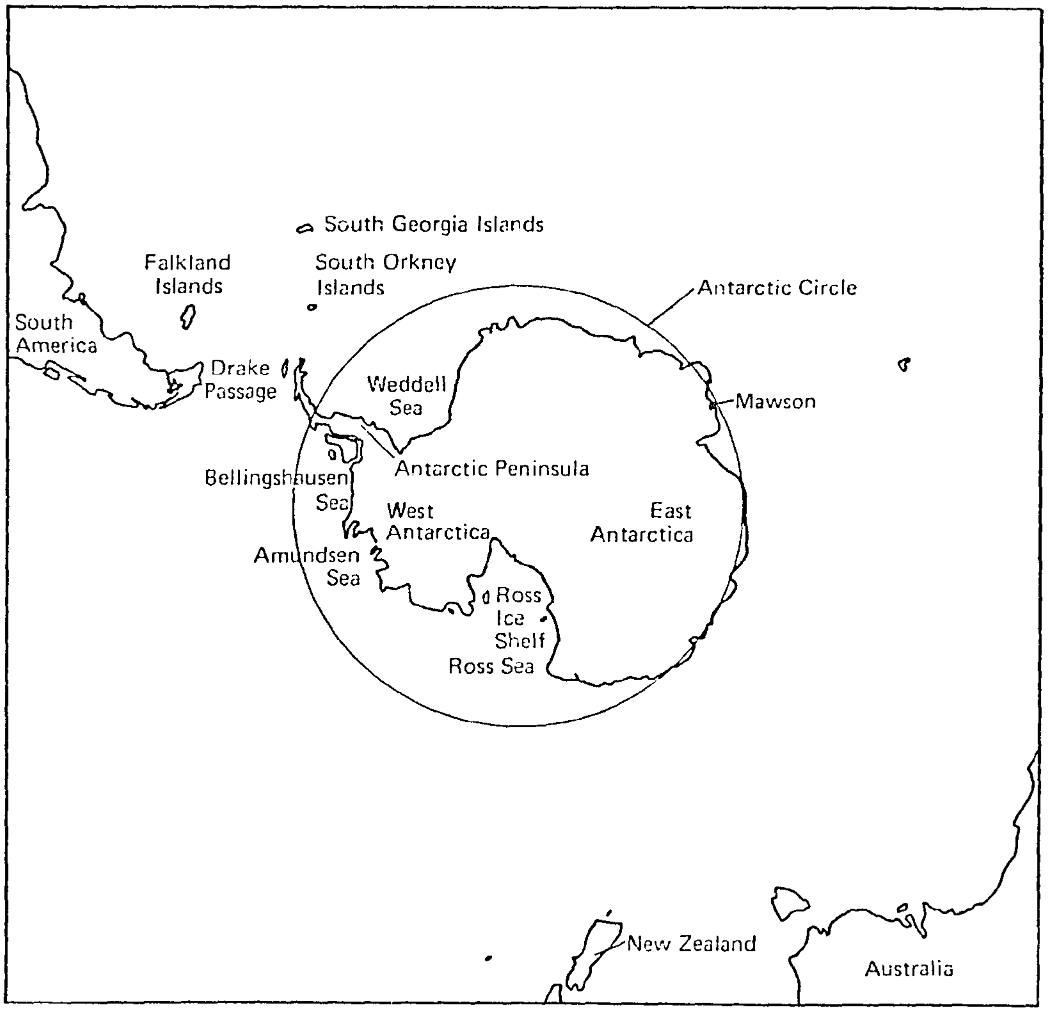

Figure 2. Map of relevant place names in the southern hemisphere.

CHAPTER II

CHARACTERISTICS OF SEA ICE

2.1 Global Sea Ice Distribution

Figures 3 and 4 present maps of the average distribution of sea ice in each hemisphere toward the end of the respective summers and winters. Such maps differ between sources, but the general picture remains similar. Typically the areal extent of floating Antarctic ice varies within the year from a minimum of 2.5×10^6 km^2 to a maximum of 2.0×10^7 km^2, a variation from roughly 1% of the southern hemisphere to roughly 8%, or from 1.6% of the southern hemisphere oceans to 13%. Ice extent in the northern hemisphere varies far less, ranging from a summer minimum of 8.4×10^6 km^2 to a winter maximum of 1.5×10^7 km^2, the latter being roughly 10% of the ocean area in the northern hemisphere (Untersteiner, 1975; Fletcher, 1969).

With the exception of the region north of Scandinavia, the Arctic Ocean remains covered with ice throughout most of the year. The central 70% of the Ocean, covering roughly 5.2×10^6 km^2, consists of a fairly compact ice mass called the polar cap. At any given time this cap area tends to have regions of extensive hummocking and pressure ridging, an

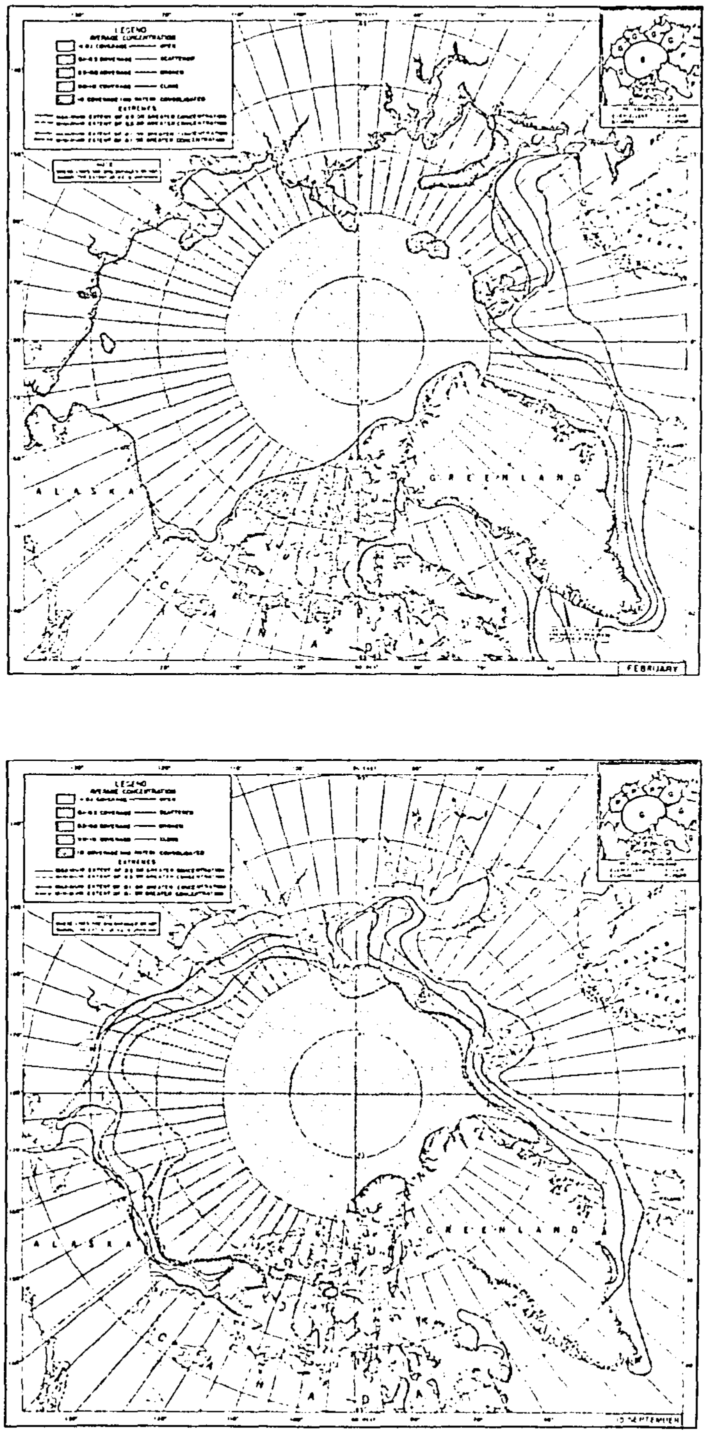

Figure 3. Average Arctic sea ice concentration and extent, February and September 1 - 15. [From Neumann and Pierson (1966, pp. 76-77), courtesy of Prentice-Hall, Inc. The maps were published by Neumann and Pierson courtesy of the U. S. Naval Oceanographic Office, Washington, D. C.]

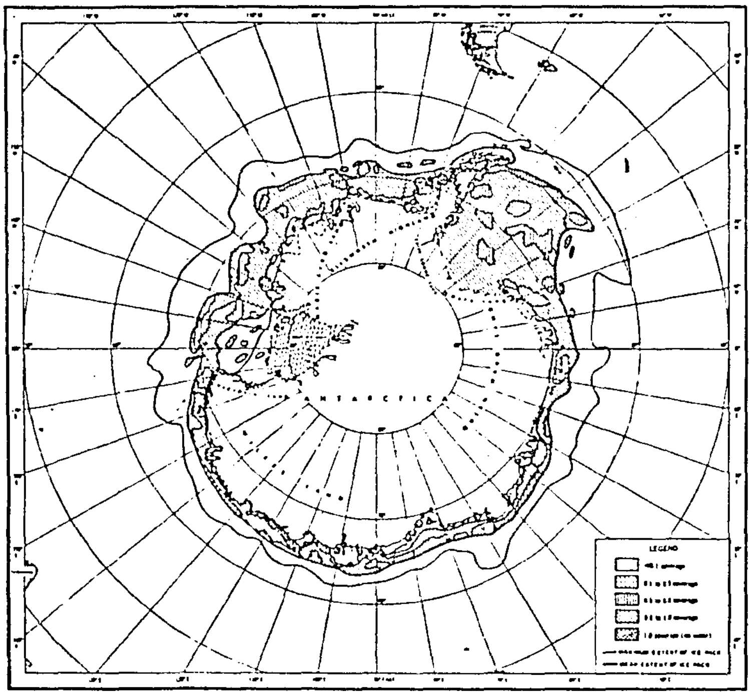

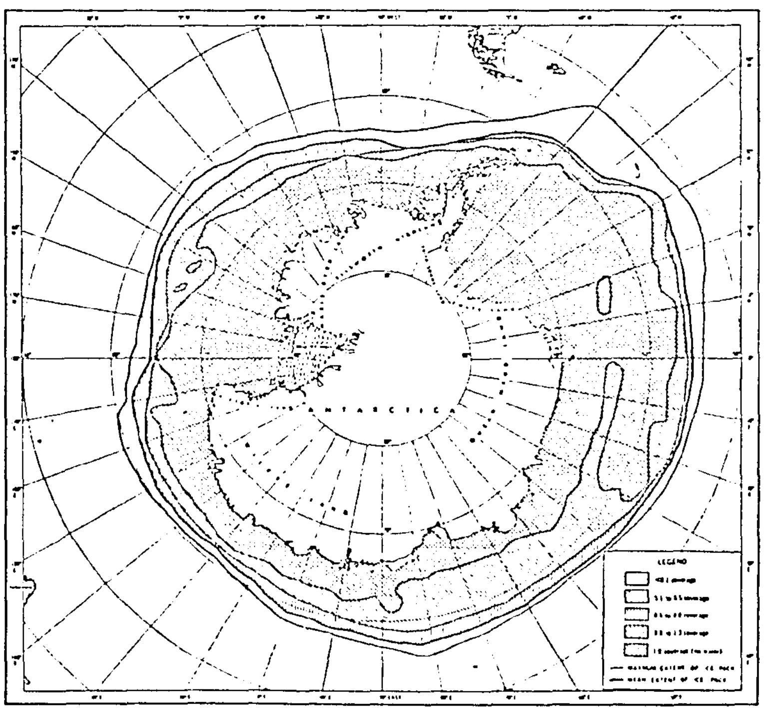

Figure 4. Average Antarctic sea ice concentration and extent, February and October. [From Neumann and Pierson (1966, pp. 79-80), courtesy of Prentice-Hall, Inc. The maps were published by Neumann and Pierson courtesy of the U. S. Naval Oceanographic Office, Washington, D. C.]

irregular placement of leads, and occasionally large areas of open water as well. In addition to the cap ice, fast ice grounded to the shore horizontally or to the ocean floor vertically also exists in the Arctic and may extend from the coast out 500 km along the Siberian continental shelf. Sea ice moves into the North Atlantic by way of the East Greenland and Labrador Currents and into the North Pacific through the Bering Strait. It also forms *in situ* in the North Pacific and surrounding waters, though this is generally restricted to the Bering Sea, the Sea of Okhotsk, and the Sea of Japan. Ice rarely is sighted in the Pacific outside the period from November to June.

The distribution of ice in the Antarctic is more symmetric than that in the Arctic and less compact. The increased symmetry results not only from the more symmetric land-sea distribution in the high latitudes of the southern hemisphere but also from the absence of an incoming warm water current of the magnitude of the North Atlantic's Gulf Stream. The one region where Antarctic ice is frequently seen decidedly north of its roughly symmetric pattern is in the region of the cold Falkland Current to the east of South America. Roughly, Antarctic sea ice extends to about 60°S in the winter and to about 66°S in the summer, the average extension often being farthest north of the Weddell Sea with longitudes approximately $30\text{-}50^{\circ}$W. The lessened compactness of Antarctic *versus* Arctic ice--i.e., the larger percentage of open water--is a consequence of at least two major factors: the lower latitudes of Antarctic ice and the contribution to divergent motion from predominant winds.

This general picture of global ice distribution omits mention of average thicknesses, actual percentages of open water, precise boundaries, drift patterns, and other such information due both to the absence of definite data and also to the existence of significant year-to-year variations. However, estimates of these characteristics are important in evaluating results from the model and hence are discussed in Chapter V. Here we turn instead to the phenomenon of ice itself: to its formation, its properties, its ablation, and also its general topography, both on the top and bottom surfaces. In doing so, this chapter discusses some of the complexities ignored within the computer model of Chapter IV.

2.2 Sea Ice Formation

The predominant reason for ice formation is that water reaches its freezing point and solidifies from its liquid state. However, the existence and distribution of ice at the sea surface are functions of more than the simple cooling of surface waters to a precise freezing point. In addition to temperature, ice formation depends on salinity, water depth, turbulence, and the presence of nucleation centers. The influence of water depth is fairly straightforward: freezing begins more quickly in shallower water due to the decreased volume of water to be cooled. The influence of nucleation centers is also straightforward, with freezing initiated more rapidly when many nucleation centers are present. The ability of these centers to initiate freezing increases with water agitation, and it appears that under calm conditions a small amount of supercooling, on the order of 0.1 K, is common in both Arctic and Antarctic waters. However, once an ice crystal is formed or introduced into the supercooled water, the freezing for the entire supercooled area tends to be rapid, as the ice crystal provides the required initial nucleation center (Coachman, 1966).

The influence of salinity on ice formation is more complex. The temperature of the freezing point of water decreases as the salinity rises, but as the salinity rises the temperature of density maximum for the water decreases as well, and this decrease is more rapid than the decrease for the freezing point. For pure water and for sea water with a salinity below $24.7^{o}/oo$, the temperature of the freezing point is less than the temperature of density maximum; with a salinity of $24.7^{o}/oo$ these two temperatures are equal (at $-1.3^{o}C$); and with salinities above $24.7^{o}/oo$ it is the temperature of density maximum which is the lesser of the two values (Donn, 1975). Thus as water with a salinity greater than $24.7^{o}/oo$ is cooled by the atmosphere, the cooling surface water will continue to convect down, for its lowered surface temperature will yield densities greater than those of the waters beneath. As a consequence, if the salinity is uniform and greater than $24.7^{\circ}/oo$, the entire depth of water tends to be cooled to or near the freezing point before freezing can commence at the surface, and once freezing begins it will tend therefore to proceed rapidly, as it will be unhindered by warm water underneath.

Actually, the salinity of the oceans is not uniform and thus the complete convection of the above scenario does not hold. Stable density structures in the Arctic and much of the Antarctic limit the actual amount of convective mixing required. By contrast, the Antarctic shelf waters do tend to be well-mixed, and the cooling does tend to convect down to the bottom before freezing begins (Untersteiner, 1975).

During the freezing process, crystals of needle-like or plate-like form are created. These are generally oriented vertically, and as they coalesce a portion of the initial brine escapes to the water beneath, the remainder being trapped in cavities formed during the coalescence. Initially the freezing crystals are pure H_2O, but with further temperature reductions the salts crystallize as well. The temperature at which crystallization occurs for a given salt depends on the exact composition of the sea water, though typically sea water with a salinity of $35^{\circ}/oo$ will have its water crystallize at $-1.9^{\circ}C$, its sodium sulfate at $-8.2^{\circ}C$, its sodium chloride at $-23^{\circ}C$, its magnesium chloride at $-36^{\circ}C$, and its calcium chloride at $-55^{\circ}C$ (Neumann and Pierson, 1966).

The type and appearance of the newly formed ice depend largely on the state of the sea surface when the freezing begins and on the rapidity of cooling. With a calm sea and rapid cooling, the ice crystals tend to be needle-like and coalesce into a fairly uniform sheet of clear, thin ice. By contrast, if the sea surface is turbulent and the cooling slow then the ice formation begins with thin plates of ice crystals giving the surface a greasy or opaque appearance. Eventually the ice obtains a thick, soupy consistency and is called ice slush or grease ice. Further development often leads to so-called 'pancake ice', this being characterized by flat, circular disks 0.3-1.0 m in diameter. As the individual pieces of pancake ice coalesce, a larger sheet about 0.02-0.03 m thick forms, and then the thickness gradually increases as accretion by further freezing continues.

The speed of this additional freezing decreases with ice thickness, all other factors being equal. The reason centers on contrasting winter rates of heat loss from the ocean to the atmosphere, the loss tending to be great in regions of open water or thin ice but much reduced under the insulating influence of a thick ice cover.

2.3 Sea Ice Composition and Properties

The structure and composition of the sea ice once formed depend on the salinity of the initial water, the speed of freezing, the amount of any melting subsequent to freezing, the temperature, and several other factors. The more quickly the freezing occurs, the more brine is likely to be trapped and the larger the expected size of the brine cavities. Thus for a given water salinity, the sea ice salinity tends to increase with a decrease in the temperature of ice formation, the lower temperature tending toward a faster ice formation. Samples from the Norwegian *Maud* expedition in the Arctic show an ice salinity generally between 3 and $8^{o}/oo$, with a sample maximum of $14.59^{o}/oo$ (Neumann and Pierson, 1966). Weber (1977) suggests $4^{o}/oo$ as an appropriate value for the bulk of sea ice, though he concurs with Untersteiner (1975) in the possibility of $20^{o}/oo$ values for new, rapidly formed ice.

Due to the settling of salt through the ice, in the absence of countering tendencies the salinity of an individual ice floe will decrease with time and the surface salinities of different floes will tend to be inversely related to ice thickness. Weeks (1976a) estimates salinities of $12\text{-}15^{o}/oo$ for newly formed ice, salinities of $4\text{-}5^{o}/oo$ for ice after a year's growth, and salinities increasing from near $0^{o}/oo$ at the top of multiyear ice to $2\text{-}3^{o}/oo$ at the bottom. Actual surface salt contents are listed by Maykut (1976) as a function of thickness, with 14.4 kg m^{-3} presented for an ice thickness of 0.05 m and 5.2 kg m^{-3} for a thickness of 1 m.

One property which alters dramatically at the moment of freezing is specific volume. The specific volume of H_2O rises immediately upon the change of state from liquid to solid, thus allowing the ice formed to float on the remaining water. For pure water, specific volume jumps from 1×10^{-3} m^3 kg^{-1} to 1.09×10^{-3} m^3 kg^{-1}, then with further cooling the ice slowly contracts, specific volume decreasing to 1.085×10^{-3} m^3 kg^{-1} by a temperature of -30°C. For sea ice, cooling after freezing initially leads to continued volume expansion. The temperature at which further cooling then produces contraction is dependent on, and decreases with, an increase in salinity (Neumann and Pierson, 1966).

In fact the specific volume of ice, along with its inverse the density, depends primarily on the air and salt content. From the previous paragraph, pure liquid water at 0°C has a density of 1000 kg m^{-3}, while pure ice at 0°C has a density of 917 kg m^{-3}. The density of sea ice is generally lower than that of pure ice, though not always. As would be expected, it tends to increase with an increase in salinity but to decrease with an increase in porosity. According to Weeks (1976b), theoretically, air-free sea ice has densities ranging from 920 to 950 kg m^{-3}. Actual measurements on Arctic ice have yielded densities ranging from 857 to 924 kg m^{-3} (Neumann and Pierson, 1966), though Rigby and Hanson (1976) narrow the predominant range down to 890-910 kg m^{-3}.

The specific heat and latent heat of fusion of ice both depend largely on salinity and temperature, specific heat increasing significantly with both variables (Table 1) and latent heat of fusion decreasing with them both (Table 2).

TABLE 1. Specific heats (in J K^{-1} kg^{-1}) for sea ice of various temperatures and salinities. [Abbreviated from Neumann and Pierson (1966, p. 83) with units converted from cal $^{o}C^{-1}$ gm^{-1}.]

	Temperature		
	$-2^{o}C$	$-8^{o}C$	$-14^{o}C$
Salinity			
$2^{o}/oo$	1.08×10^{4}	2.64×10^{3}	2.26×10^{3}
$8^{o}/oo$	3.67×10^{4}	4.23×10^{3}	2.68×10^{3}
$15^{o}/oo$	6.71×10^{4}	6.12×10^{3}	3.23×10^{3}

TABLE 2. Latent heats of fusion (in J kg^{-1}) for sea ice of various temperatures and salinities. [Abbreviated from Doronin (1970, p. 69) with units converted from cal gm^{-1}.]

	Temperature		
	$-0.5^{o}C$	$-1^{o}C$	$-2^{o}C$
Salinity			
$0^{o}/oo$	3.35×10^{5}	3.36×10^{5}	3.38×10^{5}
$1^{o}/oo$	2.98×10^{5}	3.18×10^{5}	3.29×10^{5}
$2^{o}/oo$	2.62×10^{5}	2.99×10^{5}	3.20×10^{5}
$8^{o}/oo$	4.03×10^{4}	1.89×10^{5}	2.65×10^{5}

2.4 Sea Ice Ablation

During summer, ice tends to melt and in some areas to disappear altogether. A typical summer scenario at the edge of an ice pack is presented by Langleben (1972). As the solstice approaches and the days lengthen, the high insolation causes rapid snow melt, which decreases the surface albedo and thereby allows absorption of a greater percentage of shortwave radiation. With the decreased or vanished snow cover the ice starts ablating at roughly 0.04 m per day. Drainage canals, vertical melt holes, and multiple melt ponds develop. After melting reduces the ice thickness to roughly 1-1.5 m, erosion has become intense enough to completely crack the ice along many of the drainage-canal flaws, the cracking being aided by the action of tides and storms. The lessened continuity of the ice cover then accelerates the decay by the increased thermal interaction with the water. In many of the inlets and fiords along the Arctic coastline, the disintegration is complete, with the ice cover entirely vanishing by the end of each summer (Langleben, 1972).

During ice ablation, the salt crystals, if any, melt first, along with the ice immediately around them. This increases the volume of the brine cavities, making the ice more porous and frequently allowing some of the brine to drop to the water underneath. This partially explains the altered properties, in particular the lowered salinity, of older ice, parts of which have often alternately melted and frozen.

2.5 Sea Ice Topography

As for the meso-scale appearance of the ice, a large ice pack reveals a rough topography both on the bottom surface and the top. Thin ice especially is capable of extensive ridging when acted upon by opposing horizontal forces. As large floes move toward each other, intervening thin ice and ice rubble mass together and, under sufficient pressure, pile to heights and depths significantly larger than the original floes. Although ridges greater than 4 m in height are rare, occasionally sails extend 13 m above sea level and keels 47 m below (Weeks, 1976a).

From two years of aerial surveys, Wittmann and Schule (1966) estimate that pressure ice covers 13-18% of the ice area in the Canadian Basin, while data from the British nuclear submarine H. M. S. *Dreadnought* (Swithinbank, 1972) determined an average of two ice keels with drafts greater than 10 m for each kilometer of linear track near the North Pole. The *Dreadnought* survey was conducted in early March 1971 and recorded continuous profiles of the undersurface of the Arctic ice between 1°E and 8°E from the ice edge at $79^{\circ}15'$N northward to the Pole. Some of the keels reached 30 m in depth (Swithinbank, 1972). Because the keels, especially for multiyear ice, tend to be much broader than the ridges above them (Rigby and Hanson, 1976), the keel depth-to-ridge height ratio cannot be determined simply from the sea ice and sea water densities. Instead the ratio is generally much lower than the approximate 7.2:1 which these densities (about 900 kg m^{-3} and 1025 kg m^{-3} respectively) would suggest. A typical ratio according to Weeks (1976b) is 4.9:1 and according to Wittmann and Schule (1966) is only 3.3:1. Typical slope angles for ridges are 25^{o} for the sail and 35^{o} for the keel (Weeks, 1976b).

Spatially, in the Arctic the greatest amount of ridging is near the coasts (Weeks, 1976b), as is well-illustrated for the western-hemisphere Arctic by the maps of Tucker and Westhall (1973). Analyzing results from airborne laser observations taken between April 1970 and February 1973, Tucker and Westhall have tabulated and contoured the average number of ridges per kilometer in 26 geographical regions of the Arctic Basin. To be included a ridge must be at least 1.22 m high, and separate plots are presented for winter, late winter-early spring, summer, and fall. The plots show ridge intensities to be greatest in winter, least in summer, and peaking in all seasons just north of Greenland and Ellesmere Island. Winter intensities in these peak regions are 10 ridges (of height $\geq$ 1.22 m) per kilometer.

Although ridges are the most spectacular relief form on the ice, there are also other irregularities throughout a normal ice pack. Among these are ice chunks, fissures, low hills, and depressions from melt ponds or fresh water pools. Yakovlev (1970) discusses and classifies many of these relief forms. Irregularities tend to lose their angularity with time, and former ridges often become chains of smoothed ice mounds after several years. Included in the micro-relief of an ice pack are small, columnar ice crystals frequently formed at the start of the melt season and the subsequent thin layer of ice grains produced after the columnar crystals break. This layer might be 0.05-0.1 m thick at the height of thawing, though a heavy rain will eliminate it altogether (Yakovlev, 1970). Among the approximations to be assumed in Chapter IV, the rough ice topography of the actual world is eliminated by allowing only one ice thickness per grid square at any moment.

CHAPTER III

PREVIOUS ICE MODELING

Previous ice modeling has tended to be divided into two sets of studies: one modeling thermodynamics and the other, dynamics. In general these two aspects have not been interlocked, the thermodynamic models tending to be one-dimensional and the dynamic models tending to ignore thermodynamics.

3.1 Thermodynamics

Calculations of ice and snow accretion and ablation in the present study (Chapter IV) are patterned after the Arctic work of Untersteiner (1964), Maykut and Untersteiner (1969, 1971), and Semtner (1976a). Each of these studies is one-dimensional in space and each specifies atmospheric energy flux densities rather than computing them. More precisely, fluxes in these earlier models are smoothed from monthly values thought appropriate for the central Arctic. None of the models is applied to the Antarctic and none includes ice transport.

Maykut and Untersteiner (1969, 1971) construct an elaborate one-dimensional thermodynamic model of sea ice, computing the time-dependent ice thickness and vertical ice temperature profile based on diffusion equations with finite-difference approximations involving a grid interval of 0.10 m.

They include the effects of ice salinity, brine pockets trapped within the ice, heating from penetrating shortwave radiation, vertical variations in ice density, conductivity, and specific heat. Theirs is the most complete one-dimensional ice model devised so far; however the model takes 38 simulation years to reach equilibrium and this inhibits its extension to a three-dimensional framework.

Maykut and Untersteiner (1969, 1971) perform 28 separate sensitivity studies. After testing various constants for the percentage of shortwave radiation penetrating the ice, for the magnitude of the oceanic heat flux, and for monthly snow accumulations, they vary a series of parameters specifically to examine the feasibility of man's deliberately changing ice thickness through influencing those parameters. The latter include oceanic heat flux, snowfall, atmospheric turbulent heat fluxes, incoming shortwave and longwave radiation (artificially changeable through a control on cloudiness), surface shortwave albedo (changeable through artificially covering the ice or through introducing snow lichen), and longwave emissivity. Maykut and Untersteiner conclude that albedo changes are the most feasible for effective planned modifications.

Semtner (1976a) simplifies the Maykut and Untersteiner model, making it more appropriate for three-dimensional simulations. This he does largely through a reduction in the number of vertical layers, through a change in the differencing scheme, through the elimination of a heat source term in the diffusion equation, and through the use of constants rather than variables for the specific heats and conductivities of ice and snow. The Semtner equations are formulated for n temperature levels within the ice and snow, though the article stresses the performance of the 3-layer and 0-layer versions. Since he uses atmospheric and oceanic forcing identical to that of Maykut and Untersteiner, Semtner can compare the mean annual ice thicknesses from his models against the thicknesses predicted in the earlier, more complete work. Doing so for 25 separate cases, he finds an average deviation of only 0.22 m for the 3-layer version and 0.24 m for the 0-layer version. It is basically the Semtner 0-layer model which has been followed in the present work for the calculations internal to the ice and snow.

Closer to the present model in terms of spatial extent, the model of Pease (1975) simulates Antarctic ice along longitude 155^{o}E from 70^{o}S to 58^{o}S. Although still not three-dimensional spatially, the model can compute the advance and retreat of ice along the 155^{o}E meridian, thus giving it a capability not available with the one-dimensional models of Maykut and Untersteiner (1969, 1971) or Semtner (1976a). Furthermore, Pease computes atmospheric fluxes rather than specifying them as in the two former studies, and she tests the effects of three parameterizations of the oceanic mixed layer. In the first parameterization the heat flux from water to ice is calculated as a function only of the previously specified 20 m temperature field. In the second parameterization the 200 m mean temperature and salinity fields are specified but the temperatures and salinities of the mixed layer directly under the ice are calculated and the heat and salt fluxes are determined from these calculated values. The third parameterization extends this by inserting a transient melt layer at the top of the mixed layer. Pease finds the results (on the ice) of the second and third parameterizations to be practically identical.

Pease tests the model by comparing the simulated 0 m ice boundary with the observed mean extent at 155°E as extrapolated from the Soviet *Atlas of Antarctica* (Tolstikov, 1966). Five cases are run--a standard case, one with increased diffusivity, one with decreased diffusivity, one with increased cloudiness, and one with decreased cloudiness--with the conclusion that the most obvious shortcoming is the failure to predict accurately the maximum and minimum extent (Pease, 1975).

An attempt at a three-dimensional ice simulation is included in Bryan *et al.* (1975) and Manabe *et al.* (1975). They compute an ice distribution within a global ocean-atmosphere climate simulation, stressing long-term results and using mean annual insolation rather than a seasonally varying forcing. Although they include transport of the ice, the ice moves strictly with the water of the upper ocean unless its thickness equals or exceeds 4 m, in which case the ice movement stops altogether. The resulting calculations lead to an unreasonable build-up of Arctic ice with time, the average and maximum thicknesses steadily increasing, with values of 5.32 m and 24.7 m respectively in year 200 of the simulation (Manabe *et al.*, 1975).

3.2 Dynamics

Additional discussions of ice transport include a wide range of formulations. Certainly the simplest are those relating the speed and direction of the ice strictly to the speed and direction of the water, as with Manabe *et al.* (1975), or strictly to the speed and direction of the boundary-layer wind. As an example of the latter, Zubov's rule has the ice drifting parallel to the atmospheric isobars and at a speed directly proportional to the pressure gradient (Gordienko, 1958).

Most other formulations of ice transport calculate the ice velocity by considering a balance of forces acting on the ice and assuming a steady-state solution. It appears widely agreed (e.g., Campbell, 1964; Doronin, 1970; Coon *et al.*, 1976) that the relevant forces are five in number: wind stress, water stress, Coriolis force, the stress from the tilt of the sea surface (dynamic topography), and the force from interactions within and among floes (internal ice resistance). However, disagreement exists regarding the relative magnitudes of these, with the result that different researchers have included different combinations in their final balance. A summary of the forces used by various authors appears in Table 3. The 1928 study by Sverdrup balancing wind stress, Coriolis force, and internal ice resistance is the first to insert the ice resistance term, including it primitively as the product of the drift velocity and a coefficient of friction. The first model with dynamic topography is the Felzenbaum (1958) balance of dynamic topography with wind stress, water stress, and Coriolis force; while the first balancing all five forces is Campbell (1964). Hunkins (1966, 1974) also uses all five stresses, though he does so not to calculate ice velocities but to determine internal ice resistance as a residual. Rothrock (1973) uses all five stresses, inserting the internal ice resistance through an assumption of incompressibility.

Just as different researchers balance different forces for the transport calculations, they also use different parameterizations for the forces included. For example, in dealing with the water stress, Nansen (1902) assumes an Ekman spiral in the ocean reaching precisely to the ice boundary, and fixes the angle between the ice velocity and the water stress at a constant 45°. On the other hand, Shuleikin (1938) assumes a boundary layer between the Ekman spiral and the ice and then uses an empirical formula of Ekman (1905) which sets the water speed at the top of the Ekman spiral as a constant multiple (for a given latitude) of the wind speed. As with Nansen, this results in a constant angle between the water stress and

TABLE 3. Forces included for the transport calculations of previous models. Extended from Campbell (1968).

	Wind stress	Water stress	Coriolis force	Internal ice resistance	Dynamic Topography
Nansen (1902)	√	√	√		
Sverdrup (1928)	√		√	√	
Rossby and Montgomery (1935)	√	√			
Rossby and Montgomery (1935)	√	√	√	√	
Rossby and Montgomery (1935)	√		√	√	
Shuleikin (1938)	√	√	√		
Felzenbaum (1958)	√	√	√		√
Ruzin (1959)	√	√	√	√	
Reed and Campbell (1960, 1962)	√	√	√		
Campbell (1964)	√	√	√	√	√
Hunkins (1966, 1974)	√	√	√	√	√
Rothrock (1973)	√	√	√	√	√
Coon *et al.* (1976)	√	√	√	√	
Pritchard *et al.* (1976)	√	√	√	√	√
Hibler (1977)	√	√	√	√	√

the ice velocity, but the angle is now roughly 18^{o} rather than 45^{o}. Reed and Campbell (1960) treat the water stress instead on the basis of the equation

$$\tau_w = \rho_w K_w \frac{dr}{dz} \quad , \tag{1}$$

where ρ_w is water density, z depth, K_w the vertical eddy viscosity for water, and r the magnitude of the vector difference between the velocities of the ice and the water underneath. Due to numerical complications, Reed and Campbell simplify to an eddy viscosity which is independent of depth in the Ekman spiral layer and decreases linearly in the boundary layer. This allows water stress to be expressed as

$$\tau_w = \rho_w \sqrt{f \; K_w} \, V_o \quad , \tag{2}$$

a result first obtained by Ekman. The same expression for water stress is used by Campbell (1964) and Hunkins (1966), though Hunkins sets the eddy viscosity at a constant $23.8 \times 10^4 \; m^2 \; s^{-1}$. Similarly, Rothrock (1973) uses

$$\vec{\tau}_w = \rho_w \sqrt{f \; K_w} \; [\cos \theta_w (\vec{U}_w - \vec{u}) + \sin \theta_w \; \vec{k} \times (\vec{U}_w - \vec{u})] \tag{3}$$

where $\vec{U}_w$ = water velocity,

$\vec{u}$ = ice velocity, and

θ_w = the angle of turning between the water and ice velocities.

Rothrock assumes constant K_w and θ_w, taking values of $24 \times 10^{-4} \; m^2 \; s^{-1}$ and 20^{o}, respectively. McPhee and Smith

(1975) instead employ the expression

$$\tau_w = 3.4 \times 10^{-3} \rho_o (U_R{}^2 + V_R{}^2) \tag{4}$$

where (U_R, V_R) is the vector difference $\vec{U}_w - \vec{u}$.

The above partial indication of the variety of parameterizations of water stress suggests some of the difficulty in determining a proper representation. A similar variety exists for the wind stress and the internal ice resistance. The most complete study in terms of selecting parameterizations and then combining them for a mathematical solution to the ice velocity is that of Campbell (1964). Although his solution is not seasonally dependent, Campbell does obtain a steady-state ice velocity field for the majority of the Arctic Ocean and he does, upon increasing the eddy viscosity of ice to 3×10^8 m^2 s^{-1}, position a Pacific Gyre approximately in its observed location.

However, in spite of its importance, the selection of forces and calculation of resultant velocities is only one aspect of the transport problem. By not proceeding to redistribute the ice according to the velocities obtained, the Campbell study and others mentioned above avoid the additional difficulties posed by excessive convergence and divergence. Two studies which face these difficulties in a limited fashion are Nikiforov *et al.* (1970) and J. Walsh (personal communication, 1976). Both examine ice convergence as encountered by a coastal boundary and both concern themselves with ice concentrations only, not thicknesses. These two studies will be reviewed in turn.

Nikiforov *et al.* (1970) examine the restricted problem of an ice field of uniform compactness moving at uniform and constant velocity toward a coastline. Assuming the initial fractional ice compactness of the strip between the coast and the boundary of the incoming ice to be b, the time it takes for the incoming ice to increase the compactness within this coastal strip to 100% is

$$T = L(1-b)/(av) \quad . \tag{5}$$

Here L is the width of the coastal strip, v is the ice velocity component normal to the shore, and a is the fractional area of ice coverage for the ice field moving in. Nikiforov *et al.* relax some of the initial restrictions and perform a simulation for the region of the East Siberian, Laptev, and Chukchi Seas. Once compactness adjacent to a coast reaches 100%, any velocity component normal to and approaching the coast is reduced to zero while velocity components tangential to the coast remain unchanged. Compactness n beyond the coastal region is altered according to

$$\frac{\partial n}{\partial t} = -\left(\frac{\partial nu}{\partial x} + \frac{\partial nv}{\partial y}\right), \tag{6}$$

where the ice velocity vector $\vec{v} = (u,v)$ is obtained by applying a proportionality factor and a set angle of rotation to the geostrophic wind as determined from actual synoptic pressure maps. The model uses a horizontal grid resolution of 100 km and calculates the distribution of ice compactness for 10 days subsequent to the initial state. The restriction to 10 days followed the assumption that omission of melting would lead to serious errors over longer periods. The 10-day simulations suggest that the influence of the coast is significant to 400 km and decreases proportionally to the distance from the coast (Nikiforov *et al.*, 1970).

Like Nikiforov *et al.* (1970), J. Walsh (personal communication, 1976) uses equation (6) for the time-dependence of compactness and zeroes out onshore velocity components wherever the intervening region to the coast is covered by ice of 100% compactness. Calculating within the portion of the Arctic bounded by 60°W, 120°E, 85.5°N, and the North American and Siberian coasts, Walsh employs a grid resolution of 1° latitude, 5° longitude and a timestep of 12 hours. At each timestep, observed pressure fields are used to generate geostrophic winds, from which presumed actual winds are obtained by rotating the geostrophic vectors 15° to the left and multiplying the magnitudes by 0.7. Internal ice stress is inserted by replacing the wind at a point by a weighting of the wind within a 371 km radius. Ice velocities are then obtained directly from the weighted wind field (rotating 30° to the right and multiplying by 0.02) and adjusted only by the above-mentioned zeroing out of the onshore velocities when appropriate. Upon comparing the calculated velocities to the motions of the AIDJEX main camp (situated on an ice floe at about 75°N, 145°W), Walsh finds that the calculated speeds deviate from the observed by an average of 20% of the observed and that the directions deviate by, in most cases, between 5° and 30°. Walsh applies his model to three midsummer time periods, these occurring in 1968, 1969, and 1975. Although with some misalignment of location and extent, the model does correctly predict the development of a large opening within the pack and the retreat and nonretreat of ice from the coasts of northern Alaska and northern Canada.

3.3 Arctic Ice Dynamics Joint Experiment

One of the largest groups attempting to understand sea ice has been mentioned only peripherally so far. This is the Arctic Ice Dynamics Joint Experiment (AIDJEX), established in 1970 and based at the University of Washington in Seattle. Now in its final stages, AIDJEX has been conducting an in-depth probe of many theoretical and empirical aspects of Arctic sea ice, including modeling. Geographically, the AIDJEX work centers on roughly one-twentieth of the Arctic basin, located in the Beaufort Sea, where the observational phase of the AIDJEX program was conducted from March 1975 to April 1976. Stressing a deeper physical understanding of a smaller spatial extent than the model developed below (Chapter IV), the AIDJEX ice model contains three major parts: a thickness-distribution model, a momentum equation for ice motions, and a stress-strain law. All aspects of the model are being developed theoretically, tested empirically, and adjusted as deemed necessary.

The AIDJEX thickness-distribution model is based on a thickness distribution function G(H,t) which is the fractional area with ice thinner than H at time t. The corresponding density function g(h,t) has g(h,t)dh equal to the fraction of area covered by ice with thickness between h and h + dh (Brown, 1976; Hall *et al.*, 1976). The momentum equation for ice transport includes all five major forces mentioned above plus an acceleration term. In fact, the four papers preceding Hibler (1977) in Table 3 are all part of the AIDJEX project. Typical of this work, Pritchard *et al.* (1976) have simulated ice conditions for a portion of the Beaufort Sea during the 10-day period May 15-25, 1975 and have performed detailed comparisons of the calculated motions *versus* both the observed and the results from a similar, earlier simulation (Coon *et al.*, 1976) using different boundary layer parameters. Mean floe thickness is estimated at a uniform 3.3 m and the simulation region is strictly separated from all coastal areas. The parameter changes of Pritchard *et al.* improve the drift directions, which are roughly 20° to the right of the observed in Coon *et al.*, though the authors express concern over the poor correlation between calculated and observed strain rates. They plan further modification of the model as more data become available.

The stress-strain relationships have been modeled at AIDJEX according to an unconfirmed (Hall *et al.*, 1976) elastic-plastic formulation. Basically, the modeled ice resists compression as a stiff elastic material until stress finally causes ridging, from which point the ice compresses as a plastic material. 'Strain hardening' occurs since the thicker the ice becomes, the more stress is required for ridging. As formulated in Coon *et al.* (1974) the calculations are based on an elastic-or-plastic model, whose major shortcoming as seen by Pritchard (1975) is in the kinematics. Pritchard revises the model to make the strain more physically meaningful than in Coon *et al.* In both models the placement of cracks in the ice is assigned beforehand, and the models proceed to describe the ridging and the opening of leads. Pritchard mentions that among the aspects requiring further modification are the flow rule, the yield constraint, and the elastic response.

In a later article Pritchard (1976) determines a lower bound for yield strength if a plastic model like the AIDJEX one is to simulate the ice properly. By examining data from the Beaufort Sea for five days in 1975 with steady winds and motionless ice, he calculates 1.0×10^5 N m^{-1} as a lower limit for yield strength under isotropic compression. This being an order of magnitude larger than the 6×10^3 N m^{-1} predicted by the AIDJEX model, the Pritchard (1976) study will be one of many leading to an adjustment of the model parameters by the

AIDJEX group.

The model developed in the following pages could be considerably aided by a completed AIDJEX project. However, the purposes of the two models are not the same, since AIDJEX is seeking a detailed understanding of ice while the present study is seeking a more simplified numerical simulation capable of coupling with large-scale oceanic and atmospheric models. The AIDJEX simulations are for a much smaller area spatially, are for a much shorter time period, and do not include the Antarctic. They are based on far more specific and detailed observational data and aim at a more precise determination of small-scale time and space fluctuations.

Ideally, a thorough knowledge of sea ice would already be available, providing proper large-scale constants, proper stress formulations, proper interpretations of ice response. That clearly not being the case, the model below--as well as the AIDJEX model, the Campbell model, and all other models--is forced to approximate in several areas where adequate information does not exist for a thorough understanding or even a well-founded approximation. The areas where this occurs will become clear in the next chapter.

CHAPTER IV

DESCRIPTION OF THE MODEL

The prime purpose of the numerical model described here is to simulate the thickness and areal extent of Arctic and Antarctic sea ice. Major components include the horizontal and vertical grids, calculations of ice ablation and accretion, determination of lead areas intermixed with the ice, and horizontal transport. The ablation and accretion calculations rely on computing heat fluxes into the ice from above and below, as well as on calculations within the ice layer itself, or within both the ice and snow layers. In this chapter each of the components of the model--the grid, the forcing from above and below the ice, the internal ice and snow calculations, the leads, and the horizontal transport--is discussed in turn.

4.1 The Grid

In the numerical model the earth's surface is approximated by a perfect sphere having a radius of 6370 km. Polar stereographic projections are used in each hemisphere, with rectangular grids superimposed. Standard conversion equations to such grids from latitude-longitude coordinates are given by Phillips (1957) for the northern hemisphere:

$$X = 2\,a\,\frac{\cos\,\phi}{1 + \sin\,\phi}\cos\,\lambda$$

$$Y = 2\,a\,\frac{\cos\,\phi}{1 + \sin\,\phi}\sin\,\lambda\,. \qquad (7)$$

Here, as throughout, ϕ denotes latitude positive to the north and λ denotes longitude positive to the east. Horizontal grid resolution for each polar region is determined by a 51×51 grid area enclosing the 45° parallel of latitude and divided diagonally by the 45° and 225° meridians. The grids (Figure 5) are oriented with the Greenwich meridian lying to the right of the North Pole and with the 90°E meridian lying to the right of the South Pole, thereby producing standard pictorial views in each hemisphere. As a result, in the northern hemisphere point $(X,Y) = (-25,0)$ occurs at latitude 45°N, longitude 180°E and point $(25,0)$ occurs at 45°N, 0°E. Either of these facts is sufficient for obtaining the constant a in equations (7):

$$a = \frac{25(1+\sin 45^{\circ})}{2\cos 45^{\circ}\cos 0^{\circ}} = \frac{25}{2}\,(\sqrt{2} + 1)\ , \qquad (8)$$

with the resulting conversions:

$$X = 25(1+\sqrt{2})\,\frac{\cos\phi}{1+\sin\phi}\,\cos\lambda$$

in the northern hemisphere (9)

$$Y = 25(1+\sqrt{2})\,\frac{\cos\phi}{1+\sin\phi}\,\sin\lambda$$

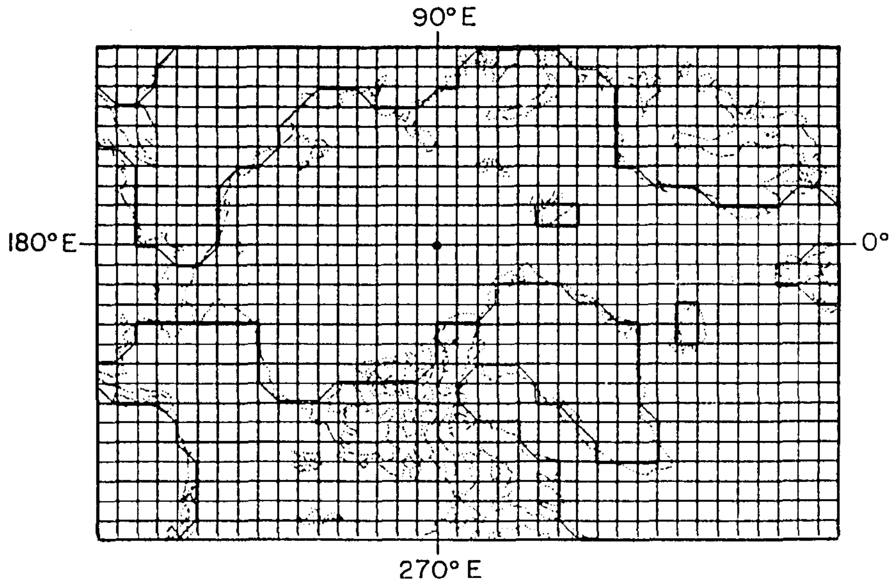

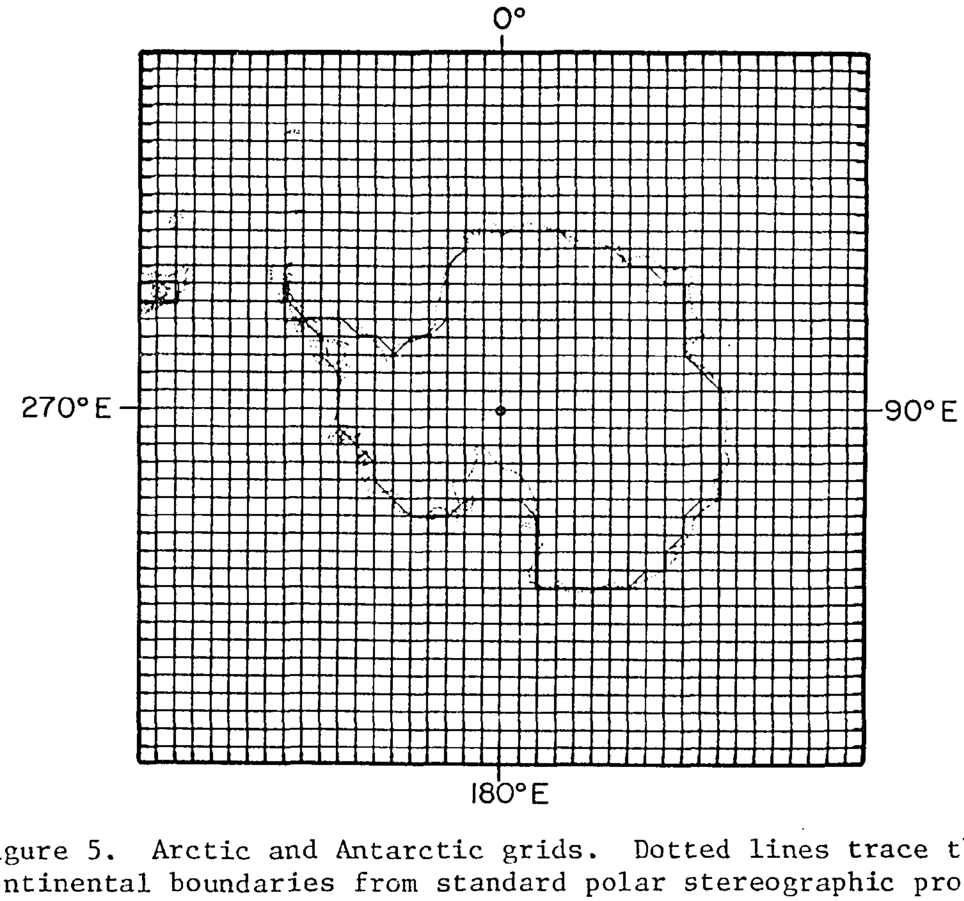

Figure 5. Arctic and Antarctic grids. Dotted lines trace the continental boundaries from standard polar stereographic projections. Model resolution of those boundaries is indicated in solid lines, as are the grids themselves. The South Pole is at the center of the 41 × 41 Antarctic grid, while the North Pole is at position (18,16) of the 38 × 26 Arctic grid.

To obtain the desired orientation in the southern hemisphere, equations (7) must be adjusted slightly:

$$X = 25(1+\sqrt{2})\ \frac{\cos\phi}{1-\sin\phi}\ \sin\lambda$$

in the southern hemisphere (10)

$$Y = 25(1+\sqrt{2})\ \frac{\cos\phi}{1-\sin\phi}\ \cos\lambda$$

Thus the South Pole is at (0,0), and 45°S (= -45°), 0°E is at (0,25).

The inverse relationships to (9) and (10) are also required. Solving the northern hemisphere equations for λ, we have

$$(Y/X) = (\sin\lambda/\cos\lambda) = \tan\lambda\ , \tag{11}$$

so that:

$$\lambda = \begin{cases} \tan^{-1}(Y/X) & \text{for } X > 0 \\ \pi + \tan^{-1}(Y/X) & \text{for } X < 0 \\ \pi/2 & \text{for } X = 0,\ Y \geq 0 \\ 3\pi/2 & \text{for } X = 0,\ Y < 0\ . \end{cases} \tag{12}$$

Solution for ϕ then proceeds, for $\lambda \neq \frac{\pi}{2}$ or $\frac{3\pi}{2}$, by setting

$$B = \frac{X}{25(1+\sqrt{2})\cos\lambda} = \frac{\cos\phi}{1+\sin\phi}\quad . \tag{13}$$

In this way

$$B^2(1+2\sin\phi + \sin^2\phi) = \cos^2\phi \; , \tag{14}$$

which can readily be solved for $\sin\phi$ by the quadratic formula. The permissible solution in the general case yields

$$\phi = \sin^{-1}\left(\frac{1 - B^2}{1 + B^2}\right) . \tag{15}$$

For $\lambda = \frac{\pi}{2}$ or $\frac{3\pi}{2}$, set

$$B = \frac{Y}{25(1+\sqrt{2})\sin\lambda} \tag{16}$$

and solve for equation (15) again, though now with the altered B. Solutions for the southern hemisphere are found similarly, the resulting longitude being:

$$\lambda = \begin{cases} \tan^{-1}(X/Y) & \text{for } Y > 0 \\ \pi + \tan^{-1}(X/Y) & \text{for } Y < 0 \\ \pi/2 & \text{for } Y = 0,\ X \geq 0 \\ 3\pi/2 & \text{for } Y = 0,\ X < 0 \end{cases} \tag{17}$$

and the resulting latitude being:

$$\phi = \sin^{-1}\left(- \frac{1 - B^2}{1 + B^2} \right) , \tag{18}$$

where

$$B = \begin{cases} \dfrac{Y}{25(1+\sqrt{2})\cos\lambda} & \text{for } \lambda \neq \frac{\pi}{2} \text{ or } \frac{3\pi}{2} \\[2ex] \dfrac{X}{25(1+\sqrt{2})\sin\lambda} & \text{for } \lambda = \frac{\pi}{2} \text{ or } \frac{3\pi}{2} \end{cases} .$$

Calculations are made on the two grids separately and are carried out only on the 41 × 41 subgrid centered on the South Pole and on the 38 × 26 subgrid positioning the North Pole at location (18,16) with respect to the lower left corner. Both grids are presented in Figure 5, along with the sea-land boundaries.

The above conversions yield a grid interval of 211.083 km on the projected plane, which translates to grid intervals on the idealized globe ranging from 211.06 km at the poles to 181.006 km at the farthest edge of the north polar region and to 173.844 km at the farthest edge of the south polar region. The global distances are obtained from the following law for spherical triangles: $\cos a = \cos b \cos c + \sin b \sin c \cos\alpha$, where a, b, c are the sides of the triangle and α is the angle opposite a.

Vertically the model includes a mixed layer in the ocean, an ice layer, a snow layer, and an atmospheric boundary layer. Figure 6 schematizes the four layers plus the allowance for leads. Depending on time and location, the snow layer or both the ice and snow layers may be nonexistent, thereby reducing the number of vertical layers from four to three or two

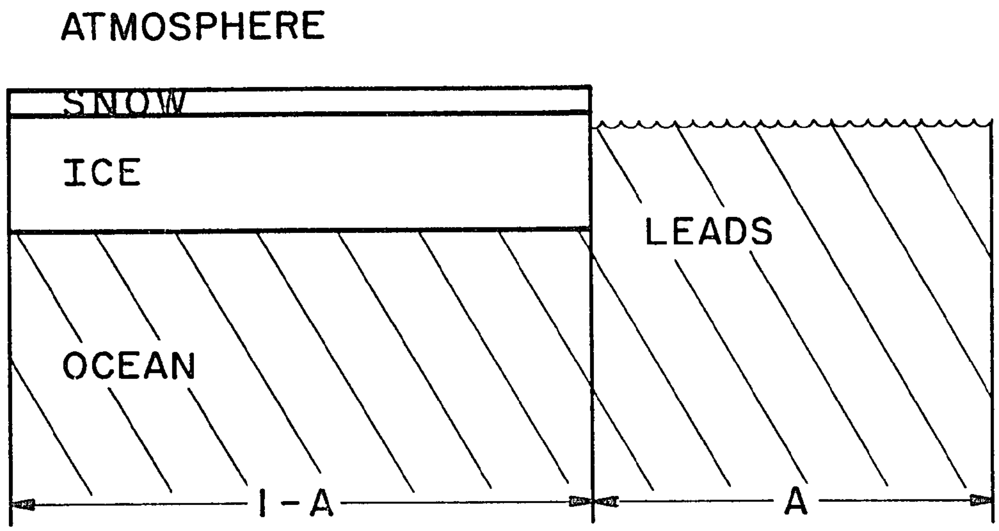

Figure 6. Schematic diagram of the major divisions within a grid square.

respectively. The remaining dimension is time, where the resolution is defined by an 8-hour timestep and the length of all months is set at a uniform 90 timesteps, i.e., 30 days.

4.2 Fields of Input Data

The thermodynamic calculations below (section 4.5) require input data fields in the form of atmospheric temperatures for sensible heat flux and incoming longwave radiation, dew points for latent heat flux, wind speeds for sensible and latent heat fluxes, and both wind velocities and dynamic topography for ice transport.

4.2.1 Atmospheric Data

The atmospheric data were obtained from long-term mean monthly distributions as given on 5° latitude-longitude grids by Taljaard *et al.* (1969) in the southern hemisphere and by Crutcher and Meserve (1970) in the northern hemisphere. The pressure, temperature, and dew point fields of both atlases were constructed from a large array of available data, the major sources being *World Weather Records, Climatological Normals for CLIMAT and CLIMAT Ship Stations for the Period 1931-60,* and marine climatic atlases, with additional sources including various national publications and the data of Antarctic research stations. The data were time and space smoothed and the geostrophic winds were computed from the smoothed pressure fields by the standard formulae:

$$u_{wg} = -\frac{1}{\rho_a f}\frac{\partial p}{\partial y}\,,$$

$$v_{wg} = \frac{1}{\rho_a f}\frac{\partial p}{\partial x}\,, \tag{19}$$

where x, y = distances along the two horizontal axes,

p = pressure,

f = the Coriolis parameter = $2\Omega\sin\phi$,

ϕ = latitude,

Ω = the speed of the earth's angular rotation = $7.292 \times 10^{-5}\ s^{-1}$,

ρ_a = air density,

u_{wg}, v_{wg} = the x and y components of the surface geostrophic wind.

The 12 monthly values of both u_{wg} and v_{wg} were time smoothed at each grid point with a 9-point filter (Jenne *et al.*, 1974).

Sixteen-point interpolation was used to convert the atlas data to the rectangular grid of the sea ice model. In this manner fields were obtained for surface air temperatures T_a, surface dew points T_d, and the u_{wg} and v_{wg} components of sea-level geostrophic winds. To conserve computer storage space during the running of the computer program, these fields were placed on magnetic tapes in a packed configuration, with the temperature and dew point at a given grid point placed in the same word location and similarly for the u_{wg} and v_{wg} wind components. The packing of the numbers forced a truncation of the data values; however, the six remaining significant figures are beyond the precision of the initial data and hence the packing itself is not a source of reduced accuracy. Figures 7-10 present contour maps and plotted wind vectors from the stored data for January and July. For increased legibility, the wind vectors are drawn at only half the grid points, and the vector lengths are scaled individually for each diagram. A unit length of the distance between grid points signifies 3 m s^{-1} in Figure 7, 2 m s^{-1} in Figure 8, and 5 m s^{-1} in Figures 9 and 10. This allows reasonably lengthened vectors in each diagram in spite of the weaker winds in the northern-hemisphere summer. Similarly, the

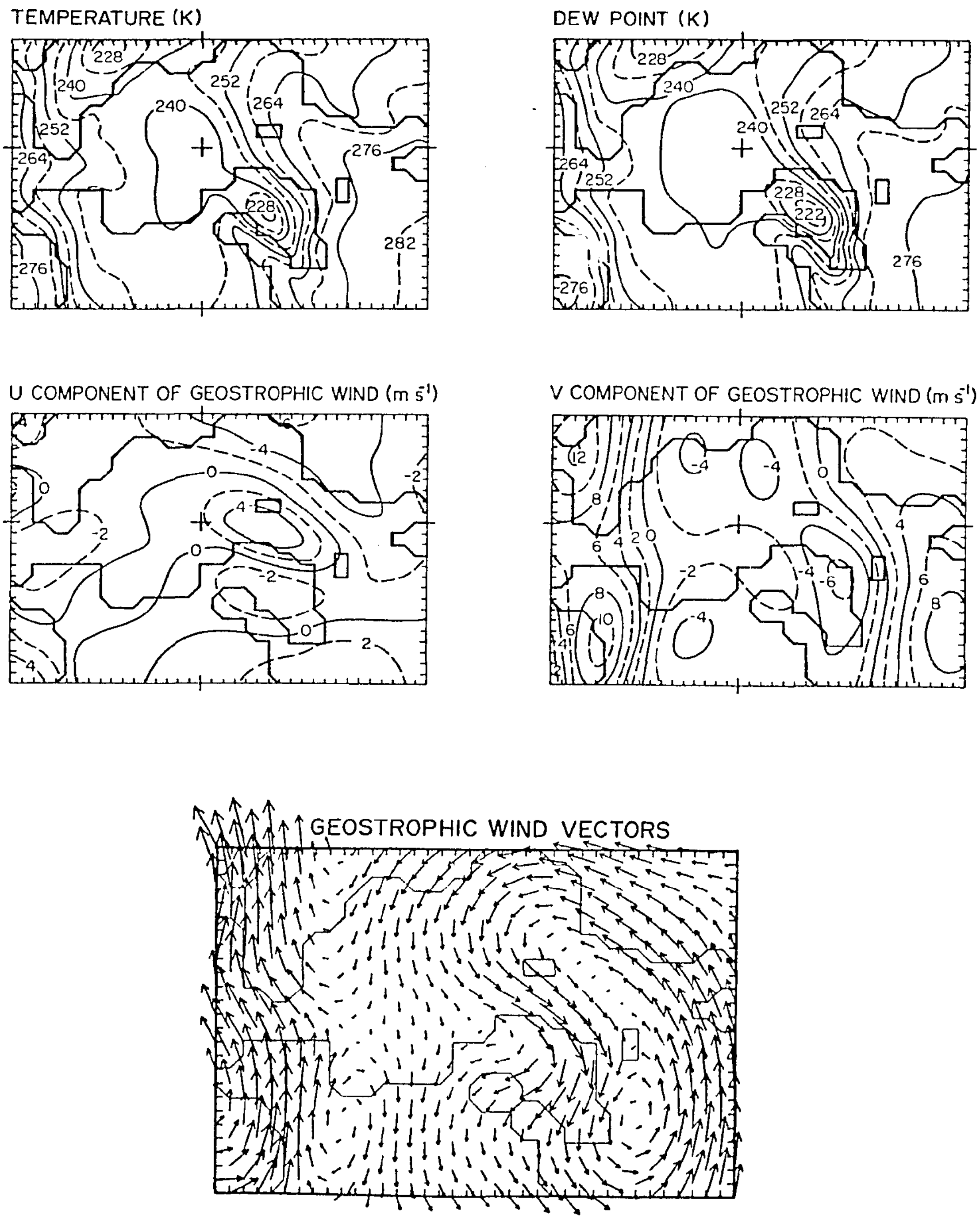

Figure 7. January atmospheric input data for the Arctic.

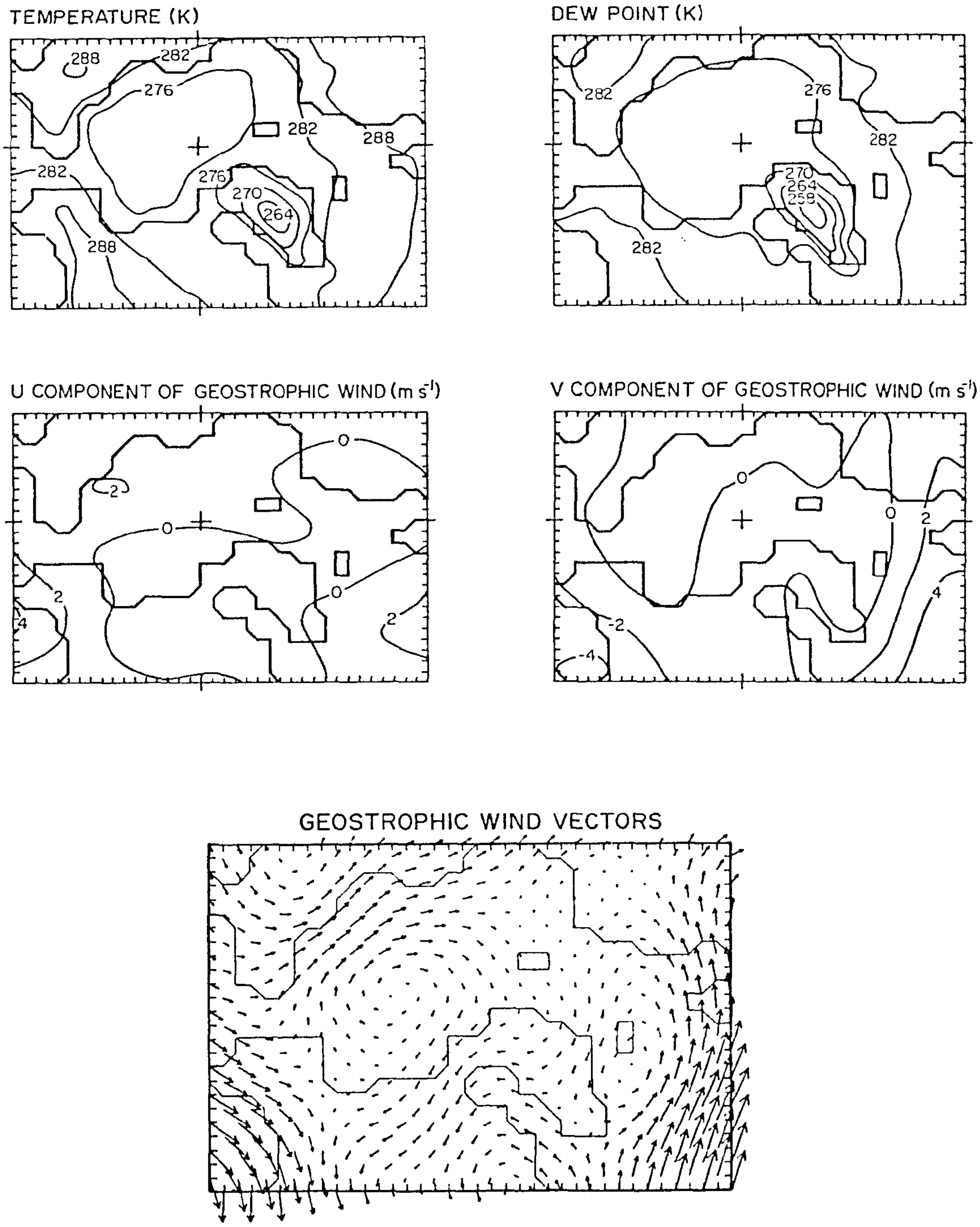

Figure 8. July atmospheric input data for the Arctic.

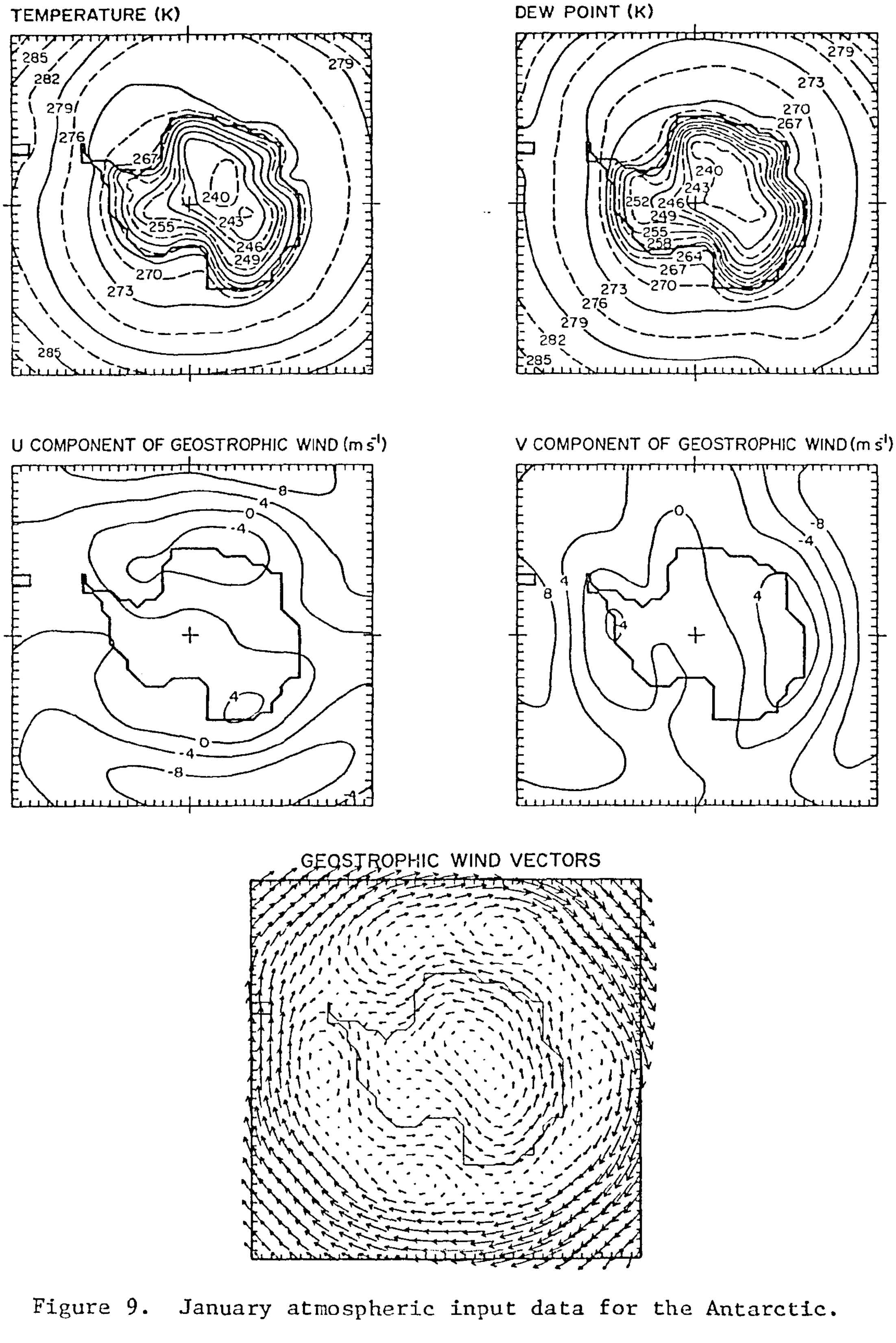

Figure 9. January atmospheric input data for the Antarctic.

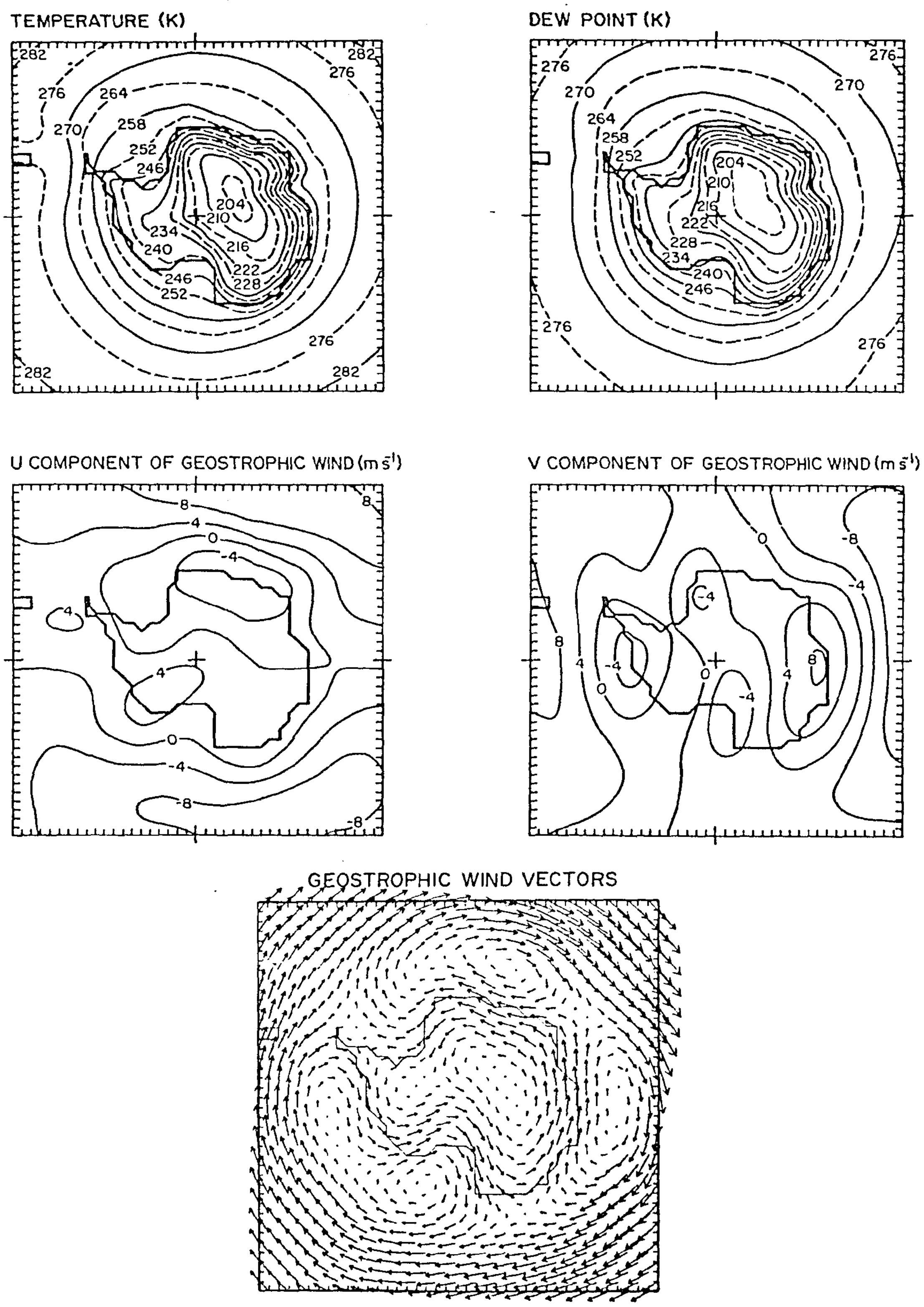

Figure 10. July atmospheric input data for the Antarctic.

contour intervals on the 16 contour maps were selected for appropriate visual presentation.

The stored atmospheric data for all 12 months are accepted as accurate at timestep 45 (midmonth), with values for other timesteps being determined by linear interpolation. The use of linear interpolation rather than a more involved calculation scheme allows the computer to retain only two months' data in its active storage space at any given time. This was found necessary to avoid overloading the core with the Antarctic data. Moreover, there is no substantial evidence that a more complicated interpolation would yield more accurate results.

4.2.2 Dynamic Topography

Input fields of dynamic topography were digitized from contour maps of A. Gordon (personal communication, 1976) in the Antarctic region and from a map of Coachman and Aagaard (1974) in the Arctic. In both hemispheres only yearly averages were available. Furthermore, the Antarctic data are considerably more complete than the Arctic data. Gordon constructed maps for three levels: 0/1000 db, 1000/2500 db, and 2500/4000 db; the three maps were digitized for the sea ice grid; and the digitized figures were summed to obtain a dynamic topography field for a full 0/4000 db layer. The summed values were space smoothed by a standard nine-point smoothing formula (weighting the central point by 4, the four adjacent points by 2, and the four diagonal points by 1), with the resulting field being that presented in Figure 11.

The limited Arctic data required more subjectivity. Figure 12 presents the dynamic topography for 0/1200 db from the Arctic Institute of North America map reproduced in Coachman and Aagaard (1974). Due to the spatial incompleteness of the field, the contour lines had to be extended subjectively. This was done by hand, maintaining the approximate patterns of a 20 m pressure field predicted by a model of the Arctic Ocean circulation (Semtner, 1976b, Figure 7; the use of this figure was suggested by B. Semtner and W. Washington). The Semtner diagram extends contours to the continental boundaries and includes the Norwegian-Barents Sea area. The patterns correspond closely with the dynamic topography field of Coachman and Aagaard in the regions for which this latter field is presented. However, neither the North Atlantic nor the North Pacific is included and so for these areas contours are sketched roughly from the patterns of ocean circulation in Sverdrup *et al.* (1961, Chart VII). The resulting Arctic dynamic topography field appears in Figure 13.

4.3 Forcing From Above the Ice or Water

As will be seen in section 4.5, the computations for thickness changes of ice and snow require fluxes of solar radiation, longwave radiation, sensible heat, and latent heat. The evaluation of each of these will be discussed in turn.

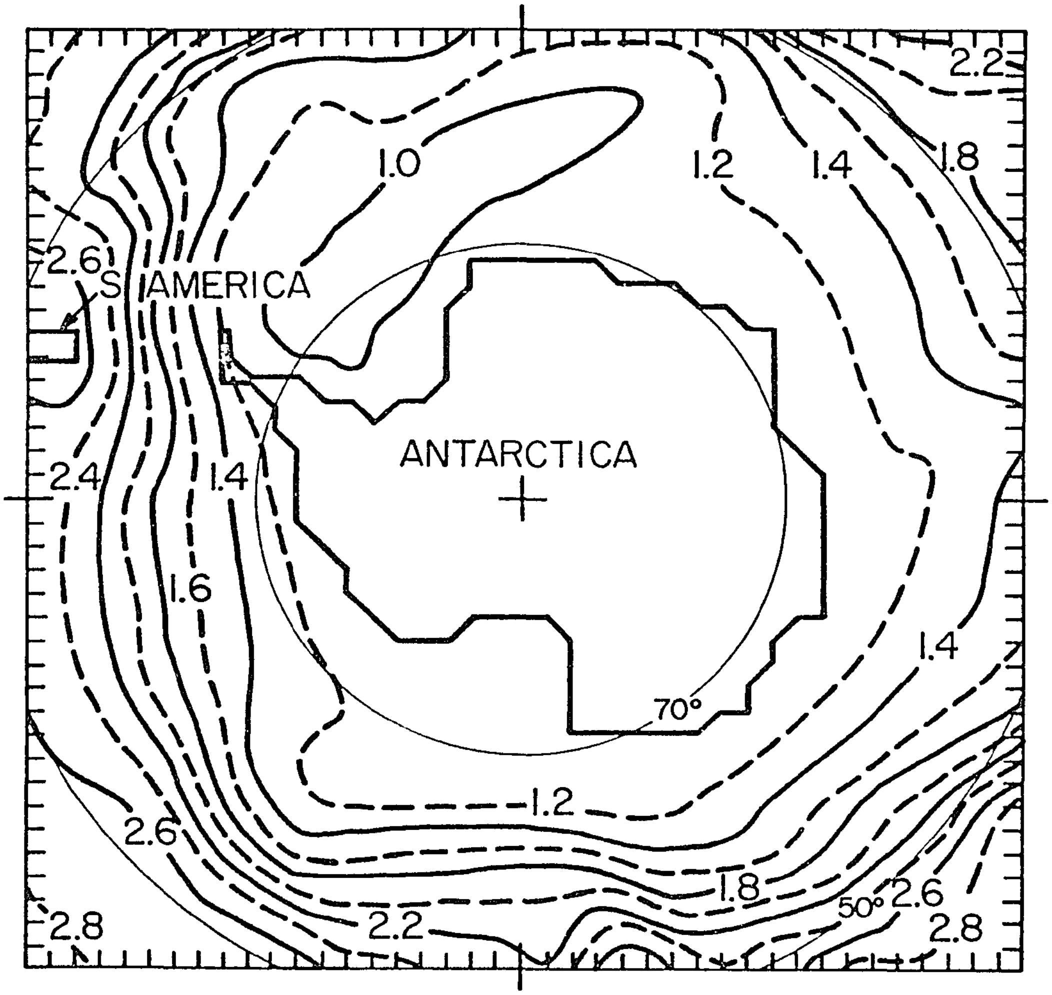

Figure 11. Contours of dynamic topography used in the Southern Ocean. Contour interval is 0.2 dynamic meters.

Figure 12. Partial dynamic topography field in the Arctic. Reproduced from Coachman and Aagaard (1974).

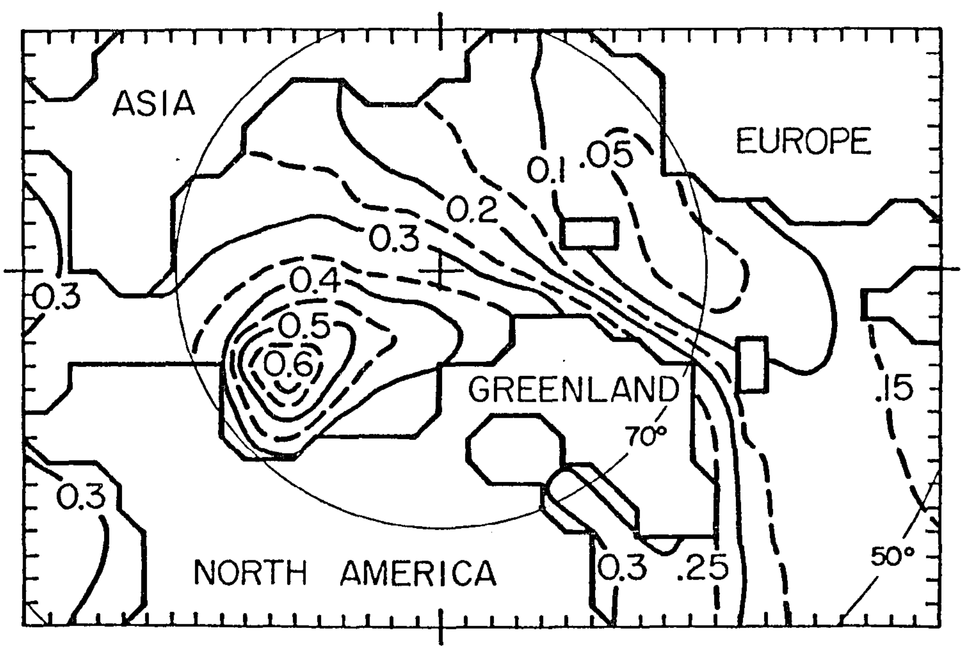

Figure 13. Contours of dynamic topography used in the Arctic. Contour interval is 0.05 dynamic meters.

4.3.1 Solar Radiation

The flux of solar radiation, SW↓, is calculated by applying the cloudiness factor of Laevastu (1960) to an empirical equation given by Zillman (1972) for global radiation under cloudless skies. The Zillman equation follows:

$$Q_o = \frac{S \cos^2 Z}{(\cos Z + 2.7)\, e \times 10^{-5} + 1.085 \cos Z + 0.10} \; . \qquad (20)$$

S signifies the solar constant, Z the solar zenith angle, and e the vapor pressure in pascals (1 pascal = 10^{-2} mb). A value of 1353 W m^{-2} has been taken for the solar constant (Thekaekara and Drummond, 1971), while the cosine of the zenith angle is calculated by the standard geometric formula

$$\cos Z = \sin\phi \sin\delta + \cos\phi \cos\delta \cos HA \qquad (21)$$

(Sellers, 1965). For this, the latitude ϕ is calculated by equations (15) or (18), while the approximate declination δ and the hour angle HA are determined as:

$$\delta = 23.44^{o} \times \cos\left[(172 - \text{day of year}) \times \pi/180\right]$$

$$HA = (12 \text{ hr} - \text{solar time}) \times \pi/12. \qquad (22)$$

The vapor pressure e is calculated by a formulation presented in subsection 4.3.4.

As already mentioned, Q_o is modified by a cloud factor in order to obtain total incoming shortwave radiation

$$Q = Q_o(1 - 0.6\ c^3) \tag{23}$$

(Laevastu, 1960). Cloud-cover figures for the Arctic have been averaged from the curves of Huschke (1969) for his four Arctic regions, these curves being frequently reproduced in the subsequent literature (e.g., Kellogg, 1974; Herman, 1975; Baker, 1976). As a result, in the Arctic the fractional cloud cover c is set at 0.50 for December through March, 0.55 for April, 0.70 for May, 0.75 for June and July, 0.80 for August and September, 0.70 for October, and 0.60 for November. The absence of spatial variation in the modeled cloud amount is felt justified by the lack of information on the actual variability. The strongest deviation between the four Huschke curves occurs in June, when the coverage in the Canadian Arctic is 60%, *versus* roughly 83% for the West Eurasian Arctic, the East Eurasian Arctic, and the Central Arctic. However, the lower values in the Canadian Arctic are at variance with a more recent contention by Herman (1975) that the frequency of low cloudiness in June remains above 70% for all regions of the Central Arctic and peripheral seas. Consequently, it was felt justified to retain only spatially averaged values.

In the Antarctic, cloud cover varies more strongly with latitude than season and so the modeled cloud values are a function of both latitude and month. The basis of the calculations are the January and July curves of van Loon (1972) for cloud cover *versus* latitude. By use of a Lagrangian interpolating polynomial, January fractional cloud cover was related to latitude through a fourth order polynomial satisfying the functional values of van Loon at 40°, 50°, 60°, 70°, and 80°S. The same was done for July cloud cover, the resulting polynomials being:

$$0.000001291677\phi^4 - 0.000312502540\phi^3 + 0.0271210643\phi^2 - 0.995259206\phi + 13.6901356 \text{ for January}$$

and

$$0.000001205\phi^4 - 0.0002934\phi^3 + 0.0255645\phi^2 - 0.94371\phi + 13.138 \text{ for July.}$$

Both polynomials are plotted in Figure 15, with the original curves from van Loon plotted in Figure 14. Cloud cover amounts for intervening months are obtained through linear interpolation. A point of caution regarding the calculated polynomials: these were derived specifically for high southern latitudes and should not be used for locations north of 40°S.

At each grid point, determination of SW↓ proceeds by performing the above calculations at the centers of two 1-hour and eleven 2-hour periods, multiplying by the relevant time length (one or two hours), summing for the day, and then dividing by 24 hours. Due to the computer time involved, solar radiation is recalculated only every 11 timesteps (3.75 days).

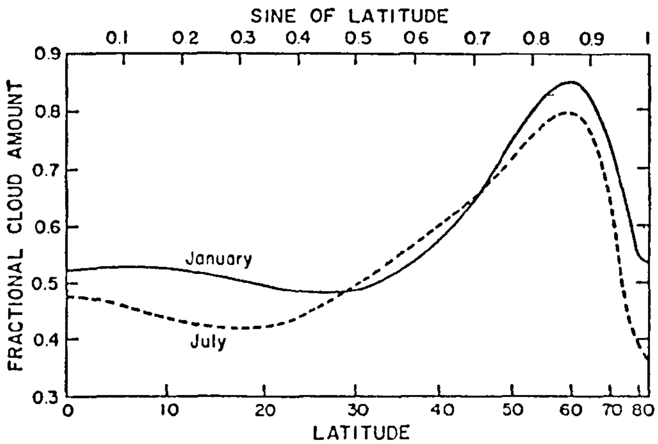

Figure 14. Zonally averaged percent cloud cover in the southern hemisphere, courtesy of van Loon (1972, p. 102).

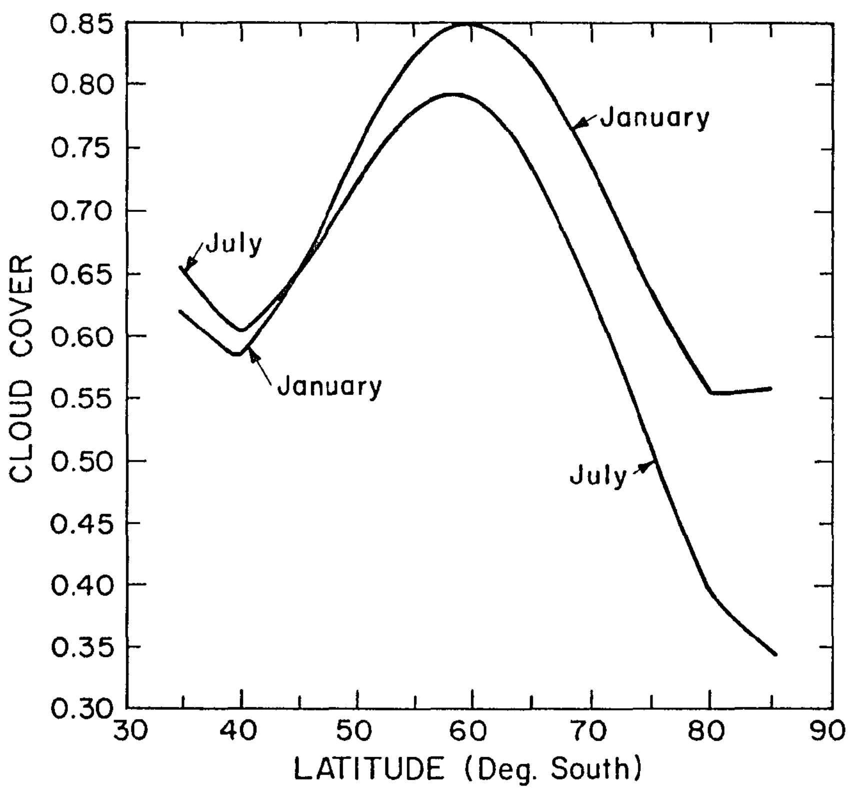

Figure 15. Cloud cover percentages used for the southern hemisphere in January and July, presented as a function of latitude.

4.3.2 Incoming Longwave Radiation

Incoming longwave radiation is calculated each timestep from Idso and Jackson's formula (1969) for clear skies:

$$F\downarrow = \sigma T_a^4 \{1 - 0.261 \exp [-7.77 \times 10^{-4} (273 - T_a)^2]\} , \tag{24}$$

modified by a cloudiness factor of $1 + cn$. The Idso and Jackson formula was developed as valid for all latitudes and all naturally occurring screen-level air temperatures T_a. Eight hundred and thirty half-hourly means from Point Barrow, Alaska were included in the verification procedure, which yielded a final correlation coefficient of 0.992 between the observed data and values from equation (24) (Idso and Jackson, 1969). In the current calculations, the Stefan-Boltzmann constant σ is 5.67×10^{-8} W m^{-2} K^{-4}, while the surface air temperatures T_a are those discussed under Fields of Input Data (section 4.2), cloud cover values c are those presented under Solar Radiation (section 4.3.1), and n is an empirical factor set at 0.275 as averaged from the drifting station values of Marshunova (1966).

4.3.3 Sensible Heat

The flux of sensible heat is calculated each timestep from the standard bulk aerodynamic formula:

$$H\downarrow = \rho_a c_p C_H V_{wg} (T_a - T_{sfc}) \tag{25}$$

with ρ_a = air density,

c_p = specific heat of air = 1004 J kg^{-1} K^{-1} (dry air value, Huschke, 1959),

C_H = transfer coefficient for sensible heat,

V_{wg} = surface geostrophic wind speed,

T_a = surface air temperature,

T_{sfc} = surface ice-snow-water temperature.

Following recent AIDJEX usage, both C_H and the latent heat transfer coefficient C_E are approximated at 1.75×10^{-3} (Maykut, 1977). Air temperature T_a and geostrophic wind speed $V_{wg} = \sqrt{u_{wg}^2 + v_{wg}^2}$ are taken from the fields of atmospheric input data described in section 4.2.1, while T_{sfc} is calculated from a surface energy balance equation to be presented under Thermodynamic Calculations (section 4.5).

Air density is obtained from the equation of state:

$$\rho_a = \frac{p}{R\,T_a} \tag{26}$$

with R = 287 J kg^{-1} K^{-1} the gas constant for dry air (Haltiner and Martin, 1957). As pressure is neither stored nor calculated in the current program, equation (26) is solved using a constant p = 98800 Pa in the southern hemisphere and a constant p = 101400 Pa in the northern hemisphere. These pressures were selected from annual mean sea level pressures of 98540, 98850, 101310, and 101500 Pa at 65°S, 60°S, 70°N, and 80°N, respectively, supplied by H. van Loon and R. Jenne (personal communication, 1977).

4.3.4 Latent Heat

As in the calculations for sensible heat, calculations for the flux of latent heat proceed each timestep with a bulk aerodynamic formula. Symbolically,

$$LE\downarrow = \rho_a L C_E V_{wg}(q_{10m} - q_s) \; , \tag{27}$$

L being the latent heat of vaporization (2.5×10^6 J kg^{-1}) or of sublimation (2.834×10^6 J kg^{-1}), depending on whether an ice cover exists (Haltiner and Martin, 1957), and the q's being specific humidities at 10 m and the surface. The formulae for specific humidities are:

$$q_{10m} = \frac{\varepsilon e}{p - (1 - \varepsilon)e}$$

and (28)

$$q_s = \frac{\varepsilon e_s}{p - (1 - \varepsilon)e_s} \; ,$$

where $\varepsilon = 0.622$ is the ratio of the molecular weight of water vapor to that of dry air (Oliger *et al.*, 1970; Hess, 1959). Symbolizing the surface dew point temperature in kelvins as T_d, the empirical formulae used for vapor pressure e and saturation vapor pressure e_s, both in pascals, become:

$$e = \begin{cases} 611.0 \times 10^{9.5(T_d-273.16)/(T_d-7.66)} & \text{if an ice cover exists} \\ 611.0 \times 10^{7.5(T_d-273.16)/(T_d-35.86)} & \text{if no ice cover exists} \end{cases} \tag{29}$$

and

$$e_s = \begin{cases} 611.0 \times 10^{9.5(T_{sfc}-273.16)/(T_{sfc}-7.66)} & \text{if an ice cover exists} \\ 611.0 \times 10^{7.5(T_{sfc}-273.16)/(T_{sfc}-35.86)} & \text{if no ice cover exists.} \end{cases} \tag{30}$$

The reference for equations (30) is Murray (1967).

4.4 Forcing From Below the Ice

The upper layer of the ocean tends to be well-mixed in both temperature and salinity. The present model assumes the depth of this mixed layer to be 30 m and calculates changes in water temperature based on this depth (section 4.6). However, in the standard case the temperature and other mixed-layer properties are not used to determine the upward heat flux, but instead the energy flux $F\uparrow$ to the ice from the water beneath is taken to be a constant 2 W m^{-2} in the Arctic and a constant 25 W m^{-2} in the Antarctic. The reasoning behind this simplification is based on the inadequate information for alternate formulations and the feeling that, in view of this inadequacy, more involved calculations are likely not more accurate. The following paragraphs describe some of the difficulties.

In studies by Pease (1975), Bryan *et al.* (1975), and Welander (1977), the flux from the mixed layer is directly proportional to the temperature difference between the water and the ice. This follows from a scale analysis of the First Law of Thermodynamics and was attempted in the present model also. However, the numerical value of the proportionality factor is not given by Welander; in Bryan *et al.* it equals 209.5 W m^{-1} K^{-1}/z_1, with z_1 the depth of the top layer of the ocean; and in Pease it alternately equals 1050 W m^{-2} K^{-1}, 524 W m^{-2} K^{-1}, and 105 W m^{-2} K^{-1}. As Pease (1975) indicates, the coefficient depends multiplicatively on the arbitrary eddy diffusivity of water; hence the wide uncertainty in a proper value.

N. Untersteiner (personal communication, 1976) and G. Maykut (personal communication, 1977) object to the calculation of the oceanic heat flux as proportional to the temperature difference between water and ice, contending that the temperature directly under the ice remains practically at freezing until the ice disappears. Indeed, this was found to be true in the calculated temperatures of the present model (see section 7.3).

Furthermore, although only temperatures have been mentioned so far, an accurate calculation of the energy flux from ocean to ice would require incorporation of ocean salinity and a variable mixed-layer depth as well. Salt content of the upper ocean is significantly affected by the freezing of water and the melting of ice and in turn affects the vertical density structure of the ocean. As water freezes in the real world, the discharge of salt to the ocean beneath increases the density of the mixed layer and hence increases the chance of an unstable stratification and resulting convection with underlying water. The convection alters the depth, the temperature, and the salinity of the mixed layer, the amount of alteration depending on the initial temperature and salinity profiles *versus* depth. Unfortunately, these profiles vary widely with location and season. This is well-quantified in Antarctic waters by data from several *Eltanin* cruises (Jacobs *et al.*, 1974), and it is well-recognized in Arctic waters, in particular due to the inflow of the Atlantic layer through the Greenland-European sector.

Thus a parameterization including the salinity influence would require three-dimensional fields of temperature and salinity. Although computer space prevented insertion of such fields for the present model, presumably upon coupling with an ocean model these fields will be available. This would allow a more realistic parameterization of ice-ocean interactions, though the problem of uncertain eddy diffusivities would remain. In the meantime, it is felt that a constant ocean heat flux is the best choice for the current standard case. The task then becomes to determine a proper constant.

In their one-dimensional model, Maykut and Untersteiner (1971) use 2 W m^{-2} for the oceanic heat flux in the central Arctic, having tested values of 0, 1, 2, 4, 6, and 8 W m^{-2}. The choice of 2 W m^{-2} for their standard case was predominantly based on its yielding the most satisfactory results. Since estimates of the flux vary and are all based on indirect evidence, this was probably as legitimate a criterion as any. With $F\uparrow$ = 8 W m^{-2}, the ice vanished before equilibrium was reached.

In the Antarctic, as in the Arctic, accurate ocean flux values are simply not known. However, typical fluxes from water to ice are believed to be much greater than in the Arctic, and A. Gordon (personal communication, 1976) suggested values up to 25 W m^{-2}. The selection of 25 W m^{-2} for the current model followed the testing of three values and the judgement that the results looked reasonable with $F\uparrow$ = 25 W m^{-2}. By contrast, the selection of 2 W m^{-2} for the Arctic simulation strictly followed the usage of Maykut and Untersteiner (1971) and was not preceded by testing alternatives.

4.5 Thermodynamic Calculations

Calculations of changes in thickness of the ice and snow layers are based on energy balances at the various interfaces. In grid squares with no ice, energy balances determine the change in ocean temperature instead.

4.5.1 Case of No Ice

The no-ice situation is depicted in Figure 16, where the net energy flux into the mixed oceanic layer is

$$Q_{net} = H\downarrow + LE\downarrow + \varepsilon_w LW\downarrow + (1-\alpha_w)SW\downarrow + F_w\uparrow - \varepsilon_w \sigma T_w^{\ 4} \ . \qquad (31)$$

The evaluations of $H\downarrow$, $LE\downarrow$, $LW\downarrow$, $SW\downarrow$ have been presented earlier, while the flux $F_w\uparrow$ to the mixed layer from the deeper ocean is here taken as 0. All terms in the expression for Q_{net} are for the current timestep, except the water temperature T_w, which is for the previous timestep. The shortwave albedo α_w of water is set at 10%, and, following Pease (1975), the longwave emissivity ε_w is set at 97%. The albedo figure is the same as that used by Badgley (1966) for Arctic leads, by Donn and Shaw (1966) for an average over an open polar ocean, and by Langleben (1972) for along the Arctic coastline. It also corresponds well with the integrated daily albedos of Parkinson (1974).

The entire net inflow Q_{net} goes toward raising the temperature of the water, so that the time rate of change of internal energy (per unit horizontal area) becomes

$$\frac{dI}{dt} = Q_{net} \ . \qquad (32)$$

Internal energy I is the product of the 30 m mixed-layer depth d_{mix}, the volumetric heat capacity of water $c_w = 4.19$ MJ m^{-3} K^{-1}, and the water temperature. Applying a finite difference

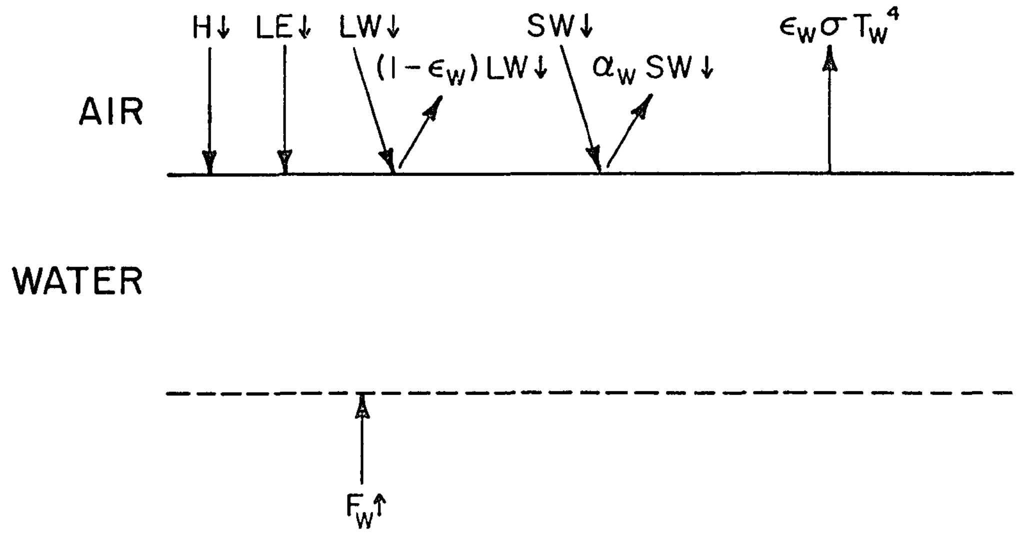

Figure 16. Schematic diagram of the energy fluxes for the case of no ice.

approximation to equation (32), we obtain a resulting temperature change of

$$\Delta T_w = \frac{\Delta t \times Q_{net}}{d_{mix} \times c_w} \tag{33}$$

where Δt is the 8-hour timestep. As heat is spread uniformly throughout the mixed layer, the new water temperature equals

$$T_{w,i} = T_{w,i-1} + \Delta T_w \tag{34}$$

where subscripts i and i-1 refer to the timestep. Note that if Q_{net} is negative in (33), then the temperature is reduced, as desired. Should T_w fall below 271.2 K, then a portion of the water is assumed to freeze. The thickness of the newly frozen ice is set at h_n = 0.01 m and the extent is calculated to release the amount of heat necessary to maintain the water temperature at freezing. The fraction of the grid square covered by ice then becomes

$$\frac{(T_B - T_w) \times d_{mix} \times c_w}{Q_I \times h_n}$$

where Q_I is the heat of fusion of ice, set at 302 MJ m^{-3}. The new ice is modeled to have a surface temperature of 271.2 K.

4.5.2 Case of Ice With No Snow

The fluxes involved in the case of ice with no snow are diagrammed in Figure 17. The only flux through the ice which is specifically modeled is the conductive one, though in reality a fraction I_o of the net incident shortwave radiation penetrates into the uncovered upper surface. Maykut and Untersteiner (1971) assume I_o = 17%. This penetrating radiation normally causes the brine volume to increase and the cooling near the upper surface to be delayed. The present model follows the 0-layer model of Semtner (1976a) in parameterizing this by using 60% of I_o as heating in the surface energy budget and ignoring the remaining 40%. In essence, the ignored 40% is treated as reflected radiation, i.e., as an

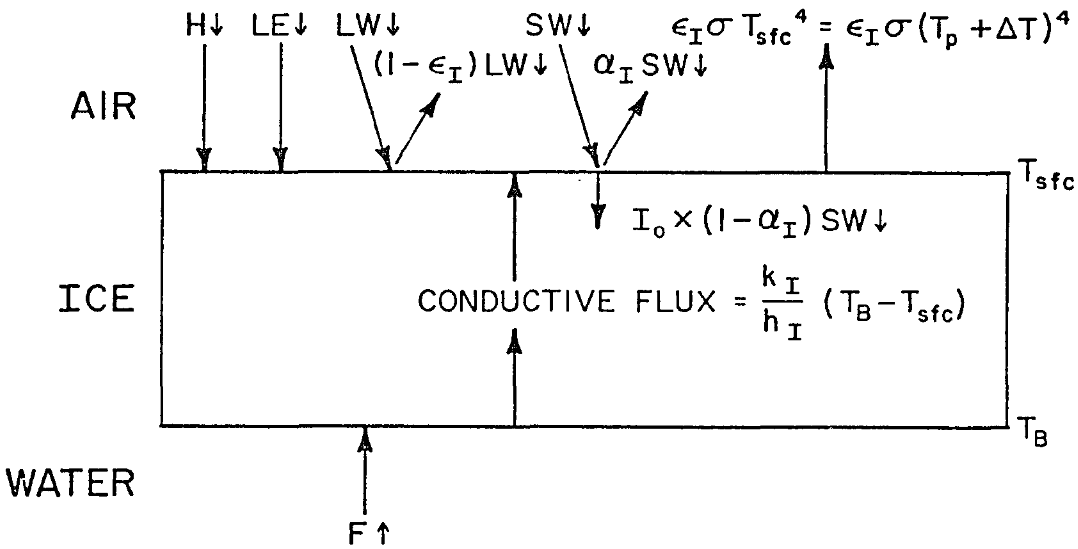

Figure 17. Schematic diagram of the energy fluxes for the case of ice with no snow.

effective increase in the shortwave albedo.

The conductive flux through the ice equals $k_I(T_B - T_{sfc})/h_I$, as in the work of Bryan *et al.* (1975), Pease (1975), and Semtner (1976a). The thickness of the ice, h_I, is taken from the previous timestep, while the thermal conductivity of the ice, k_I, is set at a constant 2.04 W m^{-1} K^{-1}, and the temperature at the bottom of the ice, T_B, is assumed to be the freezing point of sea water. Following Maykut and Untersteiner (1971) and Bryan *et al.* (1975), this freezing point is 271.2 K. The remaining value in the expression for conductive flux, surface temperature T_{sfc}, will now be calculated from the surface energy balance, the basic assumption being that the temperature at the surface adjusts itself in a manner maintaining that balance.

From Figure 17, the surface energy balance is as follows:

$$H\downarrow + LE\downarrow + \varepsilon_I LW\downarrow + (1-0.4I_o)(1-\alpha_I)SW\downarrow - \varepsilon_I \sigma T_{sfc}{}^4 + \frac{k_I}{h_I}(T_B - T_{sfc}) = 0. \tag{35}$$

The longwave emissivity of the ice, ε_I, is set at 0.97, and the shortwave ice albedo α_I is set at 0.50. As is done in Semtner (1976a), equation (35) is linearized by setting $T_{sfc} = T_p + \Delta T$ (where T_p = the temperature at the surface during the previous timestep) and approximating the power $T_{sfc}{}^4 = (T_p + \Delta T)^4$ by the two largest terms, i.e.,

$$T_{sfc}{}^4 \approx T_p{}^4 + 4T_p{}^3 \Delta T . \tag{36}$$

This reduces the surface energy balance to

$$H\downarrow + LE\downarrow + \varepsilon_I LW\downarrow + (1-0.4I_o)(1-\alpha_I)SW\downarrow - \sigma\varepsilon_I(T_p{}^4 + 4T_p{}^3\Delta T)$$

$$+ \frac{k_I}{h_I}(T_B - T_p - \Delta T) = 0 \tag{37}$$

which is immediately solved for:

$$\Delta T = \frac{H\downarrow + LE\downarrow + \varepsilon_I LW\downarrow + (1-0.4I_o)(1-\alpha_I)SW\downarrow - \varepsilon_I\sigma T_p{}^4 + \frac{k_I}{h_I}(T_B - T_p)}{4\varepsilon_I\sigma T_p{}^3 + \frac{k_I}{h_I}} . \tag{38}$$

If the resulting $T_{sfc} = T_p + \Delta T$ exceeds the 273.05 K melting point of ice, then T_{sfc} is set at 273.05 K exactly and the excess energy is used to melt a portion of the ice rather than to raise its temperature beyond 273.05 K. The amount melted is determined by recalculating, with the new surface temperature of 273.05 K, the summed fluxes to the upper ice surface. As this sum represents the energy available for melting, the calculated melt equals

$$-\Delta h_I = \frac{\Delta t}{Q_I} \left[H\downarrow + LE\downarrow + \varepsilon_I LW\downarrow + (1-0.4I_o)(1-\alpha_I)SW\downarrow - \varepsilon_I \sigma T_{sfc}^4 + \frac{k_I}{h_I}(T_B - T_{sfc}) \right] . \tag{39}$$

On the other hand, if the calculated $T_{sfc} = T_p + \Delta T$ yields a $T_{sfc} \leq 273.05$ K, then no ablation occurs and instead snow is allowed to fall at a specified rate for the given month. The prescribed snow accumulation rate in the Antarctic region is 1.1574×10^{-9} m s^{-1} from the start of March through the end of November and 0 m s^{-1} for the remaining three months. In the Arctic, the rates follow those of Maykut and Untersteiner (1969) and are presented, along with the Antarctic values, in Table 4.

With ablation and accretion at the top of the ice determined, consideration turns to the bottom of the ice. Reasoning as in the case of the upper surface, we find the melt at the bottom equals

TABLE 4. Monthly values of prescribed snowfall rates.

	Arctic Snowfall ($\times 10^{-9}$ m s^{-1})		Antarctic Snowfall ($\times 10^{-9}$ m s^{-1})	
January	3.215	(= 8.33 mm mo^{-1})	0.0	(= 0 mm mo^{-1})
February	3.215	(= 8.33 mm mo^{-1})	0.0	(= 0 mm mo^{-1})
March	3.215	(= 8.33 mm mo^{-1})	1.1574	(= 3 mm mo^{-1})
April	3.215	(= 8.33 mm mo^{-1})	1.1574	(= 3 mm mo^{-1})
May	19.290	(= 50 mm mo^{-1})	1.1574	(= 3 mm mo^{-1})
June	0.0	(= 0 mm mo^{-1})	1.1574	(= 3 mm mo^{-1})
July	0.0	(= 0 mm mo^{-1})	1.1574	(= 3 mm mo^{-1})
August			1.1574	(= 3 mm mo^{-1})
A1-19	0.0	(= 0 mm mo^{-1})		
A20-30	49.603	(= 128.57 mm mo^{-1})		
September	49.603	(= 128.57 mm mo^{-1})	1.1574	(= 3 mm mo^{-1})
October	49.603	(= 128.57 mm mo^{-1})	1.1574	(= 3 mm mo^{-1})
November	3.215	(= 8.33 mm mo^{-1})	1.1574	(= 3 mm mo^{-1})
December	3.215	(= 8.33 mm mo^{-1})	0.0	(= 0 mm mo^{-1})
		400 mm yr^{-1}		27 mm yr^{-1}

$$-\Delta h_I = \frac{\Delta t}{Q_I} \left[F\uparrow - \frac{k_I}{h_I} (T_B - T_{sfc})\right] \quad . \tag{40}$$

This equation allows the possibility of a negative "melt," translating simply to ice accretion rather than ablation.

4.5.3 Case of Snow-Covered Ice

The fluxes relevant to snow-covered ice are diagrammed in Figure 18. Due to the high extinction coefficient of snow [Schlatter (1972) suggests extinction coefficients of 10 m^{-1} and 8 m^{-1} for dry and saturated snow respectively; these compare to 1.5 m^{-1} for ice (Maykut and Untersteiner, 1969)], no penetration of shortwave radiation is allowed. Thus the I_o parameterization needed in section 4.5.2 is avoided here, and the only fluxes through the ice and snow layers are the conductive ones. With T_B, T_I, and T_{sfc} equaling the

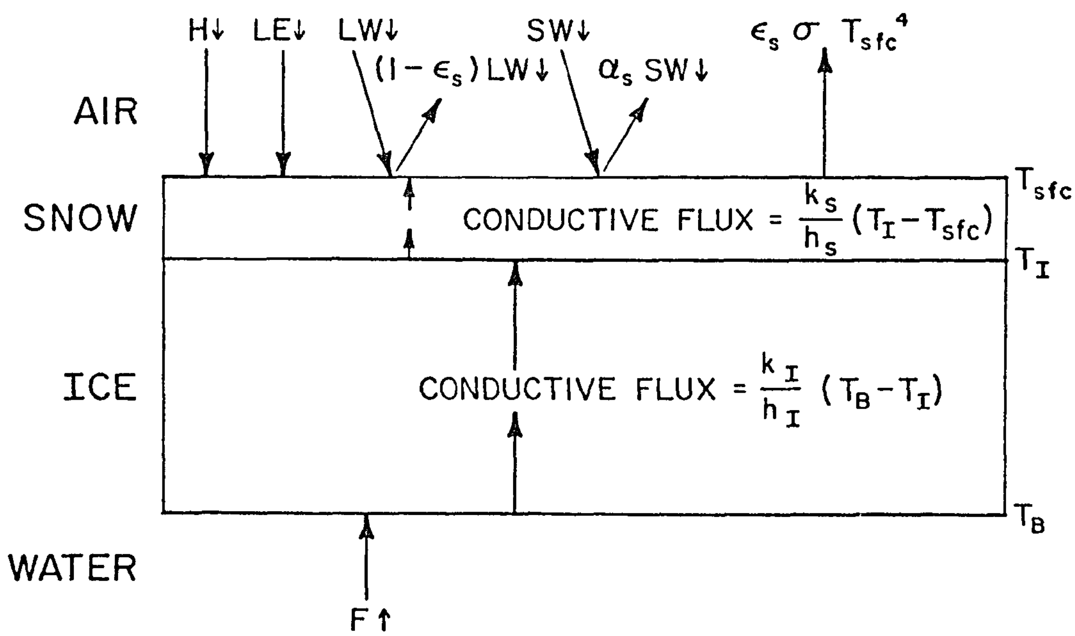

Figure 18. Schematic diagram of the energy fluxes for the case of snow-covered ice.

temperatures at the bottom of the ice, at the snow-ice interface, and at the surface of the snow, the conductive fluxes become

$$G_I = k_I(T_B - T_I)/h_I \tag{41}$$

and

$$G_s = k_s(T_I - T_{sfc})/h_s \ . \tag{42}$$

Snow conductivity k_s equals 0.31 W m^{-1} K^{-1}, while the shortwave albedo α_s of snow is set at 0.75 and the longwave emissivity ε_s is set at 0.99. Values for h_I and h_s, the ice and snow thicknesses, come from the previous timestep.

With those preliminaries, the energy balance at the snow surface becomes:

$$H\downarrow + LE\downarrow + \varepsilon_s LW\downarrow + (1-\alpha_s)SW\downarrow - \varepsilon_s \sigma T_{sfc}^4 + \frac{k_s}{h_s}(T_I - T_{sfc}) = 0 \tag{43}$$

and that at the snow-ice interface becomes:

$$\frac{k_s}{h_s}(T_I - T_{sfc}) = \frac{k_I}{h_I}(T_B - T_I) \ . \tag{44}$$

In order to solve these equations, T_{sfc} is replaced by $T_p + \Delta T$, and $(T_p + \Delta T)^4$ is again approximated by $T_p^4 + 4T_p^3\Delta T$. This leads to two equations linear in the two unknowns T_I and ΔT. Solving, we have

$$\Delta T = \frac{H{\downarrow}+LE{\downarrow}+\varepsilon_s LW{\downarrow} + (1-\alpha_s)SW{\downarrow} - \varepsilon_s \sigma T_p^{\,4} + \dfrac{k_s k_I (T_B - T_p)}{k_s h_I + h_s k_I}}{4\varepsilon_s \sigma T_p^{\,3} + \dfrac{k_I k_s}{k_s h_I + k_I h_s}} \tag{45}$$

and

$$T_I = \frac{k_s h_I (T_p + \Delta T) + h_s k_I T_B}{k_s h_I + h_s k_I} \quad . \tag{46}$$

Should the calculated ΔT result in a new snow-surface temperature $T_{sfc} = T_p + \Delta T$ greater than the melting point for snow, 273.15 K, then the excess energy goes toward melting the snow rather than increasing the temperature, so that T_{sfc} will be set back at 273.15 K and T_I will be calculated from that. The depth of melted snow equals

$$-\Delta h_s = \frac{\Delta t}{Q_s}\,[H{\downarrow} + LE{\downarrow} + \varepsilon_s LW{\downarrow} + (1-\alpha_s)SW{\downarrow}$$

$$-\varepsilon_s \sigma T_{sfc}^{\,4} + \frac{k_s}{h_s}\,(T_I - T_{sfc})] \quad , \tag{47}$$

for which the heat of fusion of snow Q_S has been set at 110 MJ m^{-3}.

In the event of a calculated snow-surface temperature T_{sfc} below 273.15 K, no snow melts but additional snow is added at the rate of snow accumulation specified for the given month (Table 4). Similarly, thickness changes at the bottom of the ice follow equivalently to those in the no-snow case (section 4.5.2), i.e.,

$$\Delta h_I = \frac{\Delta t}{Q_I} \times \left[\frac{k_I}{h_I} (T_B - T_I) - F\uparrow \right] \quad , \tag{48}$$

this being accretion if positive and ablation if negative.

4.6 Lead Parameterization and Calculation of Water Temperatures

On-site measurements have indicated that heat and moisture fluxes over sea water at the freezing point can be two orders of magnitude greater than over sea ice (Ackley and Keliher, 1976; Zwally *et al.*, 1976; Muench and Ahlnas, 1976). In fact where ice-free water covers over 1% of the total surface area, the large-scale turbulent heat exchanges can be dominated by the leads (Maykut, 1976). Consequently, the present model includes the parameter A registering at each grid point the percentage of the horizontal grid area covered by open water or leads. Changes in A occur as ice either melts laterally or forms at the lead surface, the magnitude of the change depending on the net energy flux into the lead itself and on the temperature of the water.

Each grid square has two water temperatures in the mixed layer, one, T_W, being the temperature of the water in the leads and the other, $T_{W'}$, being the temperature of the water under the ice. During any given timestep each of these temperatures is altered in a maximum of three steps. For $T_{W'}$, the first step results from the vertical melting of the ice (section 4.6.1), the second from a lateral freezing of water and hence an increase in the area of ice coverage (section 4.6.4), and the third from a partial mixing with the water in the leads (section 4.6.5). Alterations in T_w arise from the net vertical energy input into the lead (sections 4.6.3 and 4.6.4), from lateral melting and the consequent increase of the lead area (section 4.6.3), and from mixing with the water under the ice (section 4.6.5). The two sets of three-step calculations are intertwined with themselves and with the change in lead area, and hence will be presented here in the order of calculation.

4.6.1 Temperature Adjustments For Vertical Melting

If the calculations on ice thickness (sections 4.5.2 and 4.5.3) result in a melting of the ice, the melt water is assumed to mix into the water underneath and thereby readjust the mixed-layer temperature (Figure 19). The temperature of the melted water is taken as a constant 271.2 K and the ice density ρ_i is taken as a constant 900 kg m^{-3}, the midpoint of the 890-910 kg m^{-3} range given by Rigby and Hanson (1976). Since water-density measurements have been made in both hemispheres with slightly different results, the mixed-layer density in the Antarctic is set at 1027 kg m^{-3}, from the 1026-1028 kg m^{-3} range given for surface water densities south of 50°S in the Soviet *Atlas of Antarctica* (Tolstikov, 1966, plates 113, 188, 203, 221, 224),

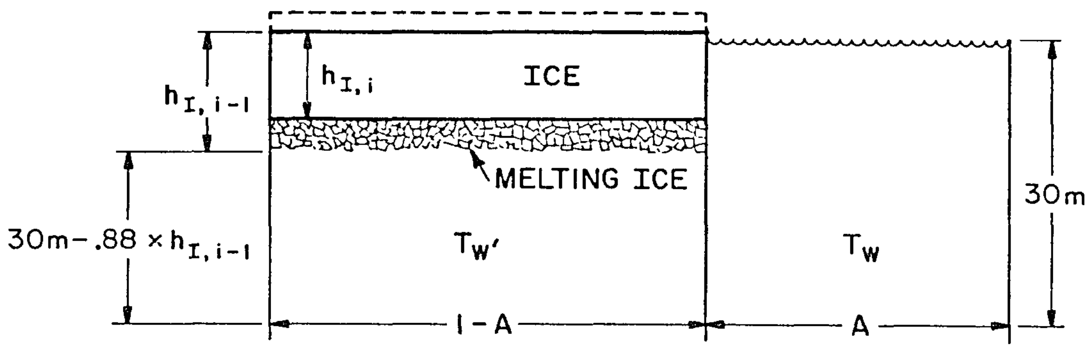

Figure 19. Variables involved in calculating temperature changes due to vertical melt.

and the mixed-layer density in the Arctic is set at 1025 kg m^{-3}, rounded from the 33-month mean mixed-layer density of 1025.15 kg m^{-3} found by Smith and English (1974) from measurements under Ice Island T-3 in the Arctic between January 1970 and September 1972. The 1025 kg m^{-3} density is also the value given by Neumann and Pierson (1966) for average surface sea water density and by Solomon (1969). With the above densities, to two decimal places the ice density/water density ratio in both hemispheres is 0.88 and thus by Archimedes' Principle, 88% of the ice sits below the air-water interface. Consequently, upon adding the melt water to the mixed layer, the new volume-weighted temperature $T_{W'}$ becomes:

$$T_{w',i} = \frac{T_{w',i-1}(d_{mix} - .88h_{I,i-1}) + 271.2\ K \times .88(h_{I,i-1} - h_{I,i})}{d_{mix} - .88 \times h_{I,i}} \quad . \tag{49}$$

The subscript i or i-1 appended to a variable normally refers to the number of the timestep. The exception comes when a variable W is recalculated more than once during a given timestep and both W_i and W_{i-1} occur within the same calculation. In that case W_i refers to the latest calculated value of W (perhaps the one currently being calculated, as for $T_{w'}$ in equation 49) and W_{i-1} refers to the latest previous value. A nonsubscripted variable automatically indicates its latest value.

4.6.2 Vertical Energy Input to the Lead

Reasonably, the energy flux to the lead area is the same as to the open water area (Figure 16). Thus the energy per unit horizontal area which vertically enters the lead during a given timestep is:

$$Q_o = \Delta t \times [(1-\alpha_w)SW\downarrow + H\downarrow + LE\downarrow + \varepsilon_w LW\downarrow - \varepsilon_w \sigma T_w^4 + F_w\uparrow] \ . \tag{50}$$

Where no ice exists within a grid square (section 4.5.1), the total energy input, positive or negative, contributes to temperature changes in the mixed layer. Here however, positive energy input will be partially used to laterally melt the ice. Briefly, if Q_o is positive then the water is warmed and the lead area increased, while if Q_o is negative then the water is cooled, and, should the temperature sink to freezing, some water freezes to ice, reducing the lead area. To present the actual amounts of temperature and lead changes, we set A_{sq} equal to the horizontal area of the grid square and A_{lead} to the horizontal area within the square covered by open water or leads. Since A is simply the percentage of leads, we have

$$A_{lead} = A_{sq} \times A \ . \tag{51}$$

4.6.3 Temperature and Lead Area Changes For Positive Q_o

In the event of a positive flux, $A_{lead} \times Q_o$ is the total energy available to warm the water and laterally melt the ice. Of this amount, $A \times A_{lead} \times Q_o$ is allotted for warming and the remaining $(1-A) \times A_{lead} \times Q_o$ is allotted for lateral melt. Although this is a crude parameterization, it does conform with the intuitive feeling that the larger the lead area, the greater will be the energy used directly in the lead rather than in melting the ice along the lead. Also, should there be no ice then this parameterization does correctly use all the energy for warming the water. The only other parameterization known to the author is one of Semtner, where all the energy is allotted to lateral melt regardless of the lead percentage (Washington *et al.*, 1976). The Semtner parameterization is unrealistic when A approaches 100%.

In the current model, the positive flux $A_{lead} \times Q_o$ is distributed as follows:

(a) $A \times A_{lead} \times Q_o$ warms the water in the lead. As the energy available per unit horizontal area is $A \times Q_o$, the temperature increase becomes:

$$\Delta T_w = \frac{A \times Q_o}{d_{mix} \times c_w} \quad . \tag{52}$$

(b) $(1-A) \times A_{lead} \times Q_o$ melts the ice laterally. Since the energy per unit horizontal area required for melting is $Q_I \times h_I + Q_S \times h_s$, the increase in horizontal lead area becomes:

$$\Delta A_{lead} = \frac{(1-A) \times A_{lead} \times Q_o}{Q_I \times h_I + Q_S \times h_s} \quad . \tag{53}$$

(c) If the resulting A_{lead} from (b) exceeds A_{sq} (i.e., $A > 100\%$), then all ice has melted and the energy which could have melted the additional ice instead further heats the water. In this case, A is subsequently set at precisely 100%.

Water temperature adjustments follow from both (b) and (c). The melted ice of (b) (Figure 20) yields a volume-weighted water temperature in the newly-formed lead area of:

$$T = \frac{T_w, (d_{mix} - .88\ h_I) + 271.2\ K \times .88 \times h_I}{d_{mix}} \quad . \tag{54}$$

The newly-formed lead immediately mixes with the old lead, yielding a lead temperature of:

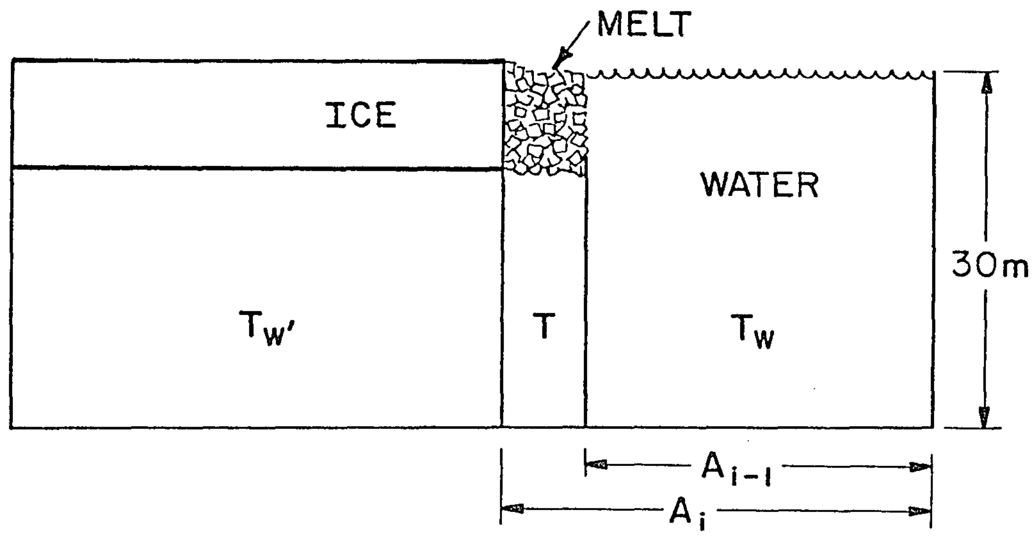

Figure 20. Variables involved in calculating temperature changes due to lateral melt.

$$T_{w,i} = \frac{T_{w,i-1} \times A_{i-1} + T\,(A_i - A_{i-1})}{A_i} \,. \tag{55}$$

In calculation (c), the new open water temperature T_w from equation (55) (calculated with A_i = 100%) must be further modified by the additional heat input from energy remaining following the total ice melt. The amount of this excess energy is the product of $(Q_I \times h_I + Q_S \times h_s)$ and the difference between the calculated lead area and the area of the grid square. Setting A' equal to the ratio of the calculated lead area to the grid square area, we have the adjusted water temperature:

$$T_{w,i} = T_{w,i-1} + \frac{(A' - 100\%) \times (Q_I \times h_I + Q_S \times h_s)}{d_{mix} \times c_w} . \qquad (56)$$

4.6.4 Temperature and Lead Area Changes For Negative Q_o

If Q_o is negative, water must be cooled to offset the energy deficit, the necessary cooling being:

$$\Delta T_w = \frac{Q_o}{d_{mix} \times c_w} . \qquad (57)$$

This creates difficulties only if the calculated water temperature lies below the freezing point, 271.2 K, in which case the temperature is reduced only to freezing and the remaining energy deficit is balanced by the freezing of water at the lead surface. In order to maintain only one ice thickness in an individual grid square, the ice accretion is done laterally onto the existing ice. Letting T_w^* equal the below-freezing, calculated water temperature, the remaining energy deficit after cooling the lead to freezing equals $c_w \times d_{mix} \times A_{lead} \times (271.2\ \text{K} - T_w^*)$. Thus, maintaining a uniform h_I throughout the ice-covered portion of the grid square, the change in lead area becomes:

$$\Delta A_{lead} = - \frac{c_w \times d_{mix} \times A_{lead} \times (271.2\ \text{K} - T_w^*)}{Q_I \times h_I} . \qquad (58)$$

This decrease in lead area requires an adjustment in the temperature under the ice. Again weighting by volume:

$$T_{w',i} = \frac{T_{w',i-1} \times (1 - A_{i-1}) + T_w \times (A_{i-1} - A_i)}{1 - A_i} \quad . \tag{59}$$

The one possible problem with the newly calculated percent leads is a resulting A which is too low. Clearly $A < 0$ is physically impossible, but the model further restricts A by setting a minimum allowable value A_{min} for the lead percentage. A_{min} equals 2% in the Antarctic and 0.5% in the Arctic, the reasoning being that in the Antarctic divergent processes tend to keep a minimum of 2% of any 200 km × 200 km area free of ice, while in the Arctic the divergent processes are considerably weaker.

If A falls below A_{min}, A is reduced exactly to A_{min}, A_{min} replaces A_i in equation (59), and the remaining energy deficit is offset by a cooling of the water under the ice. Setting A* equal to the too-low, calculated lead percentage, the remaining deficit becomes $Q_I \times h_I \times (A_{min} - A^*) \times A_{sq}$. To balance this, the temperature is reduced by:

$$\Delta T_{w'} = - \frac{Q_I \times h_I \times (A_{min} - A^*)}{d_{mix} \times c_w \times (1 - A_{min})} \quad . \tag{60}$$

Finally, should the calculated temperature $T_{w'}$ be below freezing, then ice is accreted to the bottom of the existing ice, after which $T_{w'}$ is set exactly at 271.2 K. The amount of accretion is calculated to release precisely the heat needed to raise the water temperature to 271.2 K:

$$h_{I,i} = h_{I,i-1} + \frac{(271.2\text{ K} - T_{w'}) \times d_{mix} \times c_w}{Q_I} . \qquad (61)$$

An instructive case regarding equations (60) and (61) occurs when the temperature under the ice is initially at the freezing point. In that event, since the water cannot be further cooled, the total effect of a calculated lead percentage below A_{min} is the freezing of ice to the underside of the existing ice. Equation (60) yields

$$T_{w'} = 271.2\text{ K} - \frac{Q_I \times h_I \times (A_{min} - A^*)}{d_{mix} \times c_w \times (1 - A_{min})} \qquad (62)$$

so that, by equation (61), the new ice thickness is

$$h_{I,i} = h_{I,i-1} + \frac{h_{I,i-1}(A_{min} - A^*)}{(1 - A_{min})} . \qquad (63)$$

Since the accretion occurs over the grid fraction $1 - A_{min}$, the volume accreted is $h_{I,i-1}(A_{min} - A^*)A_{sq}$. Appropriately, this is the same volume as in the lateral freezing of ice of thickness $h_{I,i-1}$ over grid fraction $A_{min}-A^*$, i.e., the amount of excess lateral freezing originally calculated in equation (58).

To summarize the calculations for this section, if the net vertical energy input into the lead is negative, the energy deficit is made up in the following order:

(1) cool the temperature in the lead (but not below 271.2 K)

(2) freeze ice laterally onto the existing ice (but do not reduce the lead area below A_{min})

(3) cool the water under the ice (but not below 271.2 K)

(4) freeze water to the underside of the ice.

4.6.5 Lateral Mixing of Water

The above temperature determinations are followed by a simple adjustment to account for lateral mixing:

$$\Delta T_{w'} = \frac{1}{4} A \; (T_w - T_{w'})$$

$$\Delta T_w = \frac{1}{4} (1 - A) \; (1 - \frac{.88h_I}{d_{mix}}) \; (T_{w'} - T_w) \; . \tag{64}$$

In this manner temperature contrasts are reduced but the total heat content of the water remains the same, the total increase/decrease of heat energy under the ice -- $c_w \times (1 - A) \times A_{sq} \times (d_{mix} - .88h_I) \times \Delta T_{w'}$ -- balancing the heat decrease/increase in the leads -- $c_w \times A \times A_{sq} \times d_{mix} \times \Delta T_w$.

4.7 Transport Calculations

The transport calculations proceed in two steps. Initially, a steady-state velocity of the ice is calculated by balancing four major stresses: wind stress from above the ice $\vec{\tau}_a$, water stress from below the ice $\vec{\tau}_w$, Coriolis force $\vec{D}$, and the stress from the tilt of the sea surface or dynamic topography $\vec{G}$. We follow this by incorporating a fifth stress, the internal ice resistance produced by the interactions among the ice floes, while computationally attempting to move the ice according to the velocity vectors resulting from the four-stress steady state. The actual movement and the ice resistance force will be discussed after the first four stresses and their balance have been presented.

4.7.1 Ice Velocities

From Newton's second law of motion, the momentum equation, ice velocities $\vec{V}_i$ should be calculable from

$$\frac{d\vec{V}_i}{dt} = \sum_j \vec{F}_j \tag{65}$$

where the $\vec{F}_j$ are all the forces (per unit mass) acting on the ice pieces. As stated above, we here assume a steady-state velocity, hence setting the left side of (65) to 0, and restrict our $\vec{F}_j$ to four major stresses, reducing equation (65) to

$$0 = \vec{\tau}_a + \vec{\tau}_w + \vec{D} + \vec{G} \ . \tag{66}$$

Arguments for a steady-state *versus* a nonsteady-state calculation have been given by both Campbell (1964) and Rothrock (1973). Arguing from the point of view of scale analysis, Rothrock shows that the acceleration term is generally three orders of magnitude smaller than the wind and water stresses.

Of the stresses considered, only the Coriolis force has a precise formulation:

$$\vec{D} = \rho_i h_I f \ \vec{V}_i \times \vec{k} \tag{67}$$

(Campbell, 1964). All terms have been previously defined (sections 4.6.1, 4.5.3, 4.2.1, 4.7.1) except $\vec{k}$, the unit vertical vector.

The stress from the dynamic topography involves a finite-difference approximation to the gradient of sea-surface height. With the use of the dynamic topography fields, DT(I,J), plotted in Figures 11 and 13, the stress formulation becomes:

$$\vec{G} = \frac{-10\rho_i h_I\{[DT(I+1,J)-DT(I-1,J)]\vec{i} + [DT(I,J+1)-DT(I,J-1)]\vec{j}\}}{2 \times H} \tag{68}$$

(Campbell, 1964: $\vec{G} = \rho_i h_I \nabla_H (\Delta D)_s$). The horizontal distance H between grid points is approximated at a constant 2×10^5 m.

The remaining two stresses are less precise. Wind stress is assumed to act in the direction of the wind, which, following Pritchard *et al.* (1976) is approximated as 20^o to the left of the surface geostrophic wind in the northern hemisphere and 20^o to the right in the southern hemisphere. With β as the resulting angle in the $x - y$ plane, wind stress is parameterized as:

$$\vec{\tau}_a = \alpha\, C_D\, \rho_a\, V_{wg}^{\;2}\, (\cos\beta\, \vec{i} + \sin\beta\, \vec{j}) \qquad (69)$$

(Hunkins, 1966: $\tau_a = \rho_a C_D V_w^{\;2}$). Equivalently, the formulation is

$$\vec{\tau}_a = \alpha\, C_D\, \rho_a V_{wg} \vec{V}_{wg} B\ , \qquad (70)$$

where B is the following rotation matrix:

$$B = \begin{cases} \begin{pmatrix} \cos 20^{\circ} & \sin 20^{\circ} \\ -\sin 20^{\circ} & \cos 20^{\circ} \end{pmatrix} & \text{in the northern hemisphere} \\ \begin{pmatrix} \cos 20^{\circ} & -\sin 20^{\circ} \\ \sin 20^{\circ} & \cos 20^{\circ} \end{pmatrix} & \text{in the southern hemisphere} \end{cases} \qquad (71)$$

This latter formulation avoids the use of β. The drag coefficient C_D is set at 0.0024, a figure reflecting the roughening effect of ridging (Banke and Smith, 1975), and $\alpha = 3$ is an adjustment factor to account for the use of monthly mean winds rather than instantaneous values (Semtner, 1976b).

Following Hunkins (1966), water stress has been parameterized as

$$\vec{\tau}_w = \rho_w \sqrt{k_w\, |f|}\, (U_R \vec{i} + V_R \vec{j})\ , \qquad (72)$$

with both the eddy viscosity $k_w = 24 \times 10^{-4}\ m^2\ s^{-1}$ and the density of sea water ρ_w (section 4.6.1) taken as constants.

The vector $U_R\vec{i} + V_R\vec{j}$ is the vector difference between the ocean geostrophic velocity $\vec{V}_{og}$ and the ice velocity $\vec{V}_i$, i.e.,

$$U_R\vec{i} + V_R\vec{j} = (u_{og} - u_i)\vec{i} + (v_{og} - v_i)\vec{j} \; . \tag{73}$$

The ocean geostrophic flow is obtained by balancing the dynamic topography and the Coriolis forces ($\vec{D} + \vec{G} = 0$), while the ice velocity is the unknown to be calculated by balancing the four stresses. The geostrophic balance yields an ocean geostrophic velocity

$$\vec{V}_{og} = \frac{-10\{[DT(I,J+1)-DT(I,J-1)]\vec{i} - [DT(I+1,J)-DT(I-1,J)]\vec{j}\}}{2 \times f \times H} \; . \tag{74}$$

Having defined the four stresses, we obtain the ice velocity from equation (66) by solving the two component equations:

$$0 = \rho_i h_I f v_i - 10\rho_i h_I \left(\frac{1}{2 \times H}\right) [DT(I+1,J) - DT(I-1,J)]$$
$$+ \alpha\, C_D \rho_a V_{wg}{}^2 \cos\beta + \rho_w \sqrt{k_w\, |f|}\; U_R \quad , \tag{75}$$

$$0 = -\rho_i h_I f u_i - 10\rho_i h_I \left(\frac{1}{2 \times H}\right) [DT(I,J+1) - DT(I,J-1)]$$
$$+ \alpha\, C_D \rho_a V_{wg}{}^2 \sin\beta + \rho_w \sqrt{k_w\, |f|}\; V_R \; .$$

To solve these, u_i and v_i are replaced by their equivalents $u_{og} - U_R$ and $v_{og} - V_R$ and equation (74) is inserted. This simplifies the pair of balance equations to:

$$0 = -\rho_i h_I f V_R + \alpha\, C_D \rho_a V_{wg}^{\ 2} \cos\beta + \rho_w \sqrt{k_w\ |f|}\ U_R$$

(76)

$$0 = \rho_i h_I f U_R + \alpha\, C_D \rho_a V_{wg}^{\ 2} \sin\beta + \rho_w \sqrt{k_w\ |f|}\ V_R$$

which are easily solvable as a pair of simultaneous linear equations in U_R and V_R. The result is:

$$U_R = \frac{-\rho_w \sqrt{k_w\ |f|}\ \cos\beta - \rho_i h_I f \sin\beta}{\rho_w^{\ 2} k_w |f| + \rho_i^{\ 2} h_I^{\ 2} f^2} \ (\alpha C_D \rho_a V_{wg}^{\ 2})$$

(77)

$$V_R = \frac{-\rho_w \sqrt{k_w\ |f|} \sin\beta + \rho_i h_I f \cos\beta}{\rho_w^{\ 2} k_w |f| + \rho_i^{\ 2} h_I^{\ 2} f^2} \ (\alpha C_D \rho_a V_{wg}^{\ 2})$$

from which the velocity of the ice $\vec{V}_i = \vec{V}_{og} - \vec{V}_R$ is immediately calculated.

4.7.2 Ice Movement

Once the ice velocities at each grid square have been found, the ice within each square is translated without rotation or distortion to the end point of its velocity vector, i.e., the midpoint of the ice is translated from (I,J) to $(I + \frac{\Delta t \times u_i}{H}, J + \frac{\Delta t \times v_i}{H})$. It is at this point that attention must be given to the effect of continental boundaries and to the resistance forces among the ice floes. The modeled ice responds to continental boundaries by disallowing on-shore motions; should either u_i or v_i component lead directly into a land grid point then that component is set to 0. Thus the boundaries have the same effect as in Nikiforov *et al.* (1970), velocity components normal to and approaching the coast being zeroed out, with velocity components tangential to the coast remaining unchanged.

Internal ice resistance produces an effect similar to, though not as stringent as, that of continental boundaries. After the redistribution of ice according to the velocities calculated from the 4-stress balance, all incoming velocities to any grid square with a resulting ice concentration $C_{\%}$ greater than 100% - A_{min} are reduced. The reduction is done proportionately, after first insisting that the ice attempting to remain in the grid square remains. More specifically, if the remaining ice covers a percentage $R_{\%}$ of the grid square, then the initial velocity components v contributing to excessive convergence in this square are reduced to

$$\frac{100\% - A_{min} - R_{\%}}{C_{\%} - R_{\%}} v \quad .$$

Since the ice remaining in a square increases with a reduction in its velocity, this method generally requires several iterations. The iterative procedure continues until no grid square has an ice concentration exceeding 100% - A_{min}.

CHAPTER V

STANDARD CASE RESULTS AND COMPARISONS WITH OBSERVATIONS

This chapter describes the model results for the so-called "standard case", the case employing all parameterizations, prescribed forcing, and numerical values presented in Chapter IV. Later, in Chapter VII, indications are given of the changes in results due to individual parameter changes.

As each run requires initialization of all variables calculated by determination of their incremental increase or decrease, Table 5 lists the starting values used for the standard case. Computations begin with a presumed time of 8:00 G.M.T., January 1, year 1 and run through four years of simulation in the Antarctic and five in the Arctic. This is sufficient time in each hemisphere for the results to approach an equilibrium yearly cycle (see section 5.4).

The resultant annual cycles obtained in the standard case are presented in Figures 21-24. The simulated Arctic ice varies in extent from a minimum in September to a maximum in March, though the February and April extents are very close to those of March. In September the ice covers only a portion of the Arctic and has receded from most coastlines. Thickness reaches 3.0 m in the center of the pack. At the March maximum, extent has greatly increased, reaching Iceland

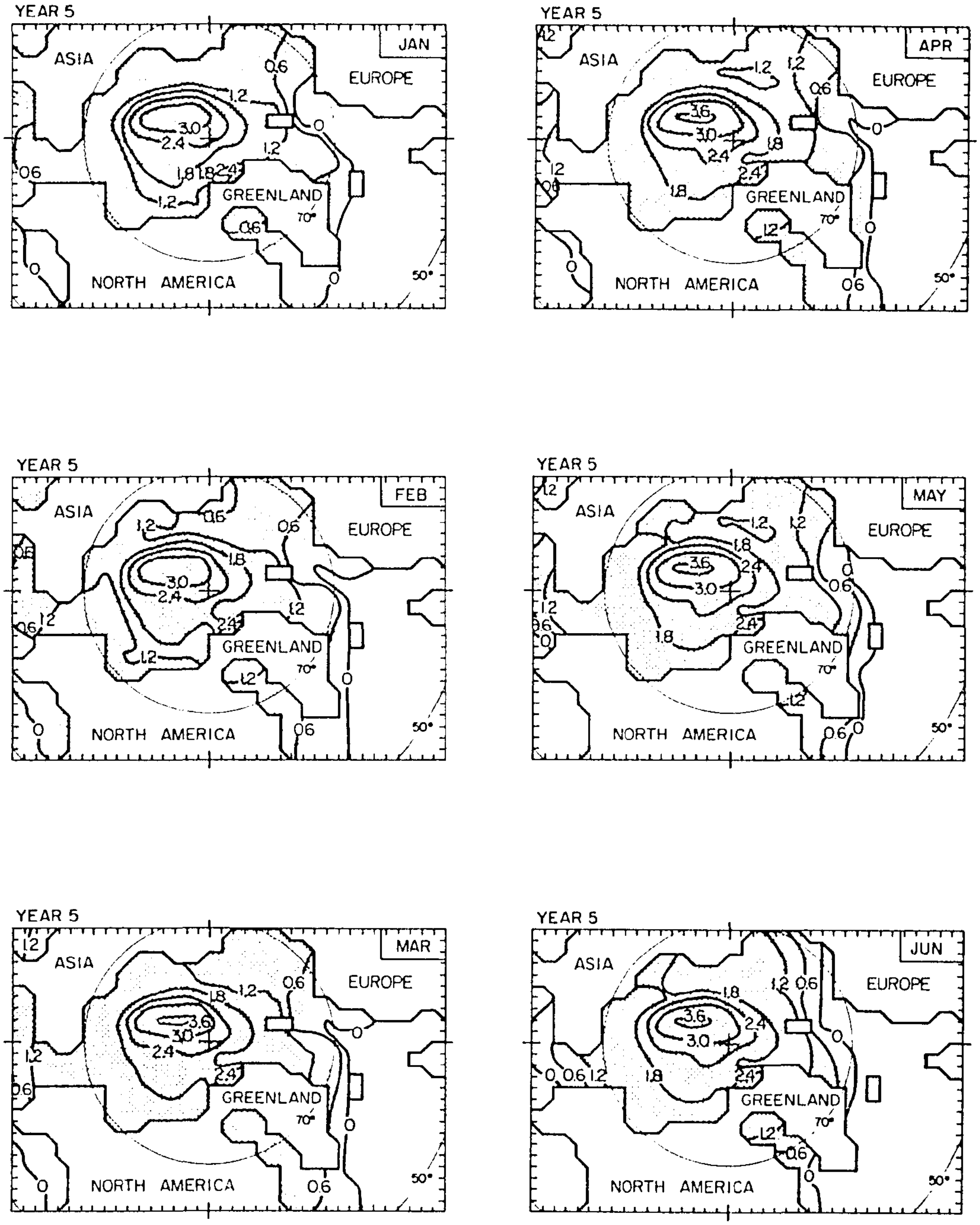

Figure 21. Simulated half-yearly cycle of sea ice in the Arctic, January–June. Contours show ice thickness in meters, while shading indicates ice compactness above 90%.

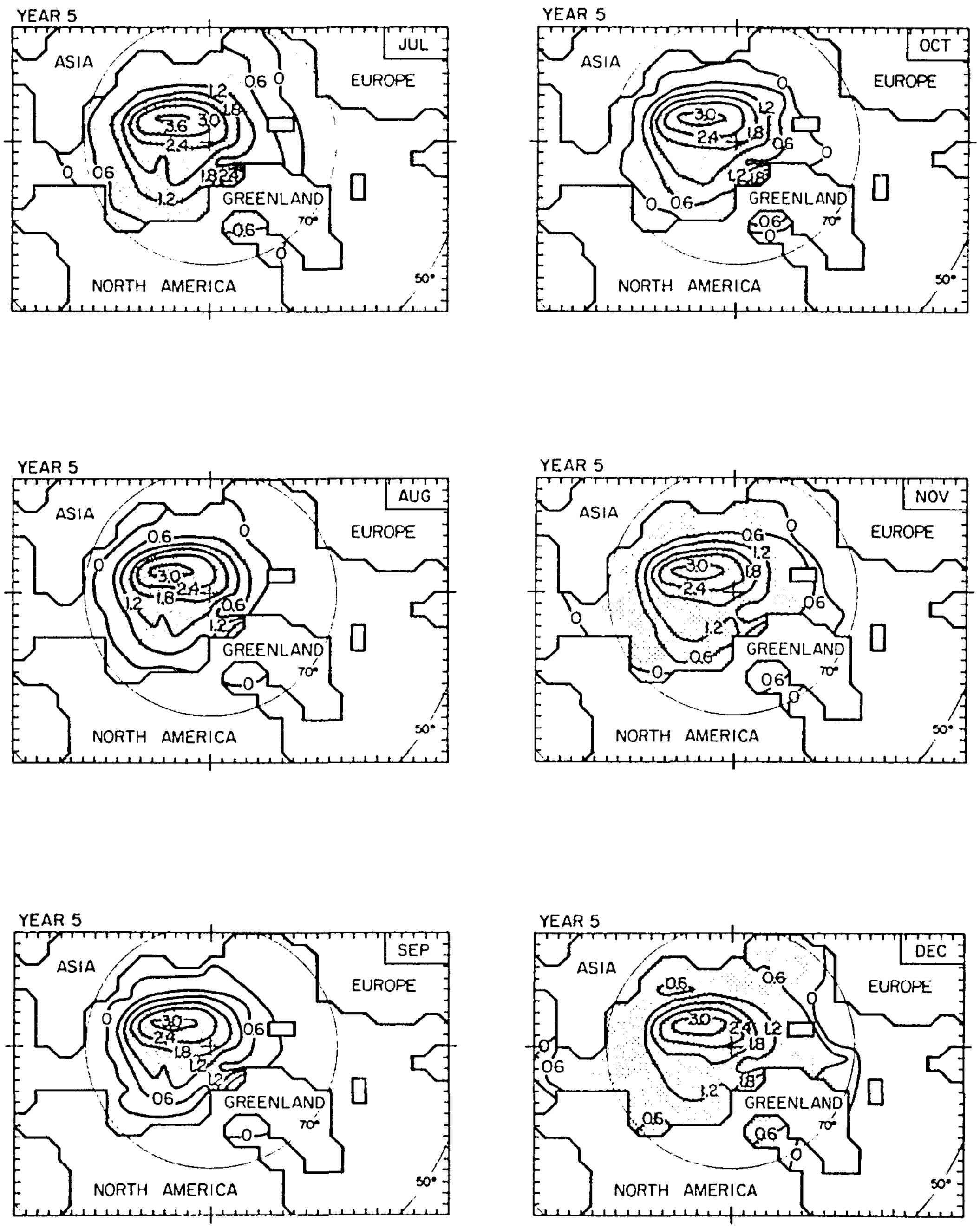

Figure 22. Simulated half-yearly cycle of sea ice in the Arctic, July-December. Contours shows ice thickness in meters, while shading indicates ice compactness above 90%.

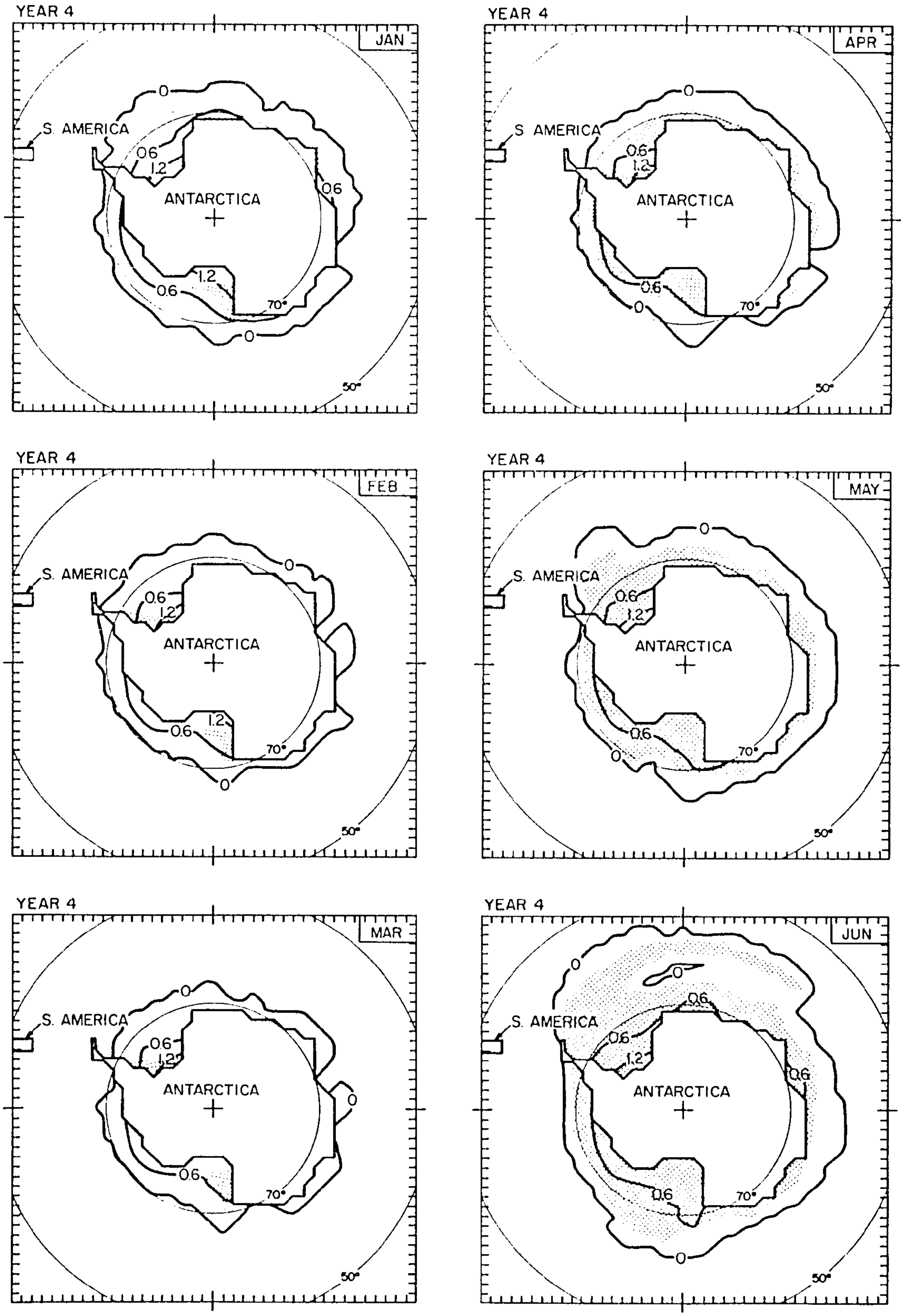

Figure 23. Simulated half-yearly cycle of sea ice in the Antarctic, January-June. Contours show ice thickness in meters, while shading indicates ice compactness above 90%.

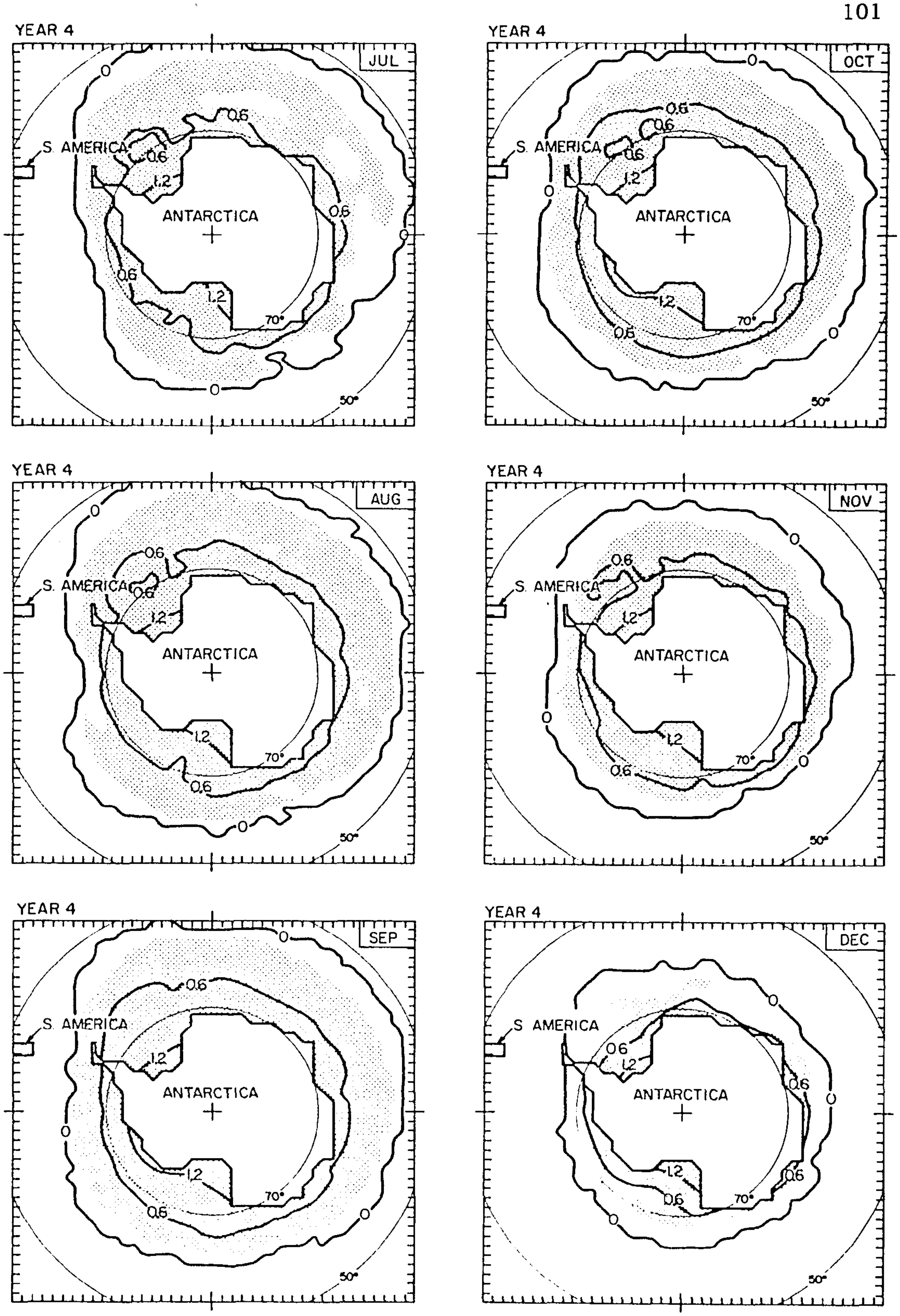

Figure 24. Simulated half-yearly cycle of sea ice in the Antarctic, July-December. Contours show ice thickness in meters, while shading indicates ice compactness above 90%.

TABLE 5. Variable initialization in the standard case.

	Arctic	Antarctic
Ice thickness	3.5 m	1.5 m
Snow thickness	0.3 m	0.0 m
Percent area with open water	10%	10%
Temperature of open water	271.45 K	271.45 K
Temperature of water under ice	271.45 K	271.45 K
Temperature of upper snow surface	271.20 K	271.20 K
Temperature of snow-ice interface	271.20 K	271.20 K

and beyond the southern coast of Greenland, while the central Arctic thicknesses have reached 3.6 m.

In the simulated Antarctic, minimum ice extent occurs in March and maximum extent in late August. In March the ice reaches a latitude of $64^{\circ}S$ off the coast of East Antarctica, with the maximum extension from the continent being in the Weddell Sea region to the east of the Antarctic Peninsula. Thickness varies from about 1.2 m in the Ross and Weddell Seas to 0 m at the ice edge. In August the ice extends to the grid boundary over the approximate longitude range $20^{\circ}W-10^{\circ}E$, reaching latitudes of $50-51^{\circ}S$. Thickness varies from about 1.4 m at its coastal maximum to 0 m at the ice edge.

In the following sections, the general pattern of Arctic and Antarctic results sketched above is examined more closely by comparison with atlas and satellite observations. The comparisons are divided into three sections--ice extent and distribution, ice thickness and lead areas, and ice drift--with the fullest discussion being given for the extent and distribution, these being the aspects for which the existing information is most complete. The concluding section of the chapter then deals with the development of the model results on a year-to-year basis.

5.1 Ice Extent and Distribution

Although an approximate picture of the winter and summer ice extents in each hemisphere is included at the start of Chapter II (Figures 3 and 4), the actual ice distributions vary considerably from one year to another, thus eliminating the possibility of a perfect yearly cycle against which to compare simulated results. This section begins therefore with an indication of the observed variability.

Pease (1975) summarizes significant differences in Antarctic ice extent as depicted by three standard atlases: (1) the Soviet *Atlas of Antarctica* (Tolstikov, 1966), (2) the U. S. Navy *Oceanographic Atlas of the Polar Seas* (Daniel, 1957), and (3) the British Admiralty's *Ice Chart of the Southern Hemisphere* (1943). The U. S. atlas shows a larger extent of ice than the Soviet atlas for eastern longitudes and a smaller extent for western longitudes, this being true in every month. The British charts suggest more ice in summer than either the Soviet or U. S. sources, while, furthermore, Gloersen and Salomonson (1975) find a much more irregular distribution for the specific summer of 1972-1973 than is presented by any of the three atlases. The Gloersen and Salomonson work plots extents from satellite microwave radiometry.

Prior to the arrival of satellite sensing, apparent differences between sources on the Antarctic ice boundary were often attributed to the sparsity and imprecision of observations rather than to real year-to-year contrasts. Though we remain plagued by sparse observations, satellite images have shown decisively the existence of large interannual differences, some of which will now be mentioned. (The Appendix briefly discusses satellite capabilities and restrictions.)

Figure 25 presents the satellite-observed October and December extents of Antarctic sea ice for the years 1967 and 1968. The maps, taken from Budd (1975), were drawn from 30-day mean minimum brightness composites. In spite of the consecutiveness of the two years, clear contrasts exist in the pattern of ice distribution. In October 1968 the ice extent is more symmetric than in 1967 and reaches to lower latitudes at almost all longitudes except those in the region north of the Weddell Sea. The ice is almost nonexistent on the east coast of the continent in December of 1967 and yet

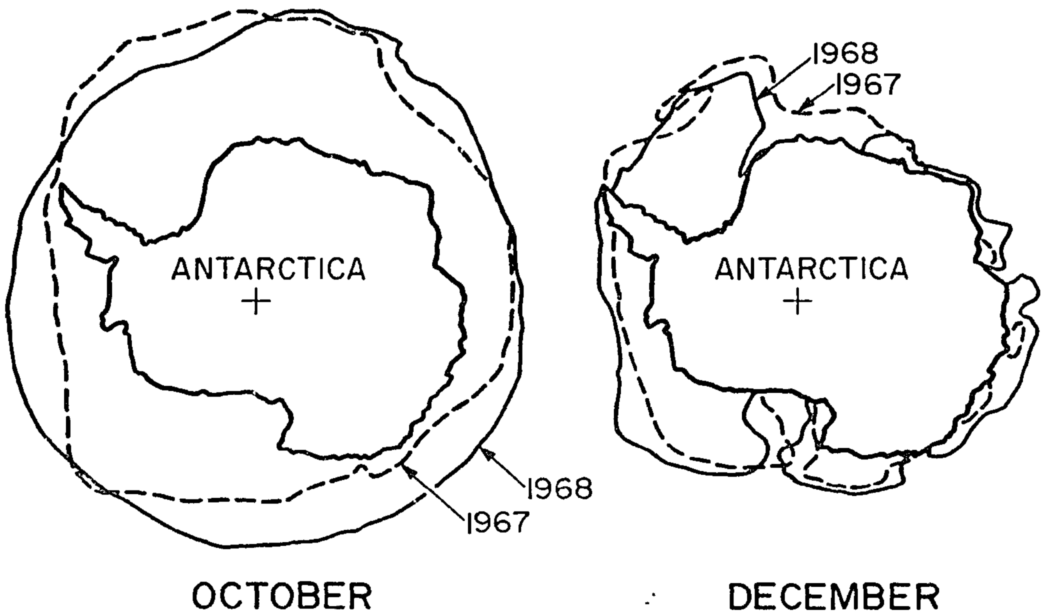

Figure 25. Satellite-observed Antarctic sea ice extents for the months October and December of 1967 and 1968. Abbreviated and redrawn from Budd (1975, p. 421).

extends further than the 1968 ice in the region of the 0^{o} meridian. Ackley and Keliher (1976) have also compared Antarctic ice extents at similar times in two consecutive years, finding the August 1-2 extent greater in 1973 than in 1974 in the Weddell Sea sector but less in the Ross Sea sector. Their data derive from ESMR (Electronically Scanning Microwave Radiometer) observations of the Nimbus V satellite.

Fletcher (1969) has conjectured that typical year-to-year variations in Antarctic ice extent may in fact be as large as typical variations between seasons. Others emphasize changing distributions from one year to another rather than changes in overall extent (e.g., Budd, 1975). As Budd mentions, large anomalies in individual regions may persist over entire seasons.

Interannual variation exists in the Arctic as well, though perhaps not to as striking an extent. As suggestions of the observed variability, Figure 26 presents the location of the September ice edge off northern Alaska for the four years 1953, 1954, 1955, and 1968, and Figure 27 presents ice borders around Spitsbergen in August for the five years 1957, 1958, 1960, 1961, and 1962. Similar variability is found in the entire Atlantic sector of the Arctic ice, as illustrated by a map of Haupt and Kant (1976) of the satellite-observed April extents from 1966 to 1973. Of the eight years presented by Haupt and Kant, the ice margins in April reached the north coast of Iceland in only two years, 1968 and 1969, while they never reached the coast of Norway and always reached the southern tip of Greenland.

Although icebergs are not modeled in the current study, year-to-year variation is also reflected in various iceberg statistics, such as the number of bergs reaching particular latitudes of the North Atlantic. As an example, the recorded number south of 48°N in 1912 (the year the *Titanic* sank) was 1010, in 1929 was 1351, but in 1924, a year intermediate between 1912 and 1929, it was only 11 (Neumann and Pierson, 1966).

This lack of constancy from one year to another obviously eliminates the possibility of an absolute standard against

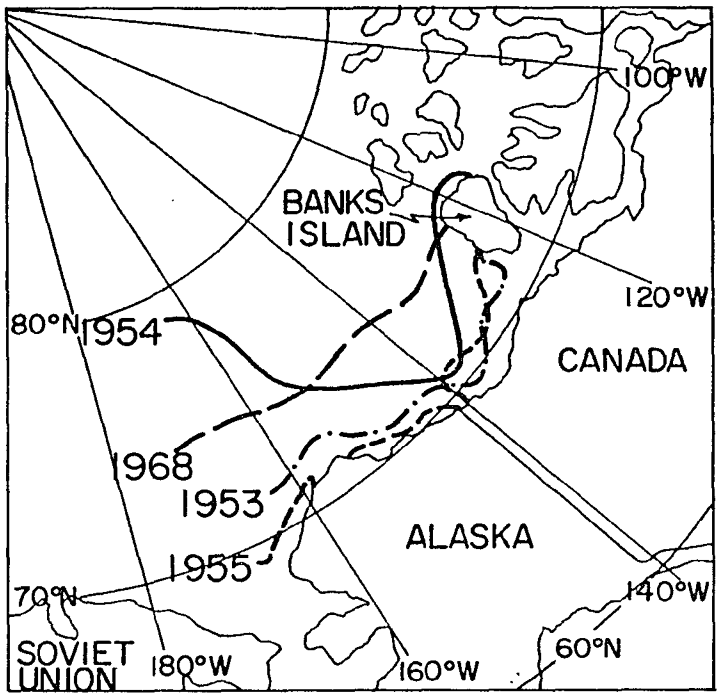

Figure 26. Arctic ice boundaries off northern Alaska, September 1-5, for four separate years. The 1953, 1954, and 1955 edges are from Winchester and Bates (1958, p. 332); the 1968 edge is from J. Walsh (personal communication, 1976).

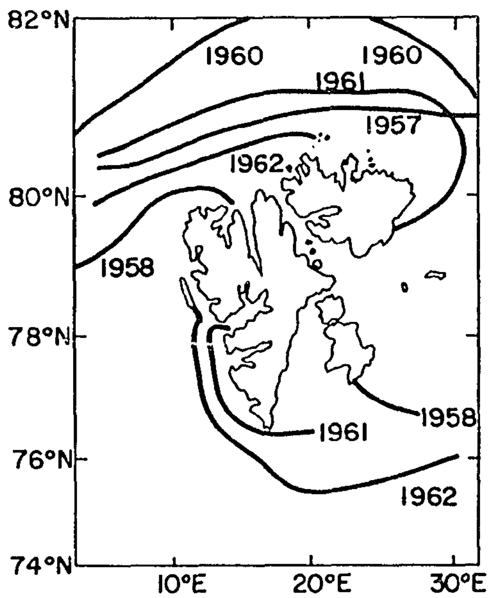

Figure 27. Ice borders around Spitsbergen in August for the five years 1957, 1958, 1960, 1961, and 1962. Abbreviated and redrawn from Blindheim and Ljoen (1972, p. 40).

which to judge numerical results. However, a general comparison can be made between model results and various estimates of actual ice extents, and when this is done the overall correspondence is found to be good.

More specifically, the simulated September and March maps in Figures 21 and 22 place the ice edge at curves which are quite similar to those of Wittmann and Schule (1966) for the mean minimum and maximum ice extents. The major differences in September are that in the Wittmann and Schule case the ice extends further along the east coast of Greenland and does not exist in the Baffin Bay region. The major differences in March are that Wittmann and Schule show a lesser extent in the Atlantic sector by an average of about two degrees of latitude and do not show ice off the coast of southern Alaska.

Off northern Alaska the September ice edge in Figure 22 is well within the range presented by the four years mapped in Figure 26, coming closest probably to 1968 though actually suggesting a greater extent than that year and a lesser extent than either 1953 or 1955. The April ice edge in the Atlantic (Figure 21) corresponds well with the Haupt and Kant (1976) curves for April extents from 1966 to 1973, though it indicates a slightly more southward extent especially off the southwest coast of Greenland. Also, the simulated results have the edge extending to Iceland, which, from the Haupt and Kant maps, would be expected only 25% of the time. By contrast, in September the simulated ice has melted much more off the east coast of Greenland than Rothrock (1973) or Wittmann and Schule (1966) would suggest. The correspondence between the simulated ice extent and the Rothrock curve is close for the rest of the Arctic though with ice touching more of the coast of Siberia in the Rothrock case. For almost every area of the Arctic a reference could be found suggesting a greater extent than the simulation and an alternate reference could be found suggesting a lesser extent.

In summary, the simulated Arctic distribution and extent seem within the observed variability for most sections of the Arctic. The two areas of poor correspondence are to the south of Alaska, where too much ice is simulated, and immediately along the Greenland coast. The results show an abbreviated ice extension down the east coast of Greenland but too much ice off the southwest coast. These are both regions where the oceans are probably exerting a far greater influence in the real world than is allowed in the model. To the east of Greenland the predominant surface flow is from north to south, carrying cold Arctic water and ice southward along the coast, while to the southwest of Greenland warm water flows from the Atlantic, moving northward along the coast in the West Greenland Current.

As with the Arctic, the large-scale Antarctic results also fall within the observed range. In each month the extents of Figures 23-24 correspond within about two degrees of latitude to those of the U. S. Navy *Oceanographic Atlas of the Polar*

Seas (Daniel, 1957). The simulated extents tend to be somewhat less than the atlas extents from February to April, especially in the Antarctic Peninsula-Weddell Sea region, and somewhat greater from July to December. In May the simulation shows more ice off East Antarctica and less ice along the Peninsula than the *Oceanographic Atlas*. The February and October maps from this source are shown in Chapter II (Figure 4).

The simulated ice limits differ from those of the Soviet *Atlas of Antarctica* (Tolstikov, 1966) most strongly off East Antarctica in the longitude range 40^{o}E-140^{o}E. Within this region the atlas extents tend to be less than the simulated extents, with the strongest differences occurring in August and September, when the simulated ice reaches roughly 6^{o} further northward than the atlas charts. By contrast, in November the atlas and simulated extents are roughly identical in the eastern longitudes.

Finally, compared to the satellite-observed results of Figure 25, the simulated December extent is noticeably greater at most eastern-hemisphere longitudes than the observed in either 1967 or 1968, while the simulated October results seem quite realistic. It should be noted that the October 1968 observed distribution--along with the simulated October distribution--does not show the bulge north of the Weddell Sea given by Neumann and Pierson and the Navy *Oceanographic Atlas* (Figure 4).

One additional comment should be made concerning ice extents. Authors presenting curves for supposed "observed" ice extents must make subjective decisions on the placement of the ice edge, as there is no sharp boundary in the real world. Since the decision is almost never at the furthest equatorward occurrence of ice, this could partially account for the model's simulation of a somewhat greater Antarctic ice extent than is indicated by many sources. As an example, Ackley and Keliher (1976) place the edge at the satellite-recorded 150 K brightness temperature contour, which corresponds roughly to an ice concentration of 14%. The maps of the U. S. Fleet Weather Facility place the edge at about 12% concentration (Ackley and Keliher, 1976).

As for the times of minimum and maximum Antarctic ice extent, the simulated minimum in March appears to be timed properly in terms of the typical real-world cycle, while the maximum in late August appears tc be slightly early. Fletcher (1969), Pease (1975), and Tolstikov (1966) all indicate March as the month of minimum extent and both Pease and Tolstikov indicate September as the month of maximum extent. Fletcher suggests the maximum may occur in either September or October. On the other hand, the ESMR satellite data examined by Ackley and Keliher (1976) place the 1974 maximum extent near the end of August, the same as the simulated results. The fact that the ESMR data for 1973 have the maximum extent at the end of September (Ackley and Keliher, 1976) once again illustrates the real-world variability.

5.2 Ice Thickness and Lead Areas

In addition to distribution and extent, ice thicknesses and concentrations are needed for a full picture of the ice coverage in either hemisphere. The simulated results in both these aspects seem reasonable in the large-scale view, though perhaps the Arctic thicknesses decrease too gradually from the thickest values in the central Arctic to the values at the ice edge and perhaps the Antarctic thicknesses are too low, though only by 0-0.5 m.

Referring back to Figures 21-22, central Arctic ice thickness tends to be about 3.0-3.6 m. This exceeds the 2.88 m average thickness simulated by the one-dimensional model of Maykut and Untersteiner (1969) and the 2 m suggested by Wittmann and Schule (1966), but it is exceeded by the 4 m mean thickness stated by Fletcher (1965) and the 4-5 m mean thickness of Lyons (1961, in Maykut and Unterstiner, 1969). The simulated central Arctic ice thicknesses thus appear within the range of other sources. The fact that these central thicknesses do not extend over a large spatial area would indicate that, if anything, the simulated results are underestimating, rather than overestimating, general thicknesses over the entire Arctic Basin. However, Baker (1976) suggests that Arctic sea ice thickness tends to be between 2 m and 3 m, and the data from H. M. S. *Dreadnought* average only 2.7 m in thickness in March, which is clearly a winter month. The *Dreadnought* data are for a linear track between $80^{\circ}N$ and $90^{\circ}N$ (Swithinbank, 1972). Comparing these various values with Figures 21-22, the simulated thicknesses appear realistic.

Spatially, the first-order tendency is for the ice thicknesses to decrease outward from the peak values in the central Arctic (Figures 21-22). The major exception to this is in the region directly north of Greenland and Ellesmere Island, where thicknesses again increase as the coast is approached. Interestingly, this is precisely the region of greatest ridging intensity (Tucker and Westhall, 1973; Weeks, 1976a).

As for the yearly cycle of central ice thicknesses, the simulated values of 3.0 m at the end of summer and 3.6 m at the end of winter are comparable to the seasonal differences suggested by others. Neumann and Pierson (1966) suggest the polar cap averages 2.0-2.5 m toward the end of summer and 3.0-3.5 m toward the end of winter, a somewhat larger range than the simulated results, while Maykut and Untersteiner (1969) obtain in their model a somewhat smaller range than that simulated here, theirs being 2.71-3.14 m.

Simulated Antarctic thicknesses (Figures 23-24) decrease fairly monotonically from coastal values of 0-1.5 m out to 0 m at the ice edge. As estimates of Antarctic sea ice suggest that most of the ice is no greater than 1.0-1.5 m thick (Baker, 1976), the simulated thicknesses are realistic, or at least no more than about 0.5 m too thin. As will be seen in Chapter VII, one method of thickening the simulated ice is to decrease the oceanic heat flux and hence the bottom ablation. Such thickening, however, occurs at the expense of increasing ice ex nt as well. Smaller-scale features of Antarctic ice thickness, such as the observed tendency for thicker ice at the northern reaches of the Weddell Sea than at the Weddell Sea coast, are not reproduced. Proper simulation of such features may require detailed modeling of the ocean circulation.

In addition to the monthly 90%-ice-concentration contours presented in Figures 21-24, Figures 28 and 29 present more detailed contour maps of concentration for the months of maximum and minimum extent. In view of the lack of precise data, the simulated concentrations seem reasonable. Wittmann and Schule (1966) claim that at least 5% of the central Arctic consists of open water during all seasons. The modeled results show less than 5% throughout the central Arctic in winter, corresponding poorly with the Wittmann and Schule estimates; however, Maykut (1976) claims a lead percentage of under 1% in winter in the central Arctic and Weeks (1976a) claims a winter ice concentration of 99%, ranging only from 98% to 100%, and a summer concentration of 92%, ranging from 30% to 100%. Similarly, Koerner claims only 0.6% of the area is ice free in winter, and Swithinbank claims a March total of 5% for all open water and ice of thickness less than 0.3 m, only a small fraction of this 5% being open water (Swithinbank, 1972).

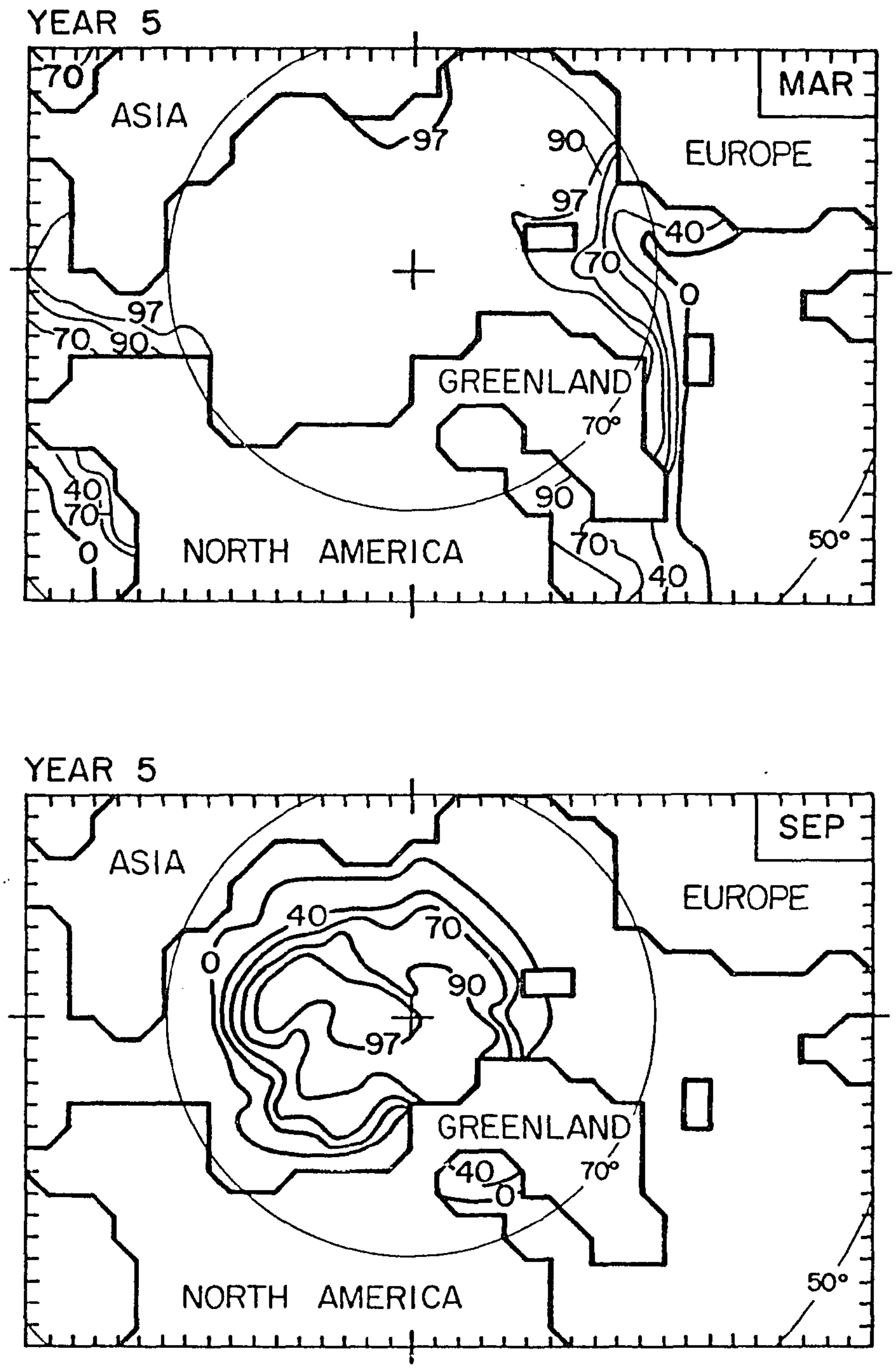

Figure 28. Simulated contours of ice concentration (%) in the Arctic, March and September.

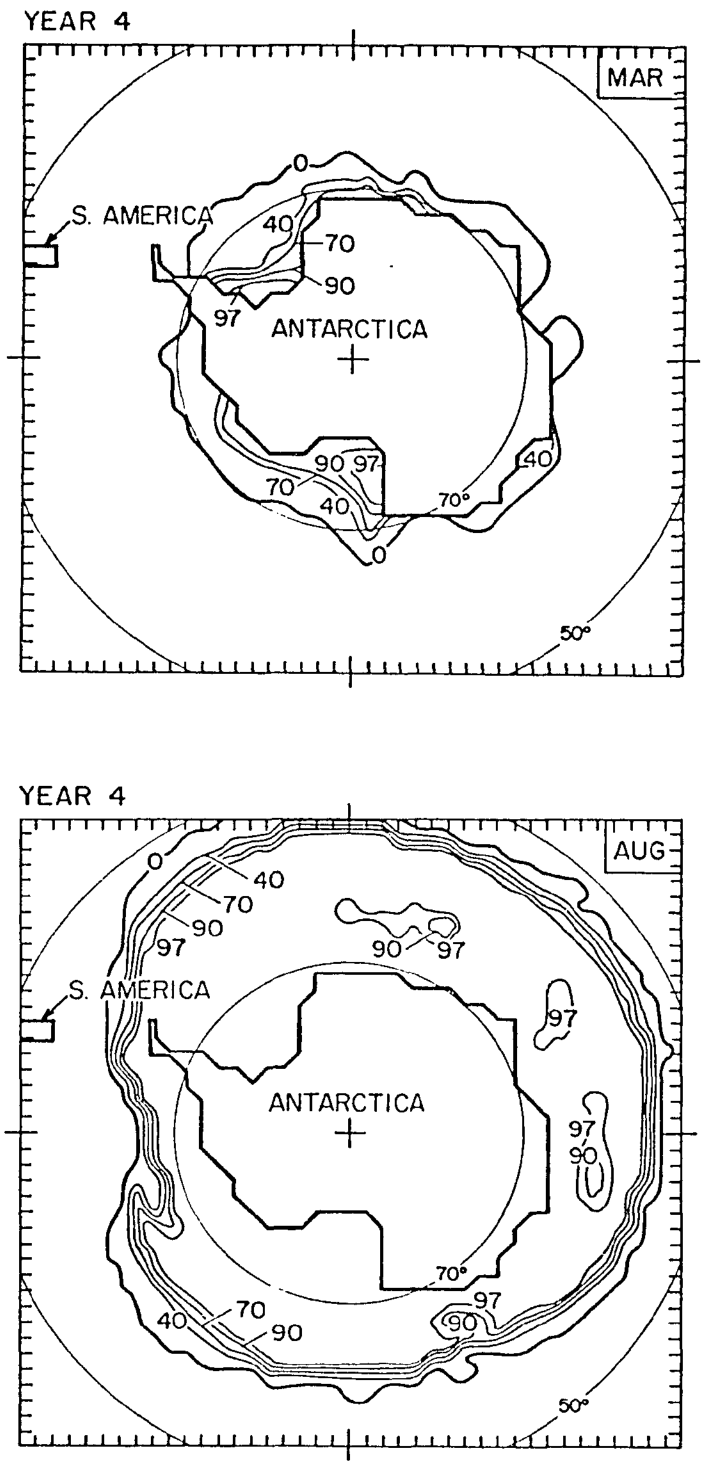

Figure 29. Simulated contours of ice concentration (%) in the Antarctic, March and August.

The ice of Figures 21-22 is less compact than the estimates of Weeks or Koerner, more compact than the estimates of Wittmann and Schule.

In the Antarctic also, the simulated ice concentrations fall within the range suggested by the data. The patterns correspond well with those of Neumann and Pierson (1966) for both February and October (Figure 4), and they reveal a broad region of lowered concentrations in the area most noted for large *polynyas*, to the north of Queen Maud Land at about the Greenwich meridian (Daniel, 1957). On the other hand, Ackley and Keliher (1976) report that satellite data examined for the Antarctic winters of 1973 and 1974 reveal far more open water than most previous estimates, and, incidentally, than the simulated results. The overall ice concentrations of Ackley and Keliher between the continent and the ice edge average 70-80% in the Weddell Sea sector, 65-75% in the Ross Sea sector, 55-65% in the East Antarctic sector, and 50-65% in the Amundsen-Bellingshausen Sea sector. Ackley and Keliher do warn that their estimates are probably smallest-possible concentrations since the method overestimates the lead percentages as both fresh snow and clouds with high water content tend to lower brightness temperatures down toward their sea water values. In a further analysis, Zwally and Gloersen (1977) claim that, on an average, the ice concentrations derived by Ackley and Keliher are probably about 10-15% too low.

5.3 Ice Drift

Simulated January and July ice velocities appear in Figures 30 and 31. These are more difficult to compare against observations than the extents or thicknesses were since considerably less observational data exist, especially in the southern hemisphere. However, major qualitative aspects of the large-scale ice drift in the Arctic are fairly well known, and, of benefit to future studies, procedures are now being developed for estimating drift from LANDSAT satellite photographs (Hibler *et al.*, 1976).

Beginning with the northern hemisphere, schematic plots of the observed patterns of Arctic ice drift almost always emphasize two main features: the anticyclonic Pacific Gyre in the Beaufort Sea and Central Arctic Basin, and the Transpolar Drift Stream crossing the Pole from the Laptev and East Siberian Seas and moving out toward the Atlantic, eventually merging with the East Greenland Drift. Smaller features also often mentioned are a stagnant region north of Greenland and Ellesmere Island and a small cyclonic gyre to the east of Severnaya Zemlya (Rothrock, 1973). These various observed features are schematized in Figure 32.

Both the Pacific Gyre and the Transpolar Drift are visible in the simulated results. The Gyre shows clearly in the July drift chart, with its center occurring at roughly 78°N, 210°E. This location for the gyre center is quite close to the 79°N, 200-205°E positioning determined from data of a

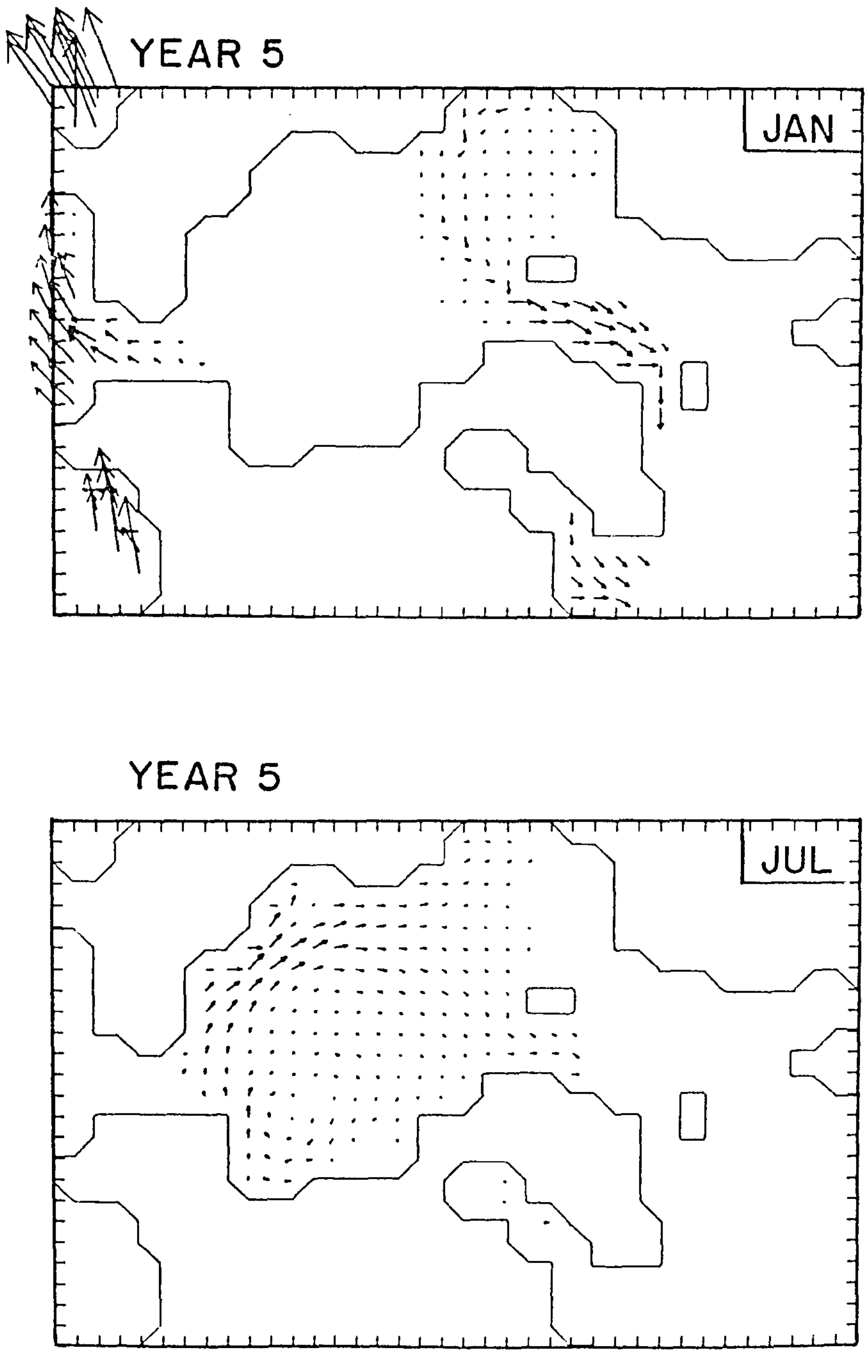

Figure 30. Simulated Arctic ice drift for January and July.

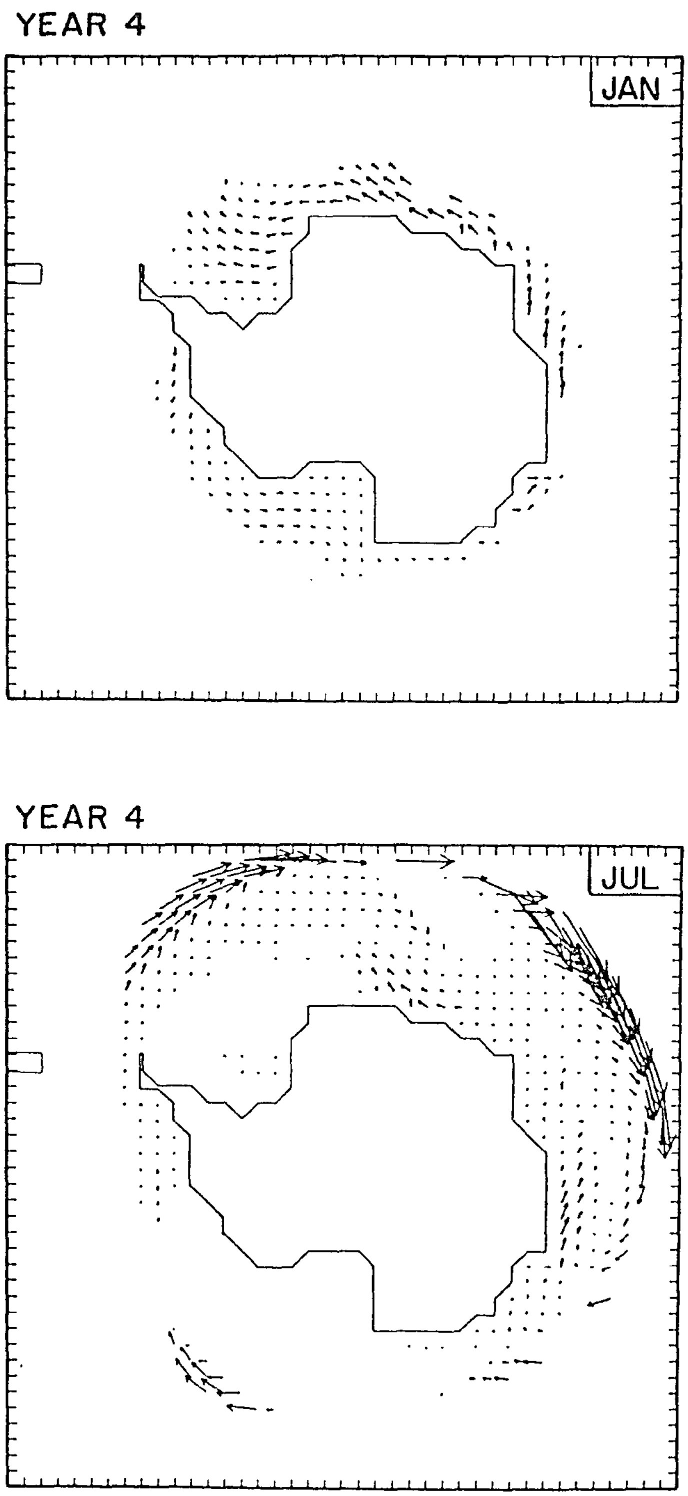

Figure 31. Simulated Antarctic ice drift for January and July.

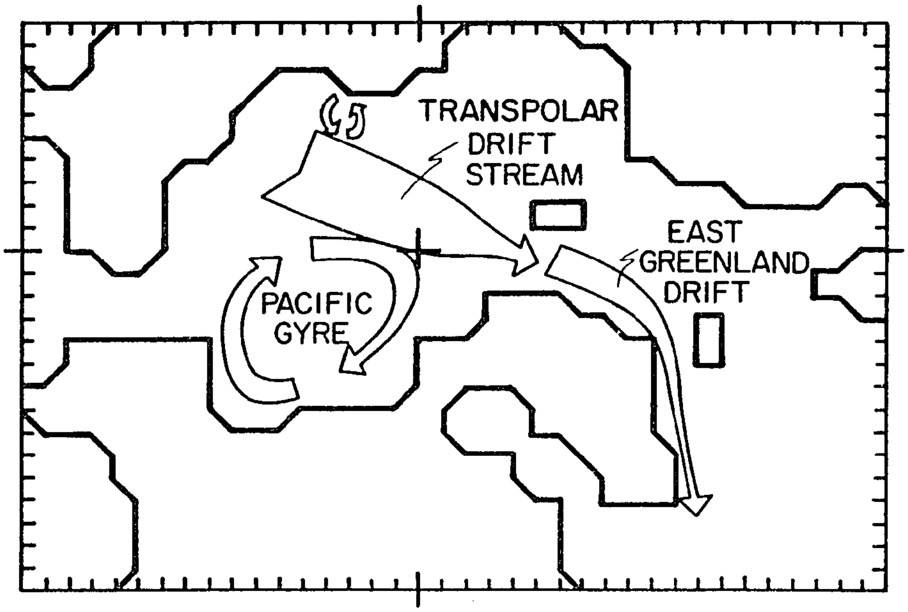

Figure 32. Schematic diagram of the major observed features of Arctic ice drift.

Soviet expedition of 1961 (Bushuyev *et al.*, 1970). However, the simulated January results do not indicate a gyre pattern, and, indeed, the internal ice resistance has reduced the January ice velocities throughout most of the central Arctic to near zero. Although this velocity reduction is probably excessive, two supportive points can be noted regarding these January results. First, the wind field specified for the present model--a field taken from mean monthly observational data (section 4.2.1)--also does not contain a gyre in the Beaufort Sea in the winter months (Figure 7). Second, there is little doubt that winter ice velocities are slowed due to compaction. This second point is illustrated by the reduction of wind coefficients from summer to winter

(Nikiforov *et al.*, 1970; McPhee, 1977) and also by well-documented, observed instances when highly concentrated winter ice has remained motionless. Notably, Pritchard (1976) reports the failure of strong surface winds (4-7 m s^{-1}) to budge a region of compact ice in the Beaufort Sea in February 1976. As the winds of Figure 7 tend to have speeds under 4 m s^{-1}, it is not surprising that the winter ice velocities are near zero.

The Transpolar Drift Stream appears in the simulated results for both January and July (Figure 30), with the continuing southward motion in the East Greenland Drift also prominent in the January results. As for the smaller-scale features of Arctic drift, there is indeed a relatively stagnant region to the north of Greenland and Ellesmere Island in both January and July plots, and there is a slight cyclonic curvature in the region to the east of Severnaya Zemlya in January, though the island itself is not modeled.

The simulated velocity fields for the Antarctic show westerly motion wherever the ice reaches northward of about 58°S (Figure 31). Ice velocities tend to be greatest in this region of strong westerly atmospheric flow, with the weaker velocities near the coast being more variable in direction but predominantly easterly and with cyclonic curvature. The cyclonic flow in the Weddell Sea is well-collaborated by the documented drift of a large iceberg from 1967 to 1976 (McClain, 1976), while the overall flow patterns of Figure 31 correspond closely with the large-scale ocean circulation in the Southern Ocean (Zwally *et al.*, 1976; Tolstikov, 1969).

5.4 Annual Development of Model Results

To place Figures 21-24 in the perspective of the previous model years, Figure 33 presents contour plots of the January and July ice thicknesses for the first four years of the Arctic simulation and Figure 34 presents similar plots for the first three years of the Antarctic simulation. At this point it is worthwhile to recall both that the plots are for the 45th timestep of the month and that the Arctic was initialized with 3.5 m ice and 10% leads in every ocean grid square and the Antarctic with 1.5 m ice and 10% leads in every ocean grid square (Table 5).

Clearly by mid January of the first year much of the excess ice initialized at the equatorward edges of the grid boundaries has melted (Figures 33 and 34). However, the melt is certainly not sufficient in these first 45 timesteps to reduce the ice to a realistic configuration in either hemisphere. By July of the first year the Antarctic extents are close to their year 4 values, though the thicknesses are still somewhat large. By contrast, in the Arctic the extents as well as the thicknesses definitely remain too large during the first July.

Figures 23-24 and 34 show that years 3 and 4 of the Antarctic simulation have close to identical contours,

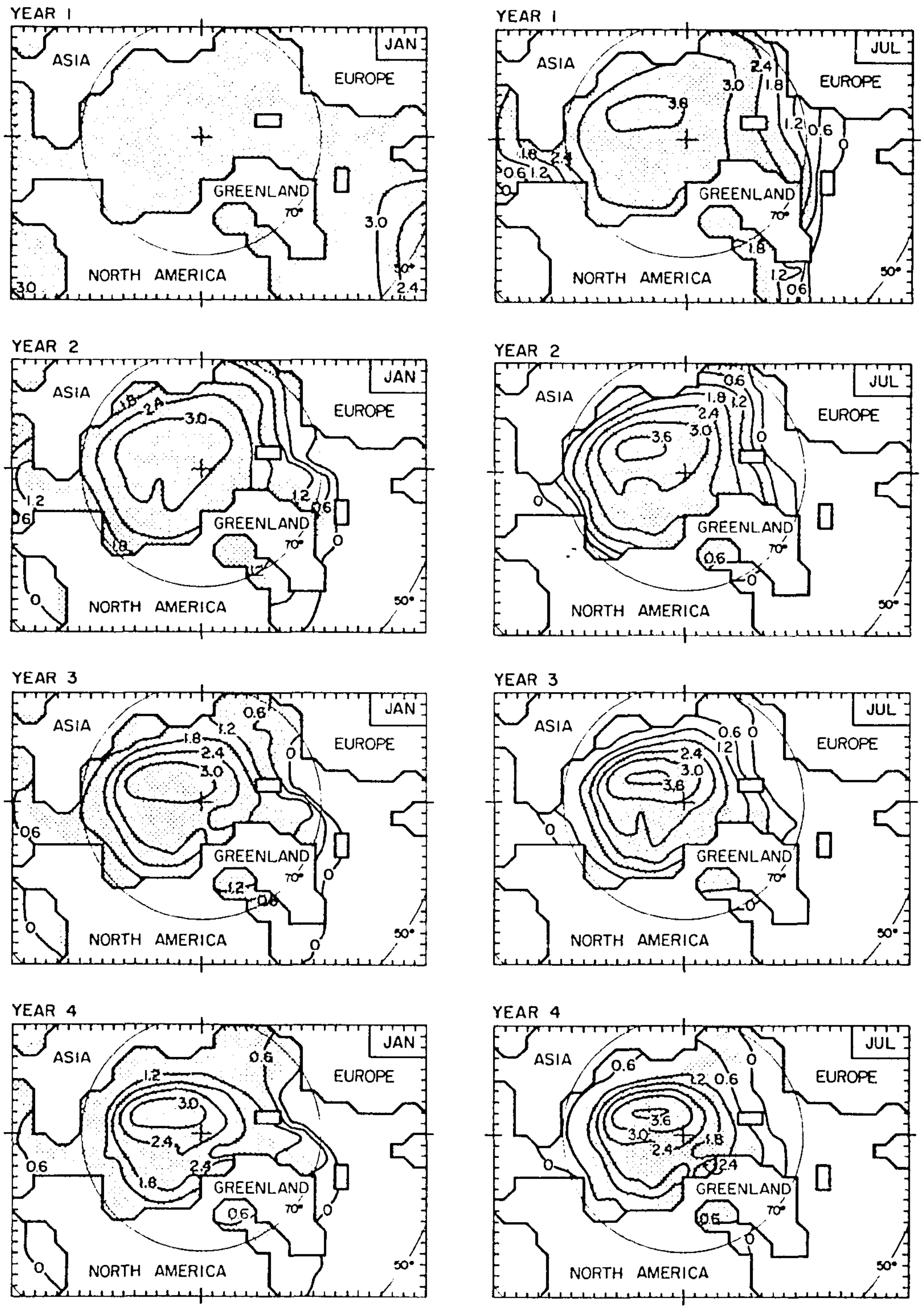

Figure 33. January and July ice thicknesses for the first four years of the Arctic simulation.

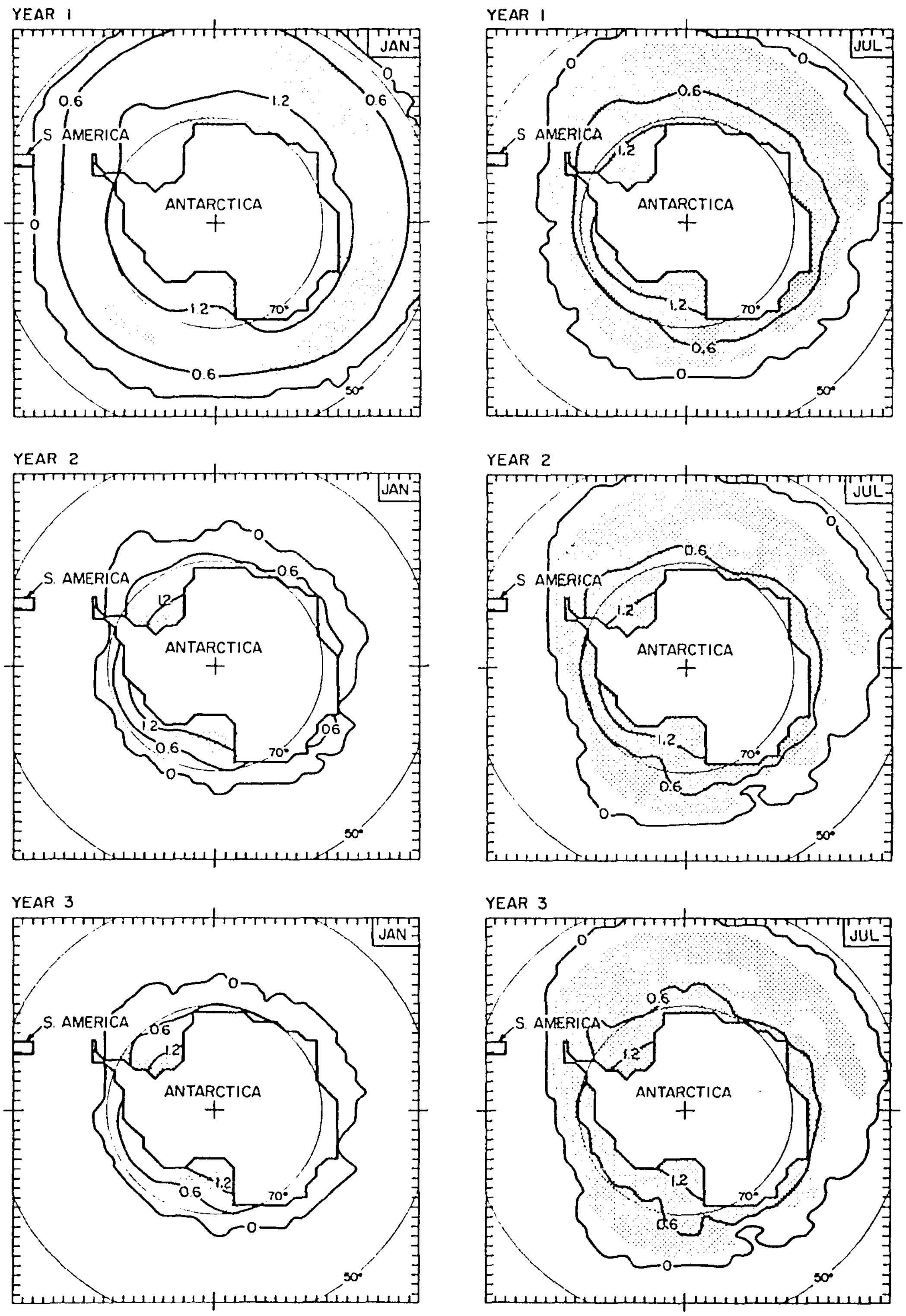

Figure 34. January and July ice thicknesses for the first three years of the Antarctic simulation.

especially in July. Thus by year 4 the model appears to have reached near-equilibrium. In the Arctic (Figure 33) the comparison between years 3 and 4 is not as close, hence the running of the model through five years. Although still not identical, both the January and July results in years 4 and 5 are felt to be close enough to warrant retaining year 5 as the final year of the simulation.

CHAPTER VI

ENERGY BUDGETS

This chapter elaborates on the model results of Chapter V by presenting energy budgets simulated over both ice and leads and by examining these briefly in the context of previously published values. One point is selected for analysis in each hemisphere--a central Arctic point in the Beaufort Sea and a coastal point near Mawson, Antarctica (Figure 35).

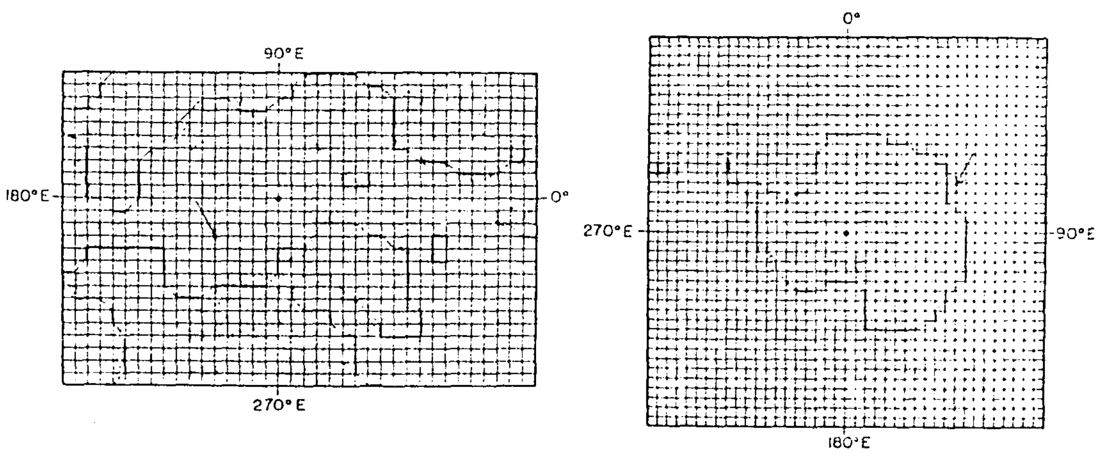

Figure 35. Locations of the Antarctic grid point for Figures 36-38 and of the Arctic grid point for Figures 39-41.

6.1 Antarctic Energy Budgets

Terms in the energy budget for point (32,26) of the southern hemisphere grid are plotted in Figures 36-38. The

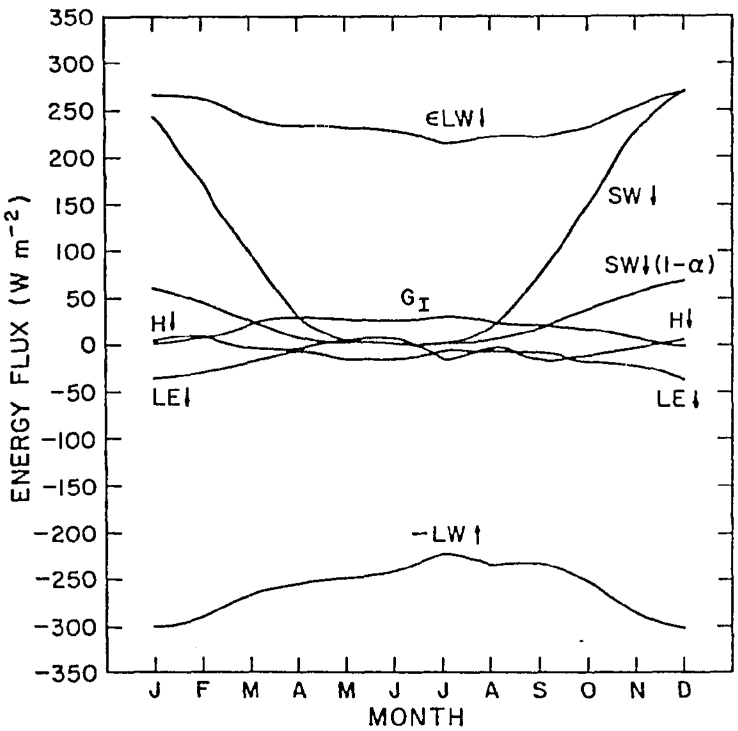

Figure 36. Terms in the energy budget over ice at point (32,26) of the southern hemisphere grid.

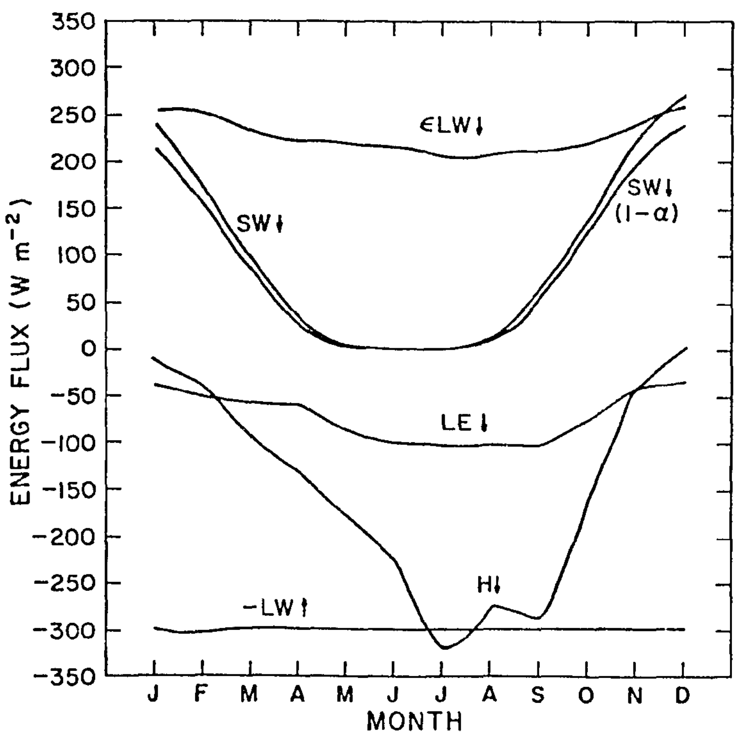

Figure 37. Terms in the energy budget over water at point (32,26) of the southern hemisphere grid.

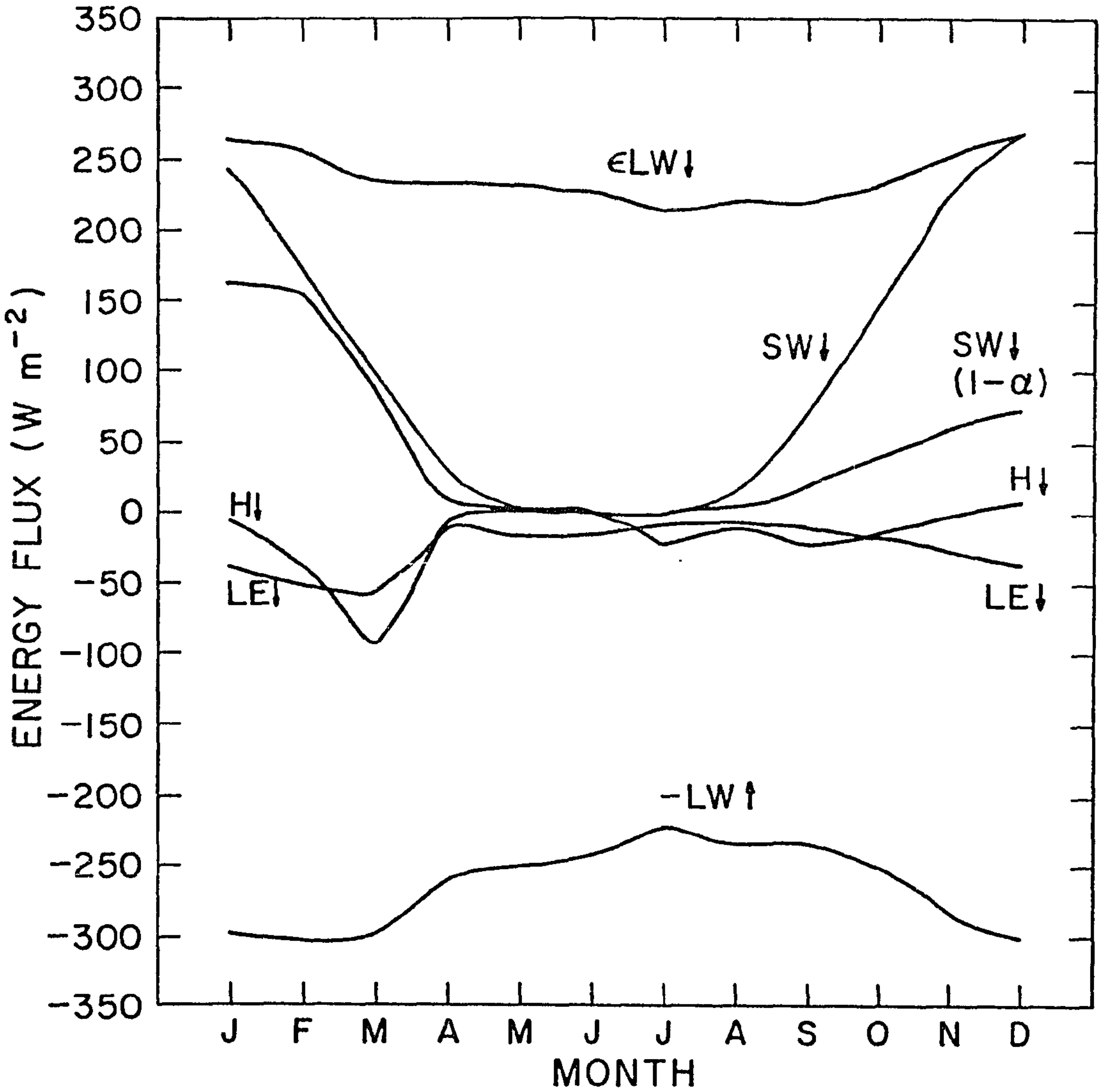

Figure 38. Terms in the energy budget weighted over ice and water at point (32,26) of the southern hemisphere grid.

three diagrams show the energy budgets over ice, over water, and averaged over the entire grid square. Point (32,26), located at 67.36°S, 65.56°E, is the closest ocean grid point to the research station at Mawson, Antarctica. The ice is snow-covered throughout the model simulation.

As expected, the curve for incoming solar radiation (Figures 36-38) peaks near the summer solstice in December and smoothly decreases to 0 at the height of the polar night near the June solstice before smoothly rising again. The solar flux shows considerably more seasonal variation than do the other fluxes over the snow surface (Figure 36), varying from 0 W m^{-2} to 269 W m^{-2}. Although varying less than the solar flux, the longwave and conductive fluxes do vary fairly smoothly in the course of the yearly cycle. The incoming longwave radiation, calculated from the formulation of Idso and Jackson (1969), depends only on air temperatures and cloud cover. It peaks in December and January, the two months of highest air temperatures at point (32,26), and descends to its lowest values in July and September, the two months of lowest air temperatures. The total variation is only from 214 W m^{-2} to 272 W m^{-2}. Outgoing longwave radiation, LW↑, being dependent only on the surface temperature due to the constant emissivity ε_s = 99%, also peaks in summer and reaches a minimum in winter. The reverse is true of the conductive flux, which is driven primarily by the temperature difference between the bottom surface of the ice and the top surface of the snow.

The bottom ice surface is maintained at the freezing temperature T_B = 271.2 K, while the temperature at the top snow surface is calculated through energy balances and tends to follow the air temperatures. The sensible and latent heat fluxes over the snow are generally smaller in magnitude than the other fluxes, and their seasonal variations are less regular (Figure 36).

The magnitudes of sensible and latent heat are considerably greater over leads (Figure 37) than over ice and snow (Figure 36), the reason being the much warmer surface temperature of the water. In fact in July the sensible heat flux is the largest-magnitude term in the heat balance equation over water. The near constancy of the outgoing longwave radiation (Figure 37) derives from the lead surface temperature remaining practically at freezing throughout the year. The slight lowering of the absorbed incoming longwave radiation ($\varepsilon LW\downarrow$) from Figure 36 results from the small contrast in emissivities (ε_s = 99%; ε_w = 97%), while the significant increase in the absorbed shortwave radiation $SW\downarrow\ (1 - \alpha)$ results from the significant contrast in shortwave albedo (α_w = 10%; α_s = 75%). Both the incoming longwave and the incoming shortwave curves ($LW\downarrow$, $SW\downarrow$) are identical, though the former is not actually plotted.

On the curves for the fluxes weighted over the ice and water, the effect of the lead percentage is clear (Figure 38). To allow proper evaluation of this, the monthly lead percentages are listed in Table 6. Also listed are the wind speed, cloud cover, and air, snow, and water temperatures, all being variables which additionally affect the energy balance terms. For most of the year (April through December), the curves of Figure 38 are almost identical to those in Figure 36 since leads cover only 2% of the grid square area. However, from January through March the leads dominate the grid square, thus producing the strong lack of symmetry in the absorbed-solar-radiation curve and the pronounced March dip in the sensible heat flux. As the leads freeze over at the start of winter the magnitudes of the sensible heat, latent heat, and outgoing longwave radiation all dramatically reduce, reflecting the insulating effect of the new ice cover. The fact that incoming solar radiation drops from December to February yet the absorbed radiation more than doubles further illustrates the importance of the leads and in particular the effect of their low relative albedo (Figure 38, Table 6).

6.2 Arctic Energy Budgets

Similar to the figures and table for the Antarctic case, Figures 39-41 present energy budgets and Table 7 monthly values of leads, cloud cover, wind speed, and temperatures for point (13,13) of the Arctic grid. This point is located in the Beaufort Sea at 78.96°N, 210.96°E (Figure 35). As the pattern of fluxes is similar to those of section 6.1 with the expected six-month shift, only additional peculiarities are commented on here.

TABLE 6. Monthly lead percentages, cloud cover, wind speeds, and temperatures at point (32,26) of the Antarctic grid. All values are for timestep 45 of the relevant month in year 4 of the simulation.

Month	Leads* (%)	Cloud Cover (%)	Wind Speed ($m\ s^{-1}$)	Temperatures (K) Air	Snow Surface	Water Surface
Jan.	64.8 -65.4	78.8	5.13	270.59	270.16	271.53
Feb.	96.7	77.3	4.63	268.89	268.10	272.67
March	98.6	75.9	4.11	261.33	261.88	271.43
April	2.0	74.4	4.72	259.51	260.04	271.20
May	2.0	72.9	6.03	258.63	258.15	271.20
June	2.0	71.4	6.54	256.79	256.44	271.20
July	2.0	70.0	6.11	249.68	250.81	271.20
Aug.	2.0	71.4	6.63	253.81	254.17	271.20
Sept.	2.0	72.9	6.52	252.75	253.91	271.20
Oct.	2.0	74.4	5.17	257.96	258.97	271.20
Nov.	2.07 -2.09	75.9	3.97	266.66	267.02	271.20
Dec.	2.21 -2.27	77.3	4.48	271.38	270.76	271.20

*Where the lead-percentage column lists two values, this percentage alters during timestep 45.

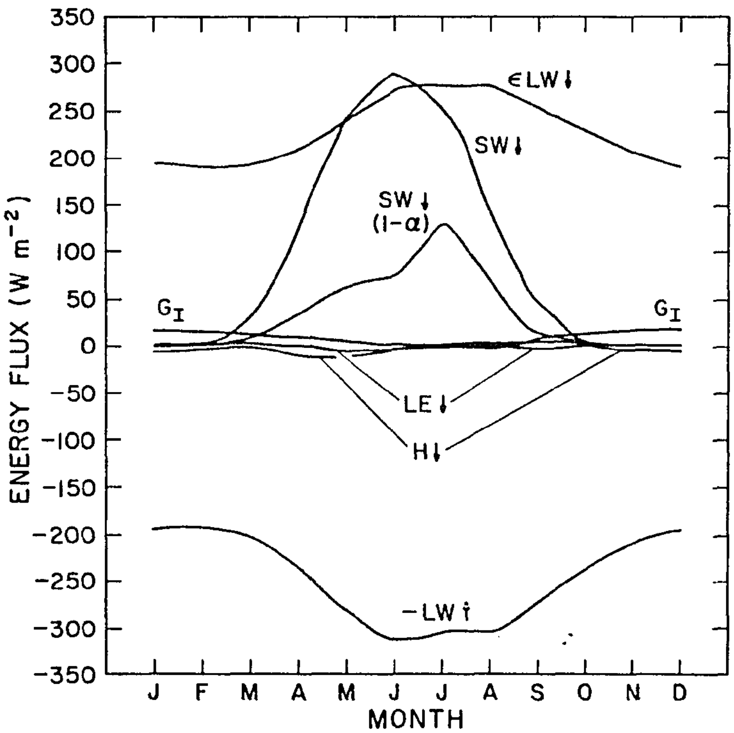

Figure 39. Terms in the energy budget over ice at point (13,13) of the northern hemisphere grid.

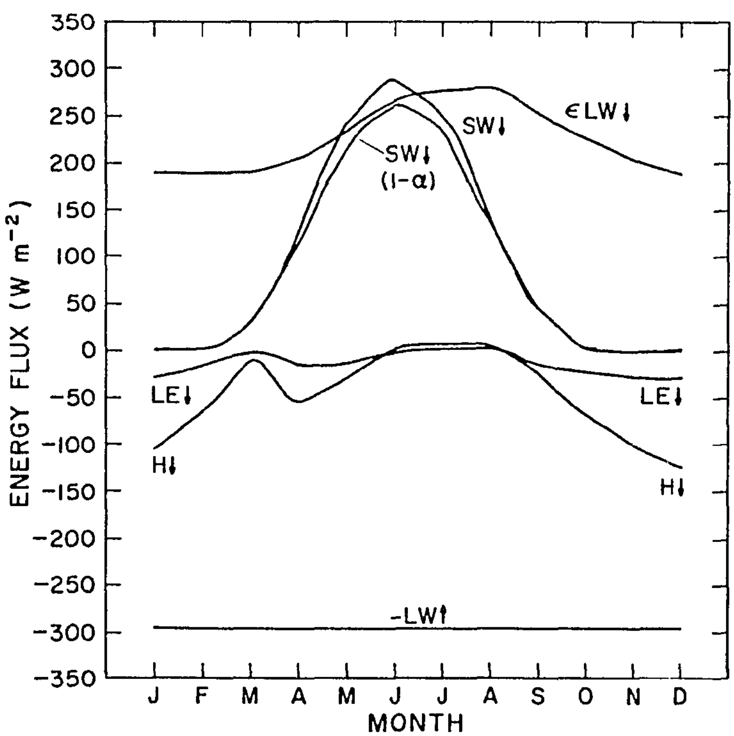

Figure 40. Terms in the energy budget over water at point (13,13) of the northern hemisphere grid.

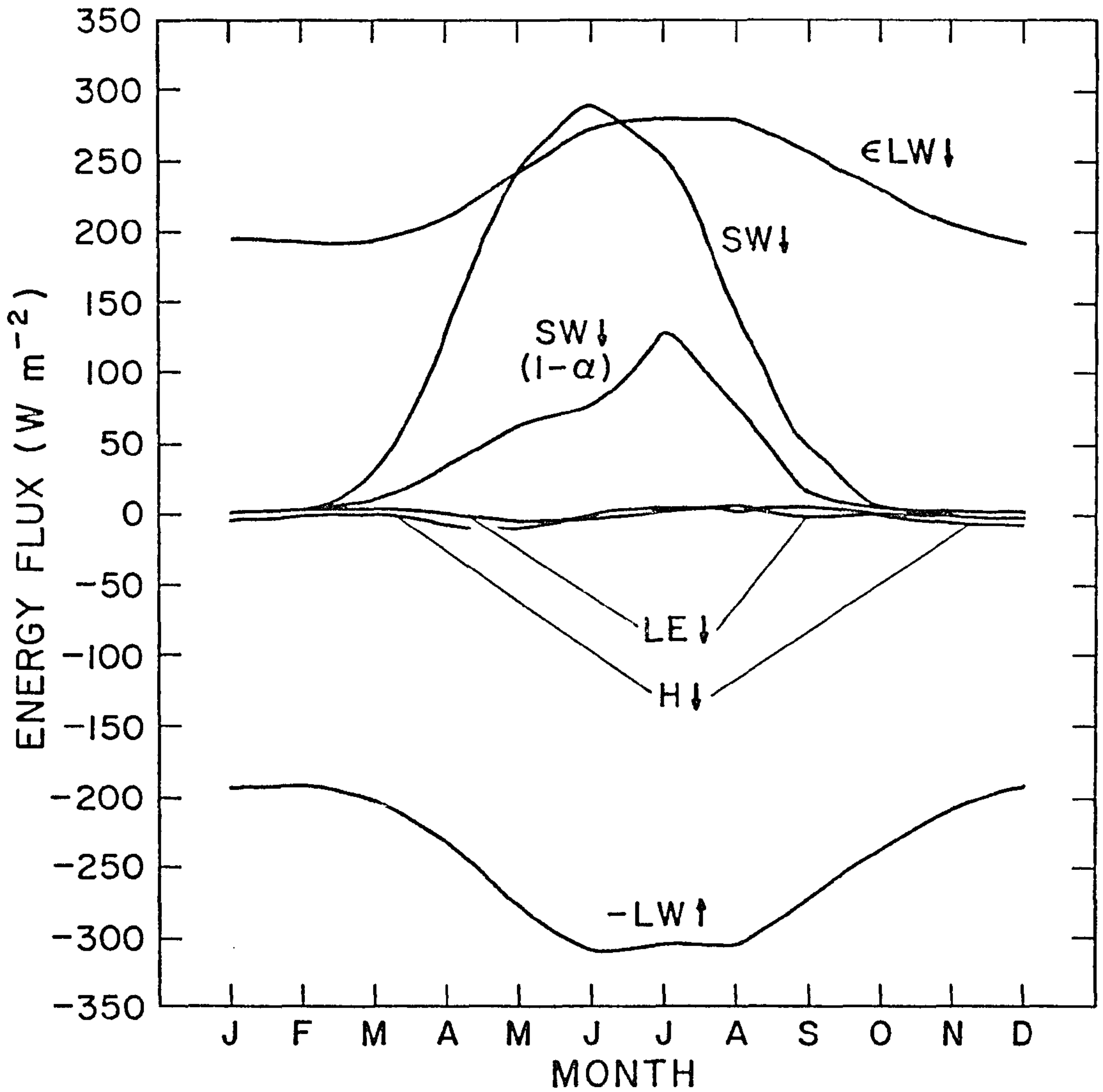

Figure 41. Terms in the energy budget weighted over ice and water at point (13,13) of the northern hemisphere grid.

TABLE 7. Monthly lead percentages, cloud cover, wind speeds, and temperatures at point (13,13) of the Arctic grid. All values are for timestep 45 of the relevant month in year 5 of the simulation.

Month	Leads* (%)	Cloud Cover (%)	Wind Speed ($m\ s^{-1}$)	Temperatures (K) Air	Snow Surface	Water Surface
Jan.	0.5	50	1.54	241.17	243.09	271.2
Feb.	0.5	50	0.86	239.93	242.76	271.2
March	0.5	50	0.17	240.87	245.94	271.2
April	0.5	55	1.03	249.09	253.69	271.2
May	0.51	70	1.34	261.55	265.69	271.2
June	0.78	75	0.90	271.06	273.15	271.2
July	0.52 -0.53	75	0.72	273.46	273.05	271.2
Aug.	0.67 -0.68	80	0.81	273.10	273.05	271.2
Sept.	2.09 -2.08	80	1.74	264.77	264.03	271.2
Oct.	3.42 -3.38	70	1.75	255.25	255.16	271.2
Nov.	0.5	60	1.63	245.91	247.59	271.2
Dec.	0.5	50	1.64	240.95	243.17	271.2

*Where the lead-percentage column lists two values, this percentage alters during timestep 45.

Among the noticeable differences between the curves of Figures 36-38 and those of Figures 39-41, at least one derives from the type of ice surface at the two localities. In the Beaufort Sea the snow covering melts off at the start of the summer season, leaving the ice bare during July and August, while at point (32,26) in the Antarctic at least a slight snow cover remains throughout the year. This implies that the relevant surface albedo is 50% rather than 75% and the relevant emissivity is 97% rather than 99% during July and August for ice at the Beaufort Sea point. The difference is very apparent in the shortwave absorption curve, $SW{\downarrow}\cdot(1 - \alpha)$, both over ice alone and weighted over the grid square. In spite of the nearly symmetric curve for incoming solar radiation, the absorption curve is clearly asymmetric, the reason being the albedo decrease in July and August.

The generally lower magnitudes of $H{\downarrow}$ and $LE{\downarrow}$ in Figures 39-41 *versus* those in the Mawson curves of Figures 36-38 are predominantly due to the lower wind speeds. Similarly, the lessened upward sensible and latent heat fluxes in March compared to February and April are due to the very low wind speed (0.17 m s^{-1}) specified for March at (13,13). Other differences between Figures 36-38 and Figures 39-41, such as the greater length of the polar night and the stronger yearly cycle of solar and longwave radiation in Figures 39-41, can easily be reasoned from the more poleward location of the Arctic point.

6.3 Energy Budget Comparisons

As in the case of ice thicknesses, concentrations, and extents (Chapter V), there exist wide differences in published values of the various terms in the energy budget. This is particularly true for the fluxes of sensible and latent heat, as illustrated by contrasts between the values of Vowinckel and Taylor (1966) and those of Badgley (1961). Both sources calculate monthly mean fluxes for the central Arctic, with the results reported for the entire region, weighting the ice and open-water percentages; yet for the annual totals Badgley presents a sensible heat gain of 0.419×10^{21} J while Vowinckel and Taylor present a sensible heat loss of 1.59×10^{21} J. The two annual figures for latent heat at least have the same sign, being a 1.30×10^{21} J loss in Vowinckel and Taylor and a 0.335×10^{21} J loss in Badgley, a difference of close to a factor of four.

In view of such variability in reported flux estimates, no attempt is made here to present a thorough comparison of model results with published data. Instead, only a small set of illustrative comparisons is included, and this is guided largely by the types of data available for the two hemispheres. First a tabulation of one source's heat budget for the central Arctic is given, along with the calculated values at point (13,13); then more detail is presented for the sensible and latent heat fluxes over Arctic ice; and finally, the February energy budget over water near Mawson, Antarctica is examined.

The latter is the one case where data have been collected for a specific spot and comparisons are made against the simulated values for that same locality.

The monthly energy budget terms plotted in Figure 41 are listed in Table 8. These values are for the grid-square average, which is obtained by weighting the ice-covered and ice-free portions. Also listed in Table 8 are the corresponding values presented in Vowinckel and Orvig (1970) and earlier in Vowinckel and Orvig (1966) and Vowinckel and Taylor (1966). The Vowinckel, Orvig, and Taylor values represent an average for the central Arctic, rather than for a specific location.

In spite of the generalized latitude appropriate for the comparative data, the simulated values of absorbed solar radiation in the present model are quite close to the Vowinckel and Orvig values for each season except late spring. The lower simulated values in May and June probably derive from the omission of puddling effects in the model. As puddles form on the ice the resultant decrease in surface albedo increases the absorbed radiation.

The simulated values for the outgoing longwave radiative flux correspond quite well with the Vowinckel and Orvig values from November through June but tend to be about 8% too low for the four months July-October. This deviation is less than might be expected considering the model simplifications and the imprecision of the Vowinckel and Orvig geographical location. Still, a possible further explanation for the lower simulated

TABLE 8. Energy fluxes weighted over ice and leads in the central Arctic (W m^{-2}).

Flux	Source*	Jan.	Feb.	March	April	May	June	July	Aug.	Sept.	Oct.	Nov.	Dec.
$SW\downarrow$	S	0	0	27	128	242	285	254	145	45	1	0	0
$SW\downarrow(1-\alpha)$	S	0	0	7	32	61	73	128	73	12	0	0	0
	VO	0	0	10	38	90	125	124	74	19	1	0	0
$LW\downarrow$	S	192	190	192	209	242	273	283	284	256	228	206	192
	VO	163	146	157	177	244	278	310	304	265	234	179	168
$\varepsilon LW\downarrow$	S	190	188	190	207	239	270	274	276	253	226	204	190
$LW\uparrow$	S	197	195	206	233	280	312	306	306	273	240	211	197
	VO	201	183	206	249	284	320	338	332	293	265	222	210
$H\downarrow$	S	-8	-7	-2	-12	-13	-4	1	0	2	-2	-7	-10
	VT	2	1	1	-15	-16	-11	1	-9	-16	0	1	1
$LE\downarrow$	S	-1	-1	0	-2	-8	-5	0	3	-4	-3	-2	-1
	VT	2	0	0	-1	-8	-7	-3	-11	-11	-2	1	0

*Sources are: S = Model simulation for midmonth, year 5 at Arctic grid point (13,13).
VO = Vowinckel and Orvig (1966), with a units conversion.
VT = Vowinckel and Taylor (1966), with a units conversion.

values at least in September and October is that the estimated lead percentages by Vowinckel and Orvig could well be above the very slight 2-4% leads simulated by the model. The somewhat greater deviations between the Vowinckel and Orvig and simulated values for incoming longwave radiation are presumably due to location, atmospheric temperatures, and/or cloud cover. The tendency is for the simulated values to exceed the Vowinckel and Orvig values during winter and to fall below them during summer.

Turning to the turbulent fluxes of Table 8, we find the correspondence between simulated and previously estimated values to be much worse than it is in the case of the radiative fluxes. Consequently, Table 9 has been included showing recent calculations by Maykut (1976) on the sensible and latent heat fluxes over ice of thicknesses 0.8 m and 3 m in the central Arctic. Maykut also includes several additional categories of ice thinner than 0.8 m, but as the simulated year 5 thicknesses at point (13,13) range only from 1.2 m in August and September to 2.2 m in March and April, the two thickest of Maykut's categories are the appropriate ones here. Maykut does not present values for July or August.

The deviations calculated by Maykut for 3 m ice *versus* 0.8 m ice are clearly significant (Table 9). In the case of sensible heat even the direction of the flux is opposite in most months. In view of these contrasts it does seem that the simulated fluxes are acceptable, and in fact for both sensible

TABLE 9. Conductive, sensible, and latent heat fluxes toward the snow-air or ice-air interface in the central Arctic (W m^{-2}).

Flux	Source*	Jan.	Feb.	March	April	May	June	July	Aug.	Sept.	Oct.	Nov.	Dec.
H↓	S	-8	-6	-2	-12	-13	-4	1	0	3	0	-7	-9
	M(3m)	17	16	12	9	-2	-8			-5	0	6	11
	M(.8m)	-31	-31	-42	-53	-61	-54			-17	-18	-27	-30
LE↓	S	-1	-1	0	-2	-8	-5	0	-3	-4	-2	-2	-1
	M(3m)	0	0	0	0	-4	-10			-9	-4	0	0
	M(.8m)	-16	-9	-4	-3	-2	-2			-2	-5	-19	-39
Conductive	S	14	14	12	8	2	-1	-2	-3	8	12	14	16
	M(3m)	14	13	11	6	3	-6			11	13	13	15
	M(.8m)	66	70	74	60	27	-1			6	31	55	66

*Sources are: S = Model simulation for midmonth, year 5 at Arctic grid point (13,13).
M(3m) = Maykut (1976) for ice of thickness 3 m, with a units conversion.
M(.8m) = Maykut (1976) for ice of thickness 0.8 m, with a units conversion.

and latent heat the simulated values fall between the 0.8 m and 3 m values of Maykut in all but two of Maykut's ten months.

Table 9 also lists the simulated and Maykut (1976) values for the conductive flux through the ice. There is a remarkably close correspondence between the simulated values and those of Maykut for 3 m ice. Additionally, in each of the two worst months for this correspondence--June and September--the simulated values are close to the 0.8 m values.

In the Antarctic, a year-round energy budget analysis over both ice and open water is being attempted at Mawson, Antarctica (Allison and Akerman, 1977). It was for this reason that point (32,26) was selected as the southern hemisphere point for Figures 36-38, although the observational work at Mawson is planned to continue at least through 1978. As of September 1977, preliminary results are available only for selected dates in February and only over open water; thus the comparisons in Table 10 are restricted to February leads.

The simulated February 15 fluxes fall between the February 15 and February 18 values of Allison and Akerman (1977) for each of their three radiative terms. In addition, the simulated sensible heat falls between the February 11 and February 18 values. Although the latent heat does not compare as nicely, it does seem that on the whole the correspondence between the simulated and comparative values in Table 10 is quite good, especially considering that the latent heat is the only flux simply estimated by Allison and Akerman and not

TABLE 10. February energy fluxes over open water near Mawson, Antarctica.

Flux	Source*	Value (W m^{-2})
SW↓	AA(15)	255
	S	178
	AA(18)	60
SW↓(1−α)	AA(15)	228
	S	161
	AA(18)	56
LW↓	S	263
εLW↓	S	255
LW↑	S	304
net LW	AA(15)	-111
	S	-49
	AA(18)	-45
H↓	AA(11)	-1
	S	-39
	AA(18)	-74
LE↓	AA(11)	-81
	S	-53
	AA(18)	-93

*Sources are: S = Model simulation for midmonth, year 4 at Antarctic grid point (32,26).
AA(11), AA(15), AA(18) = Allison and Akerman (1977) for fluxes over water in a small embayment about 200 m to the west of Mawson, on February 11, 15, and 18, respectively, of 1977.

measured.

The fact that the simulated February fluxes correspond as well as they do to the Allison and Akerman values (Table 10) suggests that the model's flux calculations produce reasonable results. Stronger statements are not warranted, in view of the limited observational data, the real-world variability, and the model simplifications. Ideally, the test of the model values should be made against climatological means from decades of observational data, but these are simply not available. Day-to-day variation in the real world can depend on cloud cover, atmospheric stability, the passage of cyclones and anti-cyclones, and the outflow of katabatic winds from the continent. Furthermore, the fluxes have noticeable diurnal variations, some of which are examined in Allison (1973). The current model cannot, and was not meant to, simulate such short-term variations.

CHAPTER VII

MODEL EXPERIMENTS

In this chapter several individual changes are made from the standard case (Chapter IV) and the resulting ice distributions are compared with those of Chapter V. In general the comparisons are made for the months of January and July, though peculiarities in other months are noted if these are not apparent from the January or July results. To avoid excessively wasting computer resources, most of the experiments are not run for a full four years in the Antarctic or five years in the Arctic. The basic trends often become apparent within the first few months.

7.1 Thermodynamics *versus* Dynamics

In this section two cases are examined, one where the ice is not transported horizontally and a second where the ice is not melted or accreted vertically. In other words we here separate the thermodynamic and mechanical processes, hoping to reveal something of their somewhat different contributions to the large-scale geographic configuration of sea ice.

The experiments without dynamics show only slight contrasts with the standard case. In the Antarctic (Figure 42) the extents are generally not quite as great as when ice transport

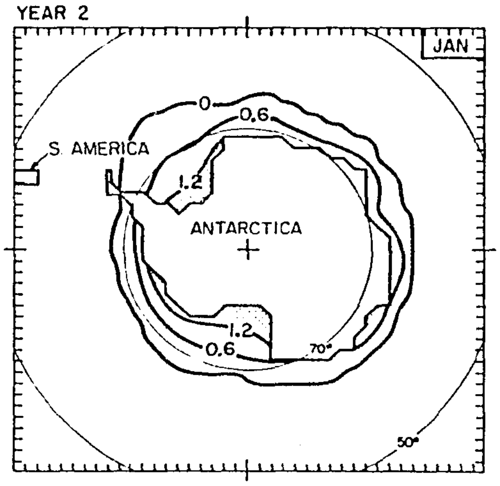

Figure 42. Simulated January and July ice thickness in the Antarctic after eliminating ice dynamics. Contours show thickness in meters, while shading indicates ice compactness above 90%.

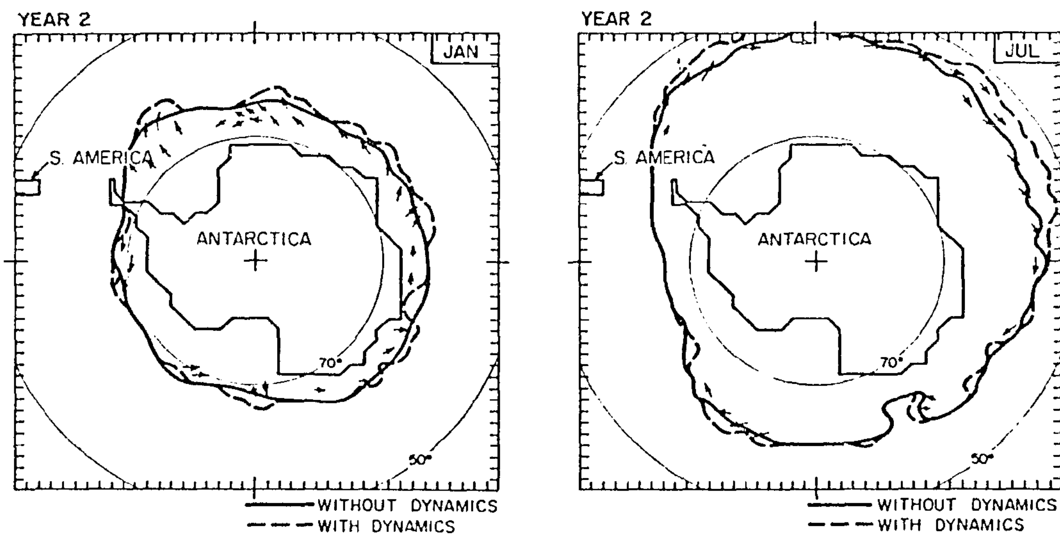

Figure 43. January and July ice extents in the Antarctic with and without ice dynamics simulated. Arrows indicate the directions of the simulated ice velocities.

allowed a slight equatorward flow, as in Figure 34. Figure 43 overlays the extents for both cases and plots the directions of the ice velocity near the ice edge. In regions where the meridional component of flow is southerly the extent is greatest when transport is included, while in regions of negligible flow the extents are identical and in the few regions with a northerly flow component the extents are greatest without transport (Figure 43). Naturally the contrast between extents with or without transport would be much greater if the predominant ice flow at its equatorward edge had been meridional rather than zonal.

In the North Atlantic the simulated meridional flow component at the ice edge tends to be somewhat stronger than in the Antarctic. As this flow is equatorward, the ice extent is thereby more noticeably reduced when transport is eliminated (Figure 44). Furthermore, the region of ice of thickness greater than 3 m is also slightly reduced without transport (Figure 45 *versus* Figure 33), presumably reflecting the small outward flow component in the Pacific Gyre. At the same time, the ice is more compact without transport (Figure 46), again reflecting the divergent velocity component. Local regions of convergent flow will naturally show less compaction without transport; however, on a large scale, in the Arctic the transport increases the extent of the ice and decreases the compactness.

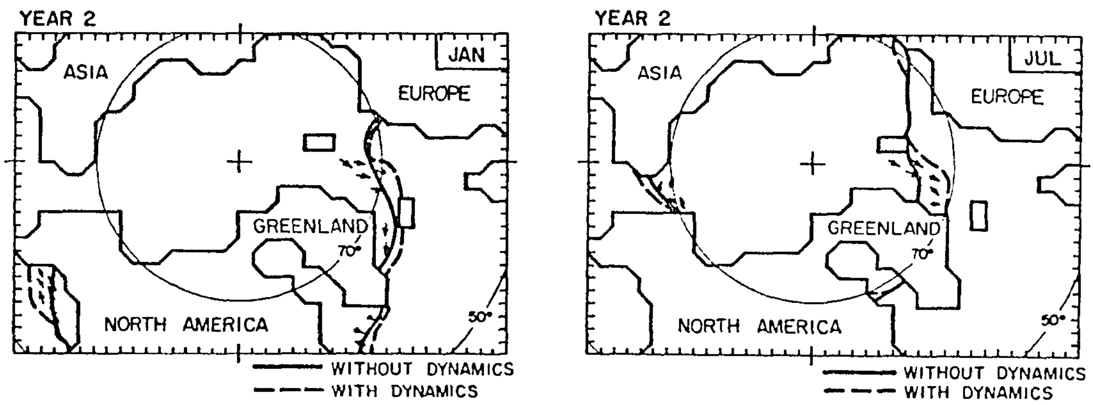

Figure 44. January and July ice extents in the Arctic with and without ice dynamics simulated. Arrows indicate the directions of the simulated ice velocities.

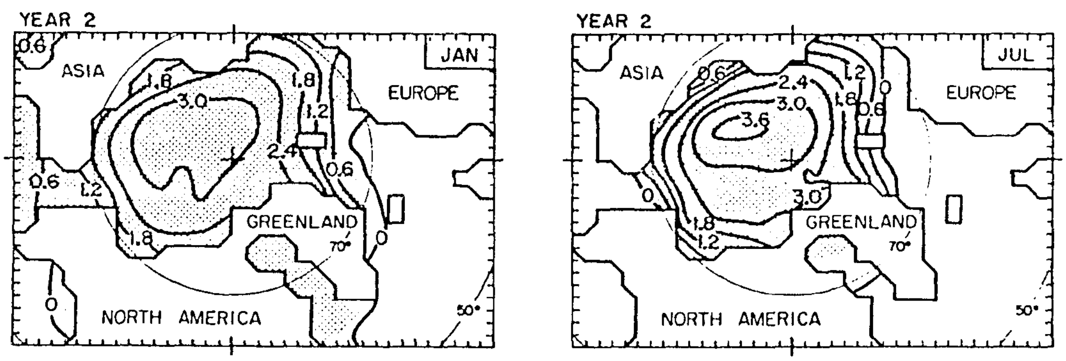

Figure 45. Simulated January and July ice thickness in the Arctic after eliminating ice dynamics. Contours show thickness in meters, while shading indicates ice compactness above 90%.

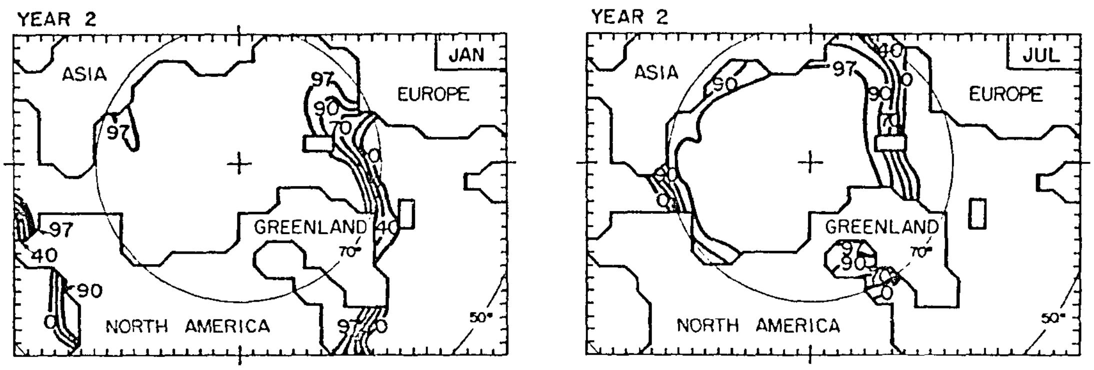

Figure 46. Simulated January and July ice compactness (%) in the Arctic after eliminating ice dynamics.

When thermodynamics is eliminated and only transport is modeled, the normal meaning of the yearly cycle vanishes. Modeling transport alone has practical meaning only over much shorter time spans, in which event it can become valuable for ice-compaction forecasts for shippers and others maneuvering in polar oceans. However, when a longer-term model such as the present one is run without thermodynamics, the effect is to increase the ice concentration to the maximum allowable in all regions with convergent flow and to decrease the ice cover to zero in regions of divergent flow.

7.2 Oceanic Heat Flux - Constant Values

As was noted in Chapter V, the overall simulated Antarctic ice is perhaps thinner than the ice in the real world. One way to increase the thickness is to decrease the oceanic heat flux $F\uparrow$ from its 25.0 W m^{-2} value in Chapter IV. However, a reasonable expectation is that such a decrease will have the added effect of increasing ice extent, which is not desired, as the Antarctic extents (Figures 23-24) already seem somewhat too large rather than too small.

By halving the oceanic heat flux to 12.5 W m^{-2}, peak ice thicknesses in the Weddell Sea increase to 2.4 m in January of year 2 and to 3.0 m in July of year 2 (Figure 47). Both these peak thicknesses are up from 1.5 m in year 2 of the standard case. The January extents and concentrations are noticeably greater than in the standard case, though the July extents are only slightly greater and in some regions are actually less. Similarly, the July concentrations are greater than in the standard case though not so noticeably so as in the January case. It thus appears that halving the ocean heat flux significantly increases ice thicknesses throughout the year but affects ice extents and concentrations much more in summer than in winter.

The oceanic heat flux has been altered in the Arctic simulation as well, being increased from 2.0 W m^{-2} first to 3.0 W m^{-2} and then to 4.0 W m^{-2} (Figure 48). Although both additional simulations were run for a full five years, the

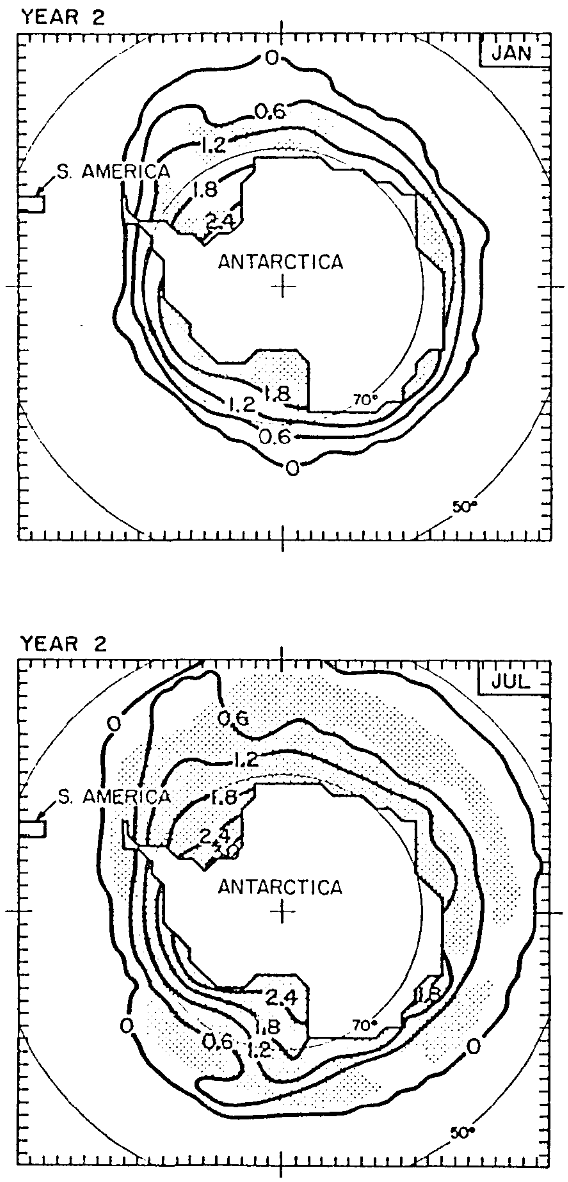

Figure 47. Simulated January and July ice thicknesses in the Antarctic after reducing the oceanic heat flux to 12.5 W m^{-2}. Contours show thickness in meters, while shading indicates ice compactness above 90%.

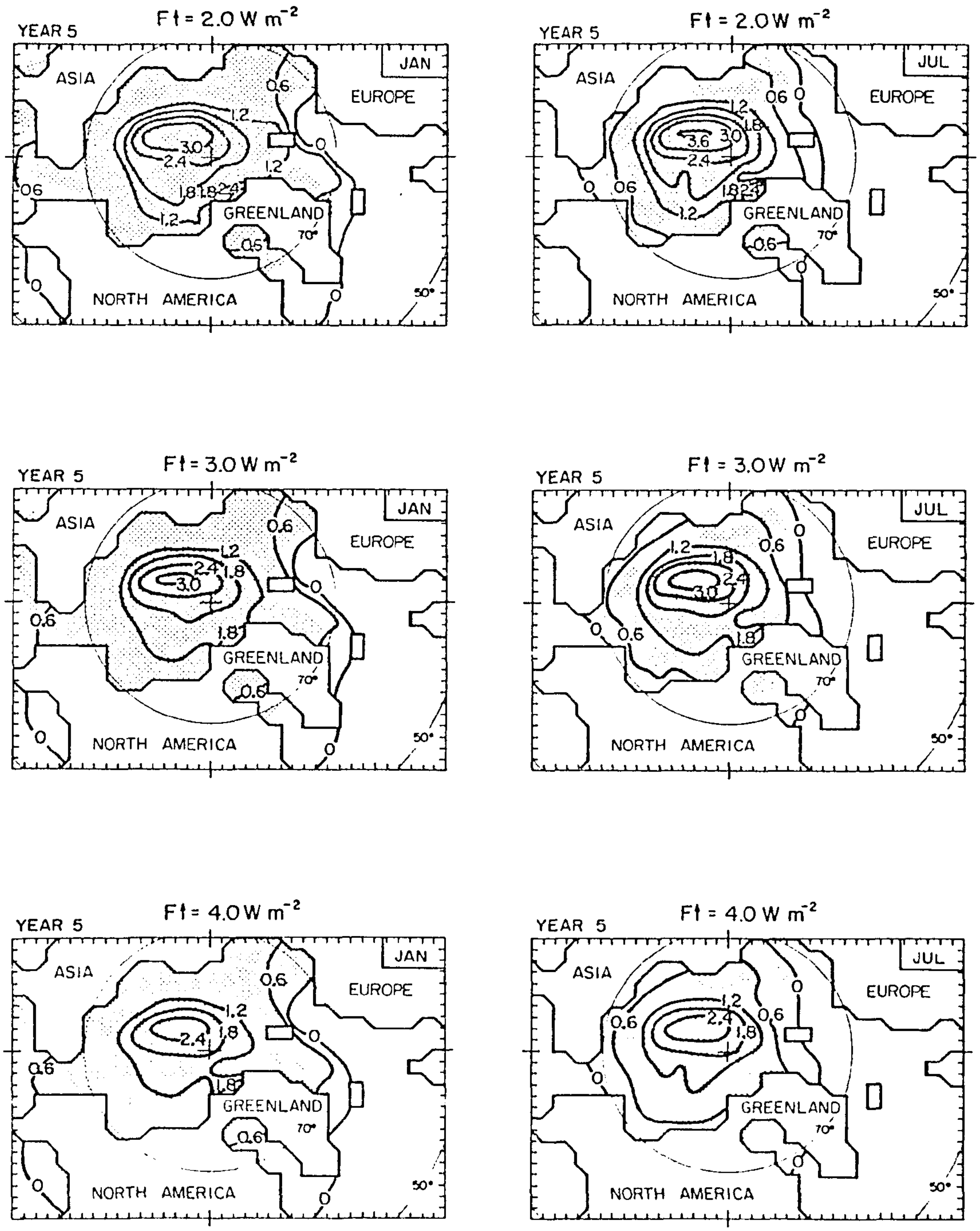

Figure 48. Simulated January and July ice thicknesses in the Arctic for three values of the oceanic heat flux. Contours show thickness in meters, while shading indicates ice compactness above 90%.

thicknesses have not stabilized but instead are continuing to decrease from years 4 to 5 due to the ablation from the increased ocean flux. This contrasts with the extents, which indeed have nearly reached equilibrium from year to year.

In terms of the year 5 results, there is a steady decrease of central Arctic thickness in January from 3.3 m to 3.0 m to 2.7 m and in July from 3.6 m to 3.0 m to 2.7 m as the ocean flux increases from 2 to 3 to 4 W m^{-2}. On the other hand, the January extents and concentrations are practically identical in the three cases, and the July extents are only slightly different, being most noticeably lessened by the increased flux in the region around Spitsbergen.

To conclude: a change in the ocean heat flux affects thickness much more than extent or concentration of the ice and it affects summer results more than winter results.

7.3 Oceanic Heat Flux - Calculated Values

Continuing with the ocean heat flux, this section presents results from calculating the flux as proportional to the temperature difference between the ocean mixed layer and the bottom of the ice:

$$F\uparrow = C\ (T_{W'} - T_B)\ . \tag{78}$$

As explained in section 4.4, the proper proportionality constant C is unknown. However, using a value of 200 W m^{-2} K^{-1}, a value lying within the range of estimates referenced in section 4.4, the model obtains the results of Figures 49 and 50. In both

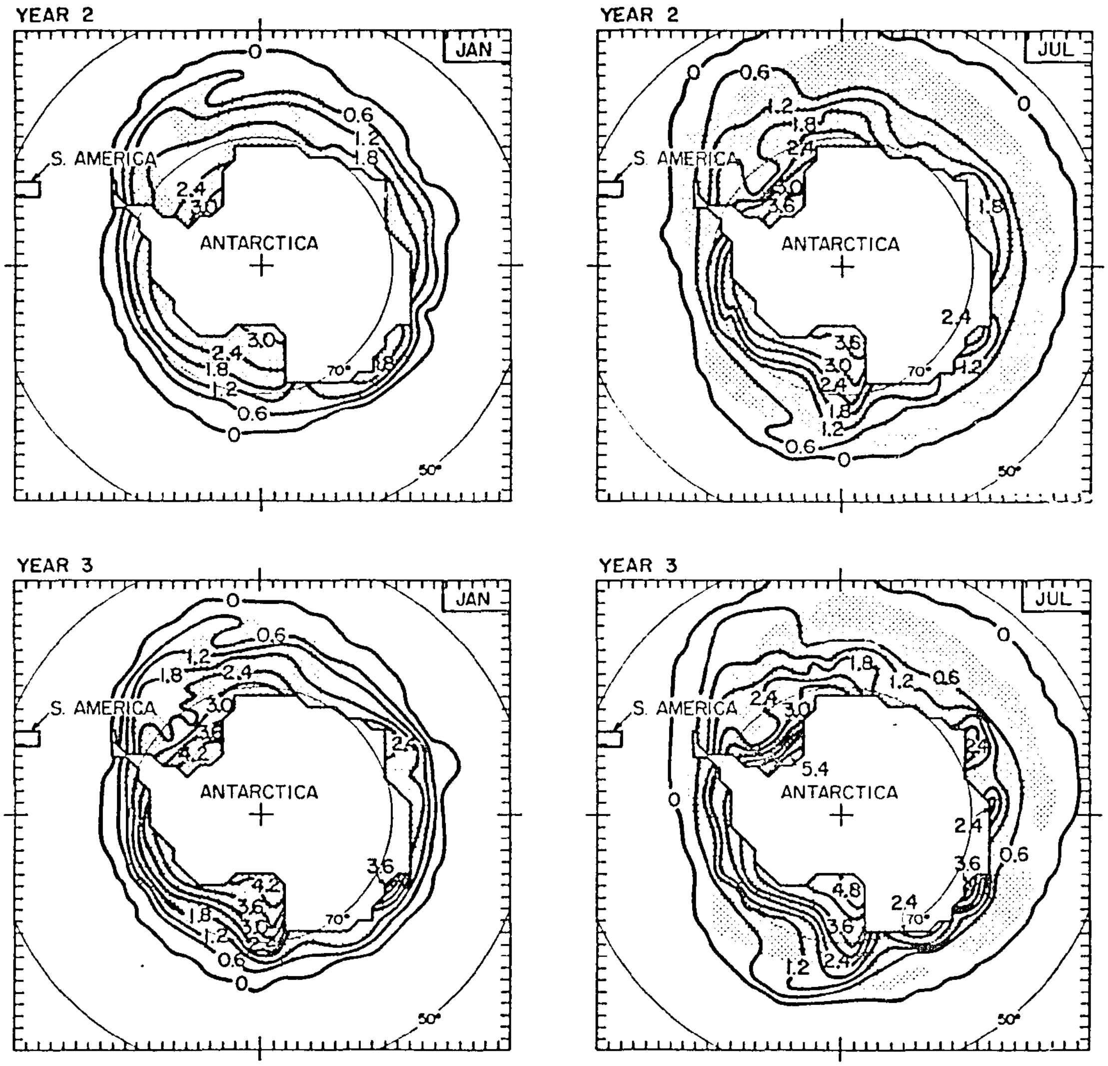

Figure 49. Simulated January and July ice thickness in the Antarctic with a calculated oceanic heat flux: $F\uparrow = C(T_{W'} - T_B)$. Contours show thickness in meters, while shading indicates ice compactness above 90%.

hemispheres, year 3 ice thicknesses exceed those of the standard case, and, furthermore, they are continuing to increase substantially from one year to another.

The Antarctic results with an ocean heat flux calculated from equation (78) are particularly bad. Even in summertime January the thicknesses reach 4.2 m near the continent in year 3, having increased roughly 1.5 m from year 2. As the proper thicknesses are believed to be closer to 1-1.5 m, the calculated ocean heat flux is clearly not allowing sufficient ablation from the bottom ice surface. Relatedly, the ice extents and concentrations are too great, particularly in January. As the January extent and concentrations noticeably exceed those of the standard case and the standard case values were definitely not too small, this is further evidence of the inappropriateness of using (78) with $C = 200\ W\ m^{-2}\ K^{-1}$, at least in the Antarctic.

It might be conjectured that the poor results using equation (78) are due to an inappropriate choice of the proportionality constant C. However, tests with higher values of C have obtained only a delay in the difficulties of excessive ice growth and not an elimination of the problem. The basic difficulty appears to be that the temperature of the water underneath the ice, $T_{w'}$, quickly reaches, or at least becomes very close to, the freezing temperature 271.2 K. Once $T_{w'}$ reaches this freezing point, then the heat flux calculated from equation (78) becomes 0 regardless of the value of C.

It should be mentioned that, in the Arctic, even if the heat flux does go to 0, the model produces a reasonable simulation. Indeed, the model has been run in the Arctic with $F\uparrow = 0.0$, and the results (Figure 51) show only a slight thickening and expansion of the ice cover from the standard case (Figure 33). This is definitely not the situation in the southern hemisphere, as Figure 49 shows.

The difficulties in the Antarctic can be circumvented by allowing interaction between the mixed layer and the water beneath. An upward flux from deeper waters would allow computational warming of the mixed layer and hence a positive flux from equation (78). Alternatively, a proportion of the flux could be carried unchanged through the mixed layer, thereby acting directly on the undersurface of the ice. However, the magnitude of the flux to the ocean mixed layer from beneath varies significantly with location and time, and proper values of this variable are no better known than for the flux from the mixed layer to the ice.

7.4 Input Temperatures

As section 5.1 detailed, there exist significant interannual variations in ice extent in both the Arctic and Antarctic. Haupt and Kant (1976) list five important factors contributing to this variation: ocean and atmospheric circulation, temperatures of the air and water, location, ocean size and salinity, and tides. Although their study deals specifically with the Arctic, the five factors could apply to the Antarctic as well.

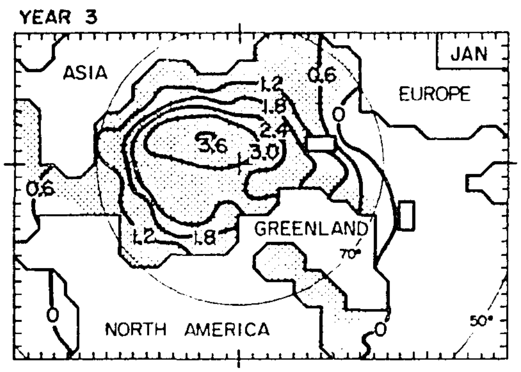

Figure 50. Simulated January and July ice thickness in the Arctic with a calculated oceanic heat flux: $F\uparrow = C(T_{w'} - T_B)$. Contours show thickness in meters, while shading indicates ice compactness above 90%.

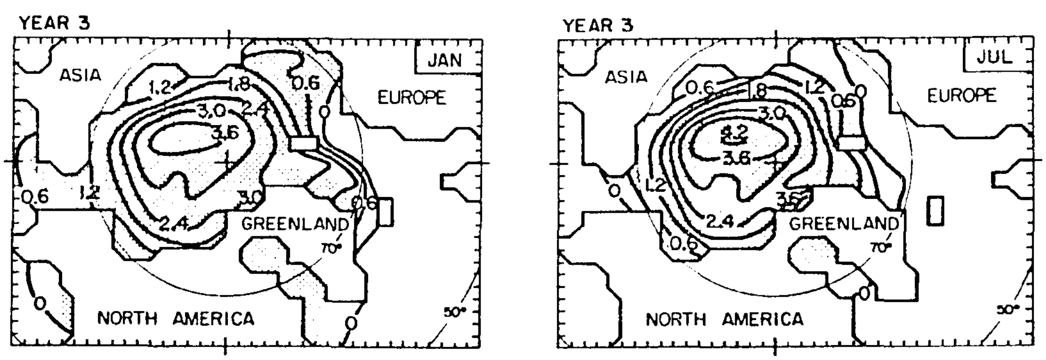

Figure 51. Simulated January and July ice thicknesses in the Arctic when no heat flux is allowed from the ocean mixed layer. Contours show thickness in meters, while shading indicates ice compactness above 90%.

After examining the first three factors, the Haupt and Kant study concludes that in the Barents Sea the ice variations can be largely explained by the atmospheric pressure and temperature, with severe ice winters (e.g., 1965/66, 1968/69) showing a large positive pressure anomaly and with winters of ice minima (e.g., 1972/73, 1973/74) showing a negative pressure anomaly. They find variations in the Norwegian Sea to be less easily explained, requiring ocean factors as well as atmospheric ones. In particular, Haupt and Kant (1976) indicate that the Norwegian Sea ice conditions are greatly affected by the particular atmospheric circulation pattern over the Arctic and its influence on the exchange or non-exchange between the waters of the Beaufort Gyre and the Transpolar Drift Stream.

Since the numerical model developed here (Chapter IV) employs only mean monthly atmospheric forcing, it is unable to simulate yearly ice differences reflecting differences in atmospheric conditions. This is one limitation of the model which can be eliminated by coupling with an atmospheric model. In the meantime, a small experiment is performed in this section to illustrate the model sensitivity to the particular atmospheric temperatures used as input. Specifically, the experiment uniformly raises all Arctic temperatures by 5 K.

Naturally, the effect on the ice of an increase in atmospheric temperatures is to decrease both thickness and extent (Figure 52). By year 3 the thickest January ice is just under 1 m and the thickest July ice is on the order of 0.3 m.

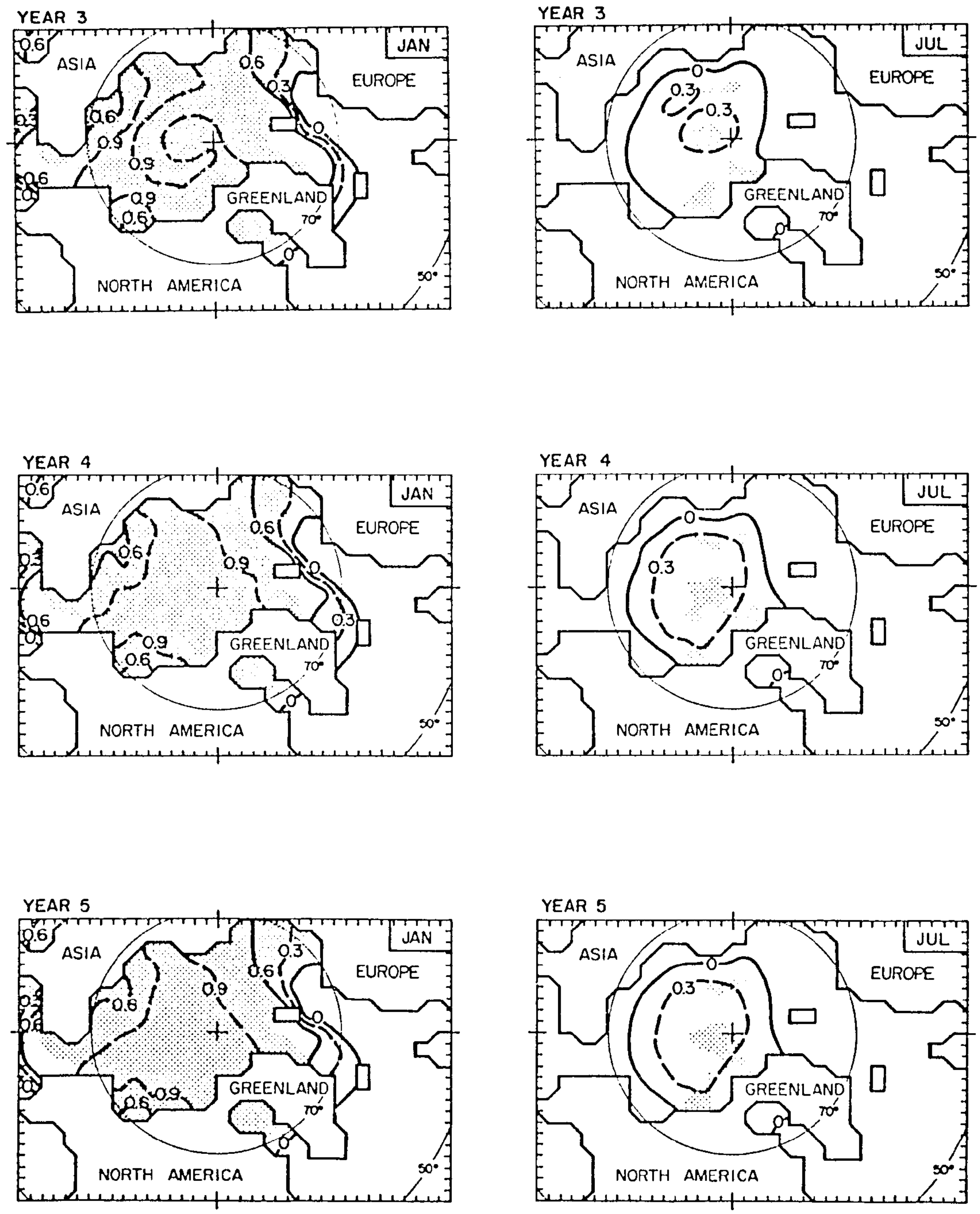

Figure 52. Simulated January and July ice thicknesses in the Arctic after increasing all atmospheric temperatures by 5 K. Contours show thickness in meters, while shading indicates ice compactness above 90%.

The ice totally disappears in August of the third year though in neither of the two previous years. It reemerges in October and, interestingly, by January of year 4 has become slightly thicker than in January of year 3. The July plots also show a thickening of the ice between years 3 and 4, with the 0.3 m contour extending further outward, as well as an increased ice concentration. The simulation appears to be near an equilibrium, as the plots for years 4 and 5 are extremely close and in each of years 3-5 there is an ice-free Arctic during August and September, with the ice cover reestablishing itself for the remainder of the year.

Clearly a 5 K increase in atmospheric temperatures causes a significant reduction in ice thicknesses and extents (Figure 52 *versus* Figure 33). However, the experiment also shows that a vanishing of the ice cover at the end of summer does not prevent the reestablishment of the ice the following winter.

CHAPTER VIII

SUMMARY AND CONCLUSIONS

This study has described the construction of a numerical model of the growth and decay of sea ice and has compared the results of the model against observations. Selected additional cases have been run to indicate the model sensitivity to individual parameterizations. In this final chapter, summaries of the model and model results are made as well as comments on its limitations and potentials.

8.1 Model Summary

8.1.1 Thermodynamics

Ice accretion and ablation are determined by energy balances at the various interfaces. With no ice, the net energy flux into the mixed oceanic layer,

$$Q_{net} = H{\downarrow} + LE{\downarrow} + \varepsilon_w LW{\downarrow} + (1-\alpha_w)SW{\downarrow} + F_w{\uparrow} - \varepsilon_w \sigma T_w^{\,4}, \quad (79)$$

is used to alter the ocean temperature T_w:

$$\Delta T_w = \Delta t \times \frac{Q_{net}}{d_{mix} \times c_w} . \quad (80)$$

Should this temperature fall below freezing, a portion of the water is frozen to ice.

With snow-less ice, the surface energy balance

$$H\downarrow + LE\downarrow + \varepsilon_I LW\downarrow + (1-0.4I_o)(1-\alpha_I)SW\downarrow - \varepsilon_I \sigma T_{sfc}^{\ 4} + \frac{k_I}{h_I}(T_B - T_{sfc}) = 0 \quad (81)$$

is linearized by setting $T_{sfc} = T_p + \Delta T$ and approximating $(T_p+\Delta T)^4$ by $T_p^{\ 4}+4T_p^{\ 3}\Delta T$. The linearized equation is solved for ΔT, after which ice is melted in the event of a surface temperature (T_{sfc}) above freezing and snow is allowed to fall in the event of a surface temperature below freezing. The amount of ice melt preserves an energy balance while maintaining a freezing temperature. Similarly, an energy balance at the undersurface of the ice determines ablation or accretion there:

$$\Delta h_I = \frac{\Delta t}{Q_I} \left[\frac{k_I}{h_I} (T_B - T_{sfc}) - F\uparrow \right] . \quad (82)$$

Snow-covered ice yields an energy balance at the snow surface of:

$$H\downarrow + LE\downarrow + \varepsilon_s LW\downarrow + (1-\alpha_s)SW\downarrow - \varepsilon_s \sigma T_{sfc}^{\ 4} + \frac{k_s}{h_s}(T_I - T_{sfc}) = 0 \quad (83)$$

and an energy balance at the snow-ice interface of:

$$\frac{k_s}{h_s}(T_I - T_{sfc}) = \frac{k_I}{h_I}(T_B - T_I) . \quad (84)$$

After replacing T_{sfc} by $T_p + \Delta T$ and linearizing as in the case of ice with no snow, these equations are solved for ΔT and T_I. Snow melt is calculated in the event of a surface temperature

T_{sfc} above freezing and snowfall is allowed in the event of a temperature equal to or below freezing. Ablation or accretion at the bottom of the ice is calculated through equation (82), with the temperature at the ice-snow interface, T_I, replacing T_{sfc}.

For operationalizing these energy balances, the sensible and latent heat fluxes at the surface are determined by bulk aerodynamic formulae, while the incoming longwave and shortwave radiative fluxes are determined by empirical formulae of Idso and Jackson (1969) and Zillman (1972) respectively. Details are presented in Chapter IV, where values are also given for all constants and variables in equations (79)-(84).

8.1.2 Water Temperatures and Leads

Each grid square has a percentage A of its area assumed ice-free, and hence the water in a grid square can be divided into two categories: water underneath the ice and water within the lead regions. These water categories have temperatures $T_{w'}$, and T_w respectively.

Ice melt affects $T_{w'}$, by mixing the melt water, at an assumed temperature of 271.2 K, into the mixed layer under the ice. The modeled mixed layer is a uniform 30 m deep, and any exchange of energy with the deeper ocean is ignored. Ocean temperatures are additionally affected by the net vertical energy input into the leads. This amount, per unit horizontal area, is

$$Q_o = \Delta t \times [(1-\alpha_w) SW{\downarrow} + H{\downarrow} + LE{\downarrow} + \varepsilon_w LW{\downarrow} - \varepsilon_w \sigma T_w^4] \ . \tag{85}$$

In the case of a positive Q_o, the energy excess heats the water and laterally melts the ice:

$$\Delta T_w = \frac{A \times Q_o}{d_{mix} \times c_w} \tag{86}$$

$$\Delta A = \frac{(1-A) \times A \times Q_o}{Q_I \times h_I + Q_S \times h_s} \ . \tag{87}$$

Should the resulting lead percentage exceed 100%, adjustments are made through a further increase in the water temperature.

In the alternate case of a negative Q_o, the energy deficit is balanced by a cooling of the lead temperature:

$$\Delta T_w = \frac{Q_o}{d_{mix} \times c_w} \ . \tag{88}$$

If this calculation gives rise to a water temperature below freezing, then the temperature remains at freezing and ice is laterally accreted onto the existing ice, again with an amount satisfying an energy balance. The model also includes a partial mixing between the water under the ice and the water in the leads.

8.1.3 Ice Dynamics

Determination of ice transport proceeds in two steps. First, a steady-state velocity of the ice is calculated by balancing wind stress, water stress, Coriolis force, and the stress from the tilt of the sea surface. These stresses are given the following formulations:

$$\vec{\tau}_a = \alpha\ C_D \rho_a\ V_{wg}^{\ 2}\ (\cos\beta\ \vec{i} + \sin\beta\ \vec{j}) \tag{89}$$

$$\vec{\tau}_w = \rho_w \sqrt{k_w \times |f|}\ \vec{V}_R \tag{90}$$

$$\vec{D} = \rho_i h_I f \vec{V}_i \times \vec{k} \tag{91}$$

$$\vec{G} = -\frac{10\rho_i h_I}{2H}\{[DT(I+1,J)-DT(I-1,J)]\vec{i}+[DT(I,J+1)-DT(I,J-1)]\vec{j}\}\ . \tag{92}$$

Second, the velocity field produced by the balance of the above four stresses is modified where necessary due to excess ice convergence. In effect, the modeled internal ice resistance decreases ice velocities to prevent ice coverage in any grid square from exceeding 98% in the southern hemisphere or 99.5% in the northern hemisphere.

8.2 Model Results

The numerical model summarized in section 8.1 and presented in detail in Chapter IV has simulated a reasonable yearly cycle of sea ice extent in both the Arctic and Antarctic (Chapter V). The large-scale features correspond well with those observed and estimated. In the Arctic, the ice grows from a minimum in September, when the edge has retreated from most coastlines, to a maximum in March, when the ice has reached well into the Bering Sea, has blocked the north coast of Iceland, and has moved southward of the southernmost tip of Greenland. Maximum Arctic thicknesses are roughly 3.7 m. In the Antarctic, the ice expands from a minimum in March to a maximum in late August, remaining close to the continent in the former month and expanding northward of $60^{\circ}S$ in the latter month. Maximum thicknesses are about 1.4 m.

Modeled ice concentrations reveal a more compact ice cover in the northern hemisphere than in the southern, corresponding correctly with qualitative observations. Winter ice concentrations exceed 97% for the entire Arctic basin, though the 97% contour has moved well into the Central Arctic region during the summer months. In the Antarctic, regions of summer ice concentrations above 97% are almost nonexistent, while in the winter the 97% contour has moved to within roughly 500 km of the ice edge.

Modeled ice velocities in the Arctic obtain both the Beaufort Sea Gyre and the Transpolar Drift Stream in summer as well as the Transpolar Drift Stream and the East Greenland Drift in winter. Simulated Antarctic ice vectors reveal predominantly westerly motion north of $58^{\circ}S$, with smaller scale cyclonic motions closer to the continent.

As model parameterizations are altered, the model results naturally change also. This has been illustrated by a few experiments examined in Chapter VII. As seen there, eliminating ice dynamics decreases the overall ice extent though has little effect on ice thickness. Thicknesses can be reduced/increased by several methods, among them an increase/decrease in either the oceanic heat flux or the atmospheric temperatures. Either of these alterations also reduces/increases ice extent, though in the case of the oceanic heat flux the effect on extent is much less than that on thickness.

8.3 Model Limitations and Future Potentials

Although large-scale features of the simulated results correspond nicely with observations in both hemispheres, the model retains many simplifications which limit its accuracy. In addition to obvious built-in restrictions such as the uniformity of ice thickness over a 200 km × 200 km grid square (with allowance for leads), the model is further limited in ways preventing its current application to many specific concerns regarding sea ice. Major among the sources of these limitations is the use of mean monthly atmospheric forcing. As emphasized in sections 5.1 and 7.4, there exist significant year-to-year variations in ice extent in both the Arctic and Antarctic. By employing a constant yearly cycle of atmospheric conditions, the present numerical model is unable to simulate such real-world interannual variability.

Equally important, the use of mean monthly averages smoothes out the temperature and wind extremes, both of which can be important in creating anomalous local conditions which can persist and expand in influence over time. For instance, large *polynyas* often open during intense storms (Vowinckel, 1966; Knapp, 1972), and a concentrated ice pack will sometimes remain motionless until the wind stress becomes untypically large (Pritchard, 1976). The use of mean winds prevents a proper simulation of such occurrences. Similarly, mean temperatures eliminate the short but sometimes significant melting periods accompanying anomalously warm conditions.

To further complicate matters in the case of the wind input, the use of averaged wind vectors does not produce averaged wind speeds, as opposing wind directions partially cancel. Thus the wind speeds specified in the model are particularly unrealistic in regions without dominant wind directions within the individual months.

Although the use of mean monthly averages is likely the largest source of error for calculations at the upper surface of the ice, there exist other error sources, including the use of constants for certain terms known to vary with atmospheric stability, winds, and/or temperatures. Perhaps the major such terms are the drag coefficient and the coefficients of sensible and latent heat exchange. The errors in each of these three coefficients, however, might be overpowered by the errors in the wind factor. Furthermore, as the AIDJEX experiment has amply shown, the uncertainty in these coefficients is great and any precise calculation with our averaged atmospheric data has no assurance of increasing the accuracy of the values.

In addition to the atmospheric simplifications, oceanic simplifications of the present model also prevent precise correspondence between simulated results and real-world ice configurations. For instance, ocean salinity is not modeled and the spatial variations of salinity are not included, although, among other consequences, the salinity affects the freezing temperature and the density of the water. Relatedly, the use of a constant mixed-layer depth ignores the influence of ocean convection, which is tied closely to the mutual interrelatedness of the freezing and melting of the ice on the one hand and the properties of the mixed oceanic layer on the other. Clearly the failure to include salinity and a variable mixed-layer depth restrict the ability of the model to simulate in precise detail the freeze-melt cycle.

Many of the current restrictions of the model can be eliminated upon coupling with atmospheric and oceanic models. A full atmospheric model will allow calculation of winds, air temperatures, and dew points on a timestep basis instead of the current use of monthly means, and a full oceanic model will allow a variable mixed layer, interaction with the deeper ocean and adjacent river and oceanic flows, calculation of the changing salinity field, and determination of the underlying oceanic circulation. Year-to-year variations should then be reproducible, and analyses of the mutual interaction of air, sea, and ice will become possible. Any contribution that such a coupled model could make to understanding the effect of ice on atmospheric circulation would be valuable.

It has been speculated that variations in the extent of the ice cover likely have considerable influence on the atmosphere well beyond the polar regions and that changes in the atmosphere can have considerable influence on the ice. In spite of the necessary cautions against placing too much faith in the outputs of a numerical model, such a model does have possibilities currently unattainable by other means. For example, in a model the effects of large-scale alterations can be tested, something not only unrealistic but also, at this stage, undesirable in the real world.

Besides the improvements and potential possible through coupling the sea-ice model with other numerical models, improvements are also needed from observational and theoretical studies on a smaller scale. Certainly the final analysis, now being carried out, of the AIDJEX data from the Beaufort Sea could be of value. Similarly, deeper understanding can be expected after the detailed temperature and salinity measurements planned by ISOS (International Southern Ocean Studies) in the Drake Passage. These studies will also monitor the development and deepening of the oceanic mixed layer. Another useful study now in progress is a collection of detailed data on the energy budget over sea ice and open water at Mawson, Antarctica (Allison and Akerman, 1977). The program envisions analyses of year-round measurements, though preliminary results are so far available only for fluxes over open water during February (see section 6.3 above). Along with the large-scale information available from satellites, such local studies are greatly improving our sea-ice data base.

The combination of observational studies, theoretical analyses, and numerical modeling can eventually lead to a much fuller understanding of Arctic and Antarctic sea ice and of its role in the global climatic system.

APPENDIX

SATELLITE CAPABILITIES

As with many other variable large-scale distributions on the earth's surface, the mapping of sea ice can be considerably aided by satellite observations. These do have limitations, however, and hence cannot themselves provide a full picture. This appendix attempts to indicate the abilities and potentials of satellite imagery related to polar sea ice. Much of the information is from a 1976 Symposium on Meteorological Observations from Space, at which, among others, E. P. McClain discussed variables measurable from current and planned earth satellites and J. R. Greaves specifically discussed the capabilities of the upcoming NASA satellites Nimbus-G and Seasat-A, both scheduled for launching in 1978.

The presence or absence of sea ice on 50 km and 100 km space resolutions has been obtainable since 1965 with the visible and thermal infrared sensors on NOAA satellites. Cloudiness limits the accuracy, though methods to filter out clouds are available (McClain, 1976). Sea surface temperature is now measurable to 2 K rms by the NOAA Scanning Radiometer (SR) and is expected to be measurable to 1.5 K rms by the Scanning Multi-Frequency Microwave Radiometer (SMMR) on

Nimbus-G and Seasat-A (Greaves, 1976). These figures compare with the desired accuracy of 0.5-1.5 K specified by the coordinators of the First GARP Global Experiment (FGGE). FGGE documents have also listed a desired accuracy of 1 K on a 100 km resolution for the surface temperature of the ice (McClain, 1976).

Both visual and infrared sensors on existing satellites are able to distinguish between open water, thin ice (i.e., less than about 0.5 m in thickness), and thick ice at 1 km resolution (McClain, 1976). New and old ice can be distinguished since old sea ice has a lower emissivity (due to the draining away of brine) and a stronger decrease of emissivity with frequency. Using the scanning microwave spectrometer (SCAMS) on the Nimbus-6, which maps at frequencies of 22.235 GHz and 31.400 GHz, this decrease can be obtained from $T_{B31.4} - T_{B22.235}$ (Fisher *et al.*, 1976). However, no satellite sensor is yet able to make direct measurements of ice thickness, and hence none can meet the FGGE specifications of a desired 10-20% accuracy in sea ice thickness on a 200 km resolution (McClain, 1976). The high-resolution Synthetic Aperture Radar (SAR) planned for the Seasat-A satellite should be valuable for ice thickness observations; however, the Seasat-A orbit has a very limited spatial coverage in polar regions (McClain, 1976).

It is anticipated that in the near future instrumentation will be available to meet the FGGE specifications of determining the presence or absence of melting on a 50 km resolution. Such measurements are obtainable because of the large decrease in near-infrared albedo when melt water appears at the ice surface. LANDSAT currently obtains some melt information, and the NOAA polar orbiters should be able to do so shortly (McClain, 1976).

Although current satellites are not capable of obtaining accurate wind speed and wind stress information over the oceans, this should be obtainable in 1978 with the Seasat-A satellite through use of a microwave scatterometer and the SMMR (McClain, 1976). The scatterometer will measure wind speeds by sensing the waves induced by the wind. This should be accurate to $\pm$ 2 m s^{-1} for wind speeds of 2-20 m s^{-1} (Greaves, 1976). Anticipated instrumentation improvements over the next decade would lead to wind speed accuracies of 1 m s^{-1} (McClain, 1976). With Seasat-A it is also hoped that dynamic topography will be measurable to within 0.2 m over an 18 km grid (McClain, 1976).

Satellite tracking of individual icebergs in Antarctica and the Labrador ice stream have been accomplished through Very High Resolution Radiometer (VHRR) imagery, but there has not been and there are no plans for large-scale documentation of sea ice drift. The 20-30 km resolution of microwave imagers is too coarse, while the Seasat-A's SAR will have the resolution but an orbit with far too limited a spatial coverage. On the other hand, present satellites are capable of tracking individual icebergs with emplaced transmitters (McClain, 1976). VHRR imagery has also been used in the Bering Sea area (Muench and Ahlnas, 1976) where a 1 km resolution has allowed tracking of individual floes as well as monitoring of the general ice distribution. However, newly-formed ice is not easily distinguished from open water (Muench and Ahlnas, 1976).

Maps of percent ice coverage have been plotted weekly from data of Electrically Scanning Microwave Radiometers (ESMR) on Nimbus 5 and Nimbus 6. Although the resolutions do not generally allow siting of individual ice floes and leads, the average ice coverage over a $2.5^{o} \times 2.5^{o}$ area is roughly obtainable owing to the wide difference in microwave emissivities of sea ice *versus* open water. The method is approximate, assuming the observed brightness temperature T_B to be the linear combination

$$T_B = \varepsilon_I T_o C + (\varepsilon_w T_w + A)(1 - C) \ , \qquad (93)$$

where C is the ice concentration, ε_I and ε_w are the ice and water emissivities, T_o and T_w are the ice and water temperatures, and A is the atmospheric brightness temperature. At the Nimbus 5 instrument wavelength of 15.5 mm, values of $\varepsilon_w T_w$, A, and $\varepsilon_I T_o$ can be approximated at 120 K, 15 K, and 250 K respectively, and then equation (93) can be solved immediately for C. Errors are clearly involved, among the largest being that ε_I varies with ice type and there is no independent measurement of T_o. However, it is felt that this method can determine C to an accuracy of $\pm$ 15% in regions, such as most of the Antarctic, where the ice is largely first-year ice (Zwally *et al.*, 1976). Due to measuring at the 15.5 mm wavelength rather than in the visible region, the ESMR imagery is not affected by the predominant clouds at high latitudes, these being clouds of low liquid-water content (Ackley and Keliher, 1976).

The Analysis Branch of the National Environmental Satellite Service of NOAA prepares weekly maps of northern hemisphere snow and ice boundaries based on visible and infrared satellite imagery from the Scanning Radiometer (SR) and the Very High Resolution Radiometer (VHRR) of the NOAA 4 satellite. In preparing the maps from satellite images, ice is distinguished from clouds subjectively by experienced analysts. The precision of the maps is estimated at 20-50 km (Kukla, 1976). Since 1973 the U. S. Navy has also prepared weekly charts of sea ice based on visual interpretation of images from NOAA and DOD satellites, along with cross-checking by plane and ship observations. Summer analysis uses visible and infrared SR images, while winter analysis uses SR images with 15.5 mm wavelength. The Navy maps present ice concentration (in octas) as well as ice extent (Kukla, 1976).

The theory behind the interpretation of satellite observations is by no means complete. Thus one should be cautious in reading present outputs and in expecting too much from future developments. Since the emission from ice depends on various aspects of subsurface structure as well as on the actual temperature and emissivity at the surface, brightness temperatures cannot be immediately reduced to surface temperatures. Work is proceeding to sort out the various influences and some hope exists that in the future satellite images will be able to reveal not only surface temperature but ice density, brine pocket sizes and frequency, salinity, and age (Fisher *et al.*, 1976).

LIST OF REFERENCES

Ackley, S. F. and T. E. Keliher, 1976: Antarctic sea ice dynamics and its possible climatic effects. *AIDJEX Bulletin No. 33*, 53-76.

Allison, I., 1973: A sample study of the energy fluxes preceding and accompanying the formation of Antarctic sea ice. *Energy Fluxes Over Polar Surfaces*. WMO Technical Note 129, 115-132.

Allison, I. and G. Akerman, 1977: Sea ice and ocean energy balance studies at Mawson, Antarctica. *A Symposium on Sea Ice Processes and Models September 6-9, 1977*, vol. II, University of Washington, Seattle, 137-146.

Badgley, F., 1961: Heat balance at the surface of the Arctic Ocean. *Proceedings of the Western Snow Conference*, Spokane, Washington.

Badgley, F., 1965: Heat balance at the surface of the Arctic Ocean. *U.S. - I.G.Y. Drifting Station Alpha, Arctic Ocean 1957-1958*, compiled by G. Cabaniss, K. Hunkins, and N. Untersteiner. Air Force Cambridge Research Laboratories, Bedford, Massachusetts, 69-79.

Badgley, F. I., 1966: Heat budget at the surface of the Arctic Ocean. *Proceedings of the Symposium on the Arctic Heat Budget and Atmospheric Circulation*, ed. by J. O. Fletcher, 267-277.

Baker, D. J., Jr., ed., 1976: *The Polar Sub-Programme of the Global Atmospheric Research Programme*. Department of Oceanography, University of Washington, Seattle, 97 pp.

Banke, E. G. and S. D. Smith, 1975: Measurement of form drag on ice ridges. *AIDJEX Bulletin No. 28*, 21-27.

Blindheim, J. and R. Ljoen, 1972: On the hydrographic conditions in the West Spitsbergen Current in relation to ice distribution during the years 1956-1963. *Sea Ice: Proceedings of an International Conference Reykjavik, Iceland May 10-13, 1971*, ed. by T. Karlsson, National Research Council of Iceland, Reykjavik, 33-41.

Brooks, C. E. P., 1949: *Climate Through the Ages*, McGraw-Hill, N. Y., 383 pp.

Brown, C. B., 1976: Interaction of pack ice with structures and associated ice mechanics. *AIDJEX Bulletin No. 34*, 207-242.

Bryan, K., S. Manabe, and R. C. Pacanowski, 1975: A global ocean-atmosphere climate model. Part II. The oceanic circulation. *Journal of Physical Oceanography*, 5, 30-46.

Budd, W. F., 1975: Antarctic sea-ice variations from satellite sensing in relation to climate. *Journal of Glaciology*, 15, 417-427.

Budyko, M. I., 1972: The future climate. *EOS, Transactions of the American Geophysical Union*, 53, 863-874.

Bushuyev, A. V., N. A. Volkov, Z. M. Gudkovich, and V. S. Loshchilov, 1970: Results of expedition investigations of the drift and dynamics of the ice cover of the Arctic Basin during the spring of 1961. *AIDJEX Bulletin No. 3*, 1-21.

Campbell, W. J., 1964: *On the Steady-State Flow of Sea Ice*. Department of Atmospheric Sciences, University of Washington, Seattle. Scientific Report to the Office of Naval Research under contract NR 207-352, 167 pp.

Campbell, W. J., 1968: Sea-ice dynamics. *Arctic Drifting Stations: A Report on Activities Supported by the Office of Naval Research.* Arctic Institute of North America, 189-196.

Coachman, L. K., 1966: Production of super-cooled water during sea ice formation. *Proceedings of the Symposium on the Arctic Heat Budget and Atmospheric Circulation*, ed. by J. O. Fletcher, 497-530.

Coachman, L. K. and K. Aagaard, 1974: Physical oceanography of Arctic and sub-Arctic seas. *Arctic Geology and Oceanography*, ed. by H. Nelson and Y. Herman. Springer-Verlag, 1-72.

Coon, M. D., R. Colony, R. S. Pritchard, and D. A. Rothrock, 1976: Calculations to test a pack ice model. *Numerical Methods in Geomechanics*, II, ed. by C. S. Desai, American Society of Civil Engineers, N. Y., 1210-1227.

Coon, M. D., G. A. Maykut, R. S. Pritchard, D. A. Rothrock, and A. S. Thorndike, 1974: Modeling the pack ice as an elastic plastic material. *AIDJEX Bulletin No. 24*, 1-105.

Crutcher, H. L. and J. M. Meserve, 1970: *Selected Level Heights, Temperatures and Dew Points for the Northern Hemisphere.* NAVAIR 50-1C-52 Revised, Naval Weather Service Command, Washington, D. C.

Daniel, H. C., 1957: *Oceanographic Atlas of the Polar Seas, Part I, Antarctic.* U. S. Navy Hydrographic Office, H. O. Pub. No. 705, Washington, D. C., 70 pp.

Dansgaard, W., S. J. Johnsen, H. B. Clausen, and N. Gundestrup, 1973: Stable isotope glaciology. *Meddelelser om Grönland,* 197, 53 pp.

Donn, W. L., 1975: *Meteorology,* 4th Edition, McGraw-Hill, New York, 518 pp.

Donn, W. L. and D. M. Shaw, 1966: The heat budgets of an ice-free and an ice-covered Arctic Ocean. *Journal of Geophysical Research,* 71, 1087-1093.

Doronin, Yu. P., 1970: On a method of calculating the compactness and drift of ice floes. *AIDJEX Bulletin No. 3,* 22-39.

Doronin, Yu. P., 1970: *Thermal Interaction of the Atmosphere and the Hydrosphere in the Arctic.* Translated from Russian, Israel Program for Scientific Translations, Jerusalem, 244 pp.

Ekman, V. W., 1905: On the influence of the earth's rotation on ocean currents. *Arkiv. f. Matem., Astr. o. Fysik* (Stockholm) 2, 11, 53 pp.

Ewing, M. and W. L. Donn, 1956: A Theory of ice ages. *Science,* 123, 1061-1066.

Ewing, M. and W. Donn, 1958: A theory of ice ages, 2. *Science,* 127, 1159-1162.

Farhadieh, R. and R. S. Tankin, 1975: A study of the freezing of sea water. *Journal of Fluid Mechanics,* 71, 293-304.

Felzenbaum, A. I., 1958: The theory of the steady drift of ice and the calculation of the long period mean drift in the central part of the Arctic basin. *Problems of the North,* 2, 5-44.

Fisher, A. D., B. L. Ledsham, P. W. Rosenkranz, and D. H. Staelin, 1976: Satellite observations of snow and ice with an imaging passive microwave spectrometer. *Proceedings of the Symposium on Meteorological Observations from Space: Their Contribution to the First GARP Global Experiment.* Held June 8-10 at Philadelphia in conjunction with the 19th meeting of COSPAR (Committee on Space Research of the International Council of Scientific Unions), 98-103.

Fletcher, J. O., 1965: *The Heat Budget of the Arctic Basin and Its Relation to Climate.* The Rand Corporation, Santa Monica, California, R-444-PR, 179 pp.

Fletcher, J. O., 1969: *Ice Extent on the Southern Ocean and Its Relation to World Climate.* Memorandum RM-5793-NSF, March, Rand Corporation, Santa Monica, California, 108 pp.

Gloersen, P. and V. V. Salomonson, 1975: Satellites - new global observing techniques for ice and snow. *Journal of Glaciology,* 15, 373-389.

Gordienko, P., 1958: Arctic ice drift. *Proceedings of the Conference on Arctic Sea Ice,* Publication 598. National Academy of Sciences and National Research Council, Washington, D.C., 210-222.

Greaves, J. R., 1976: Surface characteristics observable from experimental satellites during FGGE. *Proceedings of the Symposium on Meteorological Observations from Space: Their Contribution to the First GARP Global Experiment.* Held June 8-10 at Philadelphia in conjunction with the 19th meeting of COSPAR (Committee on Space Research of the International Council of Scientific Unions), 87-88.

Hall, R. T., G. A. Maykut, and D. A. Rothrock, 1976: Sea ice modeling: its testing with LANDSAT and potential use in FGGE. *Proceedings of the Symposium on Meteorological Observations from Space: Their Contribution to the First GARP Global Experiment.* Held June 8-10 at Philadelphia in conjunction with the 19th meeting of COSPAR (Committee on Space Research of the International Council of Scientific Unions), 104-109.

Haltiner, G. J. and F. L. Martin, 1957: *Dynamical and Physical Meteorology.* McGraw-Hill Book Company, Inc., New York, 470 pp.

Haupt, I. and V. Kant, 1976: Satellite ice surveillance studies in the Arctic in relationship to the general circulation. *Proceedings of the Symposium on Meteorological Observations from Space: Their Contribution to the First GARP Global Experiment.* Held June 8-10 at Philadelphia in conjunction with the 19th meeting of COSPAR (Committee on Space Research of the International Council of Scientific Unions), 179-187.

Heap, J. A., 1972: International co-operation in sea ice observing, recording and reporting. *Sea Ice: Proceedings of an International Conference Reykjavik, Iceland May 10-13, 1971,* ed. by T. Karlsson, National Research Council of Iceland, Reykjavik, 80-83.

Herman, G., 1975: *Radiative-Diffusive Models of the Arctic Boundary Layer.* Department of Meteorology, Massachusetts Institute of Technology, Cambridge, Massachusetts, 170 pp.

Hess, S. L., 1959: *Introduction to Theoretical Meteorology.* Holt, Rinehart and Winston, New York, 362 pp.

Hibler, W. D. III, 1977: Modeling pack ice as a viscous-plastic continuum: some preliminary results. *A Symposium on Sea Ice Processes and Models September 6-9, 1977,* vol. II, University of Washington, Seattle, 46-55.

Hibler, W. D. III, W. B. Tucker, and W. F. Weeks, 1976: Techniques for using LANDSAT imagery without land references to study sea ice drift and deformation. *AIDJEX Bulletin No. 31,* 115-135.

Holmgren, B. and G. Weller, 1973: *Studies of the Solar and Terrestrial Radiation Fluxes over Arctic Pack Ice.* Final Report (Technical Report No. 3), Geophysical Institute, University of Alaska, Fairbanks, Alaska. Advanced Research Projects Agency of the Department of Defense, Contract No. N00014-71-A-0364-0001, 25 pp.

Hughes, T., 1973: Is the West Antarctic Ice Sheet disintegrating? *Journal of Geophysical Research,* 78, 7884-7910.

Hughes, T., 1974: Study of unstable Ross Sea glacial episodes. *Ice Stability Coordinated Antarctic Program Bulletin No. 3.* Institute for Quaternary Studies, University of Maine at Orono, 93 pp.

Humphreys, W. J., 1964: *Physics of the Air,* Dover Publications, Inc., New York, 676 pp.

Hunkins, K., 1966: Ekman drift currents in the Arctic Ocean. *Deep-Sea Research,* 13, 607-620.

Hunkins, K., 1974: The oceanic boundary layer and ice-water stress during AIDJEX 1972. *AIDJEX Bulletin No. 26*, 109-127.

Huschke, R. E., 1959: *Glossary of Meteorology*. American Meteorological Society, Boston, Massachusetts, 638 pp.

Huschke, R. E., 1969: *Arctic Cloud Statistics from 'Air-Calibrated' Surface Weather Observations*. The RAND Corporation Memorandum RM-6173-PR, Santa Monica, California, 79 pp.

Idso, S. B. and R. D. Jackson, 1969: Thermal radiation from the atmosphere. *Journal of Geophysical Research*, 74, 5397-5403.

Jacobs, S. S., E. B. Bauer, P. M. Bruchhausen, A. L. Gordon, T. F. Root, and F. L. Rosselot, 1974: *Eltanin Reports, Cruises 47-50, 1971; 52-55, 1972*. Lamont-Doherty Geological Observatory of Columbia University, Palisades, New York, 503 pp.

Jenne, R. L., H. L. Crutcher, H. van Loon, and J. J. Taljaard, 1974: *A Selected Climatology of the Southern Hemisphere: Computer Methods and Data Availability*. NCAR Technical Note STR-92, 91 pp.

Kellogg, W. W., 1974: Meteorological observations in support of weather forecasting. *U. S. Contribution to the Polar Experiment (POLEX), Part 1: POLEX-GARP (North)*, National Academy of Sciences, Washington, D. C., 26-49.

Knapp, W. W., 1972: Satellite observations of large *polynyas* in polar waters. *Sea Ice: Proceedings of an International Conference Reykjavik, Iceland May 10-13, 1971*, ed. by T. Karlsson, National Research Council of Iceland, Reykjavik, 201-212.

Ku, T. and W. S. Broecker, 1967: Rates of sedimentation in the Arctic Ocean. *Progress in Oceanography 4*, ed. by M. Sears, Pergamon, 95-104.

Kukla, G. J., 1976: Global variation of snow and ice extent. *Proceedings of the Symposium on Meteorological Observations from Space: Their Contribution to the First GARP Global Experiment.* Held June 8-10 at Philadelphia in conjunction with the 19th meeting of COSPAR (Committee on Space Research of the International Council of Scientific Unions), 110-115.

Laevastu, T., 1960: Factors affecting the temperature of the surface layer of the sea. Soc. Sci. Fennica Commentations. *Physical Mathematics*, 25, 1.

Lamb, H. H., 1966: *The Changing Climate*. Methuen, London, 236 pp.

Langleben, M. P., 1972: The decay of an annual cover of sea ice. *Journal of Glaciology*, 11, 337-344.

Lindsay, R. W., 1976: Wind and temperature profiles taken during the Arctic lead experiment. *AIDJEX Bulletin No. 33*, 102-104.

Manabe, S., K. Bryan, and M. J. Spelman, 1975: A global ocean-atmosphere climate model. Part 1. The atmospheric circulation. *Journal of Physical Oceanography*, 5, 3-29.

Marshunova, M. S., 1966: Principal characteristics of the radiation balance of the underlying surface and of the atmosphere in the Arctic. *Soviet Data on the Arctic Heat Budget and Its Climatic Influence*, ed. by J. O. Fletcher, B. Keller, and S. M. Olenicoff, 51-131.

Maykut, G. A., 1976: Energy exchange over young sea ice in the central Arctic. *AIDJEX Bulletin No. 31*, 45-74.

Maykut, G., 1977: Estimates of the regional heat and mass balance of the ice cover. *A Symposium on Sea Ice Processes and Models September 6-9, 1977*, vol. I, University of Washington, Seattle, 65-74.

Maykut, G. A. and A. S. Thorndike, 1973: An approach to coupling the dynamics and thermodynamics of Arctic sea ice. *AIDJEX Bulletin No. 21*, 23-29.

Maykut, G. A. and N. Untersteiner, 1969: *Numerical Prediction of the Thermodynamic Response of Arctic Sea Ice to Environmental Changes*. The RAND Corporation Memorandum RM-6093-PR. Santa Monica, California, 173 pp.

Maykut, G. A. and N. Untersteiner, 1971: Some results from a time-dependent thermodynamic model of sea ice. *Journal of Geophysical Research*, 76, 1550-1575.

McClain, E. P., 1976: Monitoring earth surface characteristics important to weather and climate with earth satellites. *Proceedings of the Symposium on Meteorological Observations from Space: Their Contribution to the First GARP Global Experiment.* Held June 8-10 at Philadelphia in conjunction with the 19th meeting of COSPAR (Committee on Space Research of the International Council of Scientific Unions), 129-135.

McPhee, M. G., 1977: An analysis of pack ice drift in summer. *A Symposium on Sea Ice Processes and Models September 6-9, 1977*, vol. I, University of Washington, Seattle, 240-250.

McPhee, M. G. and J. D. Smith, 1975: Measurements of the turbulent boundary under pack ice. *AIDJEX Bulletin No. 29*, 49-92.

Mercer, J. H., 1970: A former ice sheet in the Arctic Ocean. *Palaeogeography, Palaeoclimatology and Palaeoecology*, 8, 19-27.

Muench, R. D. and K. Ahlnas, 1976: Ice movement and distribution in the Bering Sea from March to June 1974. *Journal of Geophysical Research*, 81, 4467-4476.

Muller, E. H., 1972: Implication of an ice-free Polar Basin. *Sea Ice: Proceedings of an International Conference Reykjavik, Iceland May 10-13, 1971*, ed. by T. Karlsson. National Research Council of Iceland, Reykjavik, 112-117.

Murray, F. W., 1967: On the computation of saturation vapor pressure. *Journal of Applied Meteorology*, 6, 203-204.

Nansen, F., 1902: The oceanography of the north polar basin. *Norwegian North Pole Expedition, 1893-1896, Scientific Results*, 3, 357-386.

Neumann, G. and W. J. Pierson, Jr., 1966: *Principles of Physical Oceanography*. Prentice-Hall, Inc., Englewood Cliffs, N. J., 545 pp.

Nikiforov, E. G., Z. M. Gudkovich, Yu. N. Yefimov, and M. A. Romanov, 1970: Principles of a method for calculating the ice redistribution under the influence of wind during the navigation period in Arctic seas. *AIDJEX Bulletin No. 3*, 40-64.

Oliger, J. E., R. E. Wellck, A. Kasahara, and W. M. Washington, 1970: *Description of NCAR Global Circulation Model*. NCAR/ TN-56+ STR. National Center for Atmospheric Research, Boulder, Colorado, 94 pp.

Parkinson, C. L., 1974: Shortwave albedo over wavy water surfaces, master's paper, Ohio State University, unpublished.

Pease, C. H., 1975: A model for the seasonal ablation and accretion of Antarctic sea ice. *AIDJEX Bulletin No. 29*, 151-172.

Phillips, N. A., 1957: A map projection system suitable for large-scale numerical weather prediction. *Journal of the Meteorological Society of Japan*, 75, 262-267.

Pritchard, R. S., 1975: An elastic-plastic constitutive law for sea ice. *Journal of Applied Mechanics*, 42, 379-384.

Pritchard, R. S., 1976: An estimate of the strength of Arctic pack ice. *AIDJEX Bulletin No. 34*, 94-113.

Pritchard, R. S., M. D. Coon, and M. G. McPhee, 1976: Simulation of sea ice dynamics during AIDJEX. *AIDJEX Bulletin No. 34*, 73-93.

Ralston, T. D., 1977: Yield and plastic deformation in ice crushing failure. *A Symposium on Sea Ice Processes and Models September 6-9, 1977*. University of Washington, Seattle, vol. II, 147-156.

Reed, R. J. and W. J. Campbell, 1960: *Theory and observations of the drift of Ice Station Alpha*. Department of Meteorology, University of Washington, Seattle. Final report to the Office of Naval Research under contract NR 307-250, 255 pp.

Reed, R. J. and W. J. Campbell, 1962: The equilibrium drift of ice station Alpha. *Journal of Geophysical Research*, 67, 281-297.

Rigby, F. A. and A. Hanson, 1976: Evolution of a large Arctic pressure ridge. *AIDJEX Bulletin No. 34*, 43-71.

Rothrock, D. A., 1973: The steady drift of an incompressible Arctic ice cover. *AIDJEX Bulletin No. 21*, 49-77.

Schlatter, T. W., 1972: The local surface energy balance and subsurface temperature regime in Antarctica. *Journal of Applied Meteorology*, 11, 1048-1062.

Sellers, W. D., 1965: *Physical Climatology*. University of Chicago Press, Chicago, Illinois, 272 pp.

Semtner, A. J., 1976a: A model for the thermodynamic growth of sea ice in numerical investigations of climate. *Journal of Physical Oceanography*, 6, 379-389.

Semtner, A. J., Jr., 1976b: Numerical simulation of Arctic Ocean Circulation. *Journal of Physical Oceanography*, 6, 409-425.

Shuleikin, V. V., 1938: The drift of ice-fields. *Comptes Rendus (Doklady) de l'Acad. des Sci. de l'USSR*, 19, 589-594.

Smith, J. D. and T. S. English, 1974: Seasonal variations in density and depth of the mixed layer in the Arctic Ocean. *EOS, Transactions of the American Geophysical Union*, 55, 76.

Solomon, H., 1963: *Large-Scale Response of the Ocean to Sea Ice Formation.* Department of Meteorology, Massachusetts Institute of Technology, unpublished Ph.D. dissertation, 132 pp.

Sverdrup, H. U., M. W. Johnson, and R. H. Fleming, 1961: *The Oceans, Their Physics, Chemistry and General Biology.* Prentice-Hall, Inc., 1087 pp.

Swithinbank, C., 1972: Arctic pack ice from below. *Sea Ice: Proceedings of an International Conference Reykjavik, Iceland May 10-13, 1971,* ed. by T. Karlsson, National Research Council of Iceland, Reykjavik, 246-254.

Taljaard, J. J., H. van Loon, H. L. Crutcher, and R. L. Jenne, 1969: *Climate of the Upper Air, Part I. Southern Hemisphere, Vol. 1, Temperatures, Dew Points, and Heights at Selected Pressure Levels.* NAVAIR 50-1C-55, U. S. Naval Weather Service, Washington, D. C., 135 pp.

Thekaekara, M. P. and A. J. Drummond, 1971: Standard values for the solar constant and its spectral components. *Nature Physical Sciences,* 229, 6-9.

Thompson, L. G., 1977: Variations in microparticle concentration, size distribution, and elemental composition found in the Camp Century, Greenland, and the Byrd Station, Antarctica, deep ice cores. *Proceedings of a Symposium on Isotopes and Impurities in Snow and Ice, Grenoble, 1975.* International Union of Geodesy and Geophysics, International Association of Scientific Hydrology, Commission of Snow and Ice. (In press.)

Tolstikov, Ye. I., chief editor, 1966: *Atlas of Antarctica,* vol. I, Academy of Sciences, USSR, Moscow, 225 plates.

Tolstikov, Ye. I., chief editor, 1969: *Atlas of Antarctica,* vol. II, Academy of Sciences, USSR, Moscow.

Treshnikov, A. F., 1964: Surface water circulation in the Antarctic Ocean. *Soviet Antarctic Expedition Information Bulletin,* 5, 81-83.

Treshnikov, A. F., 1966: Water circulation and ice drift of the Southern Ocean. *Morning Review Lectures of the Second International Oceanographic Congress.* Held 30 May - 9 June at Moscow, 250-256.

Tucker, W. B. III and V. H. Westhall, 1973: Arctic sea-ice ridge frequency distributions derived from laser profiles. *AIDJEX Bulletin No. 21,* 171-180.

Untersteiner, N., 1964: Calculations of temperature regime and heat budget of sea ice in the central Arctic. *Journal of Geophysical Research*, 69, 4755-4766.

Untersteiner, N., 1975: Sea ice and ice sheets and their role in climatic variations. *GARP Publications Series No. 16, The Physical Basis of Climate and Climate Modelling*, 206-224.

U. S. Chief of Naval Operations, 1966: *Components of the 1000mb Winds (or Surface Winds) of the Northern Hemisphere*, Washington, D. C.

van Loon, H., 1972: Cloudiness and precipitation in the Southern Hemisphere. *Meteorological Monographs, vol. 13, Meteorology of the Southern Hemisphere*, ed. by C. W. Newton, American Meteorological Society, Boston, Massachusetts, 101-111.

Vowinckel, E., 1966: Some estimates about the size and variation of the Antarctic pack ice belt. Institute of Polar Studies Report No. 19, The Ohio State University, Columbus, Ohio, 20 pp.

Vowinckel, E. and S. Orvig, 1965a: Energy balance of the Arctic I. Incoming and absorbed solar radiation at the ground in the Arctic. *Archiv Für Meteorologie, Geophysik Und Bioklimatologie*, Series B, 13, 352-377.

Vowinckel, E. and S. Orvig, 1965b: Energy balance of the Artic II. Longwave radiation and total radiation balance at the surface in the Arctic. *Archiv Für Meteorologie, Geophysik Und Bioklimatologie*, Series B, 13, 451-479.

Vowinckel, E. and S. Orvig, 1966: Energy balance of the Arctic V. The heat budget over the Arctic Ocean. *Archiv Für Meteorologie, Geophysik Und Bioklimatologie*, Series B, 14, 303-325.

Vowinckel, E. and S. Orvig, 1970: The climate of the north polar basin. *World Survey of Climatology, Vol. 14, Climates of the Polar Regions*, ed. by S. Orvig, 129-252.

Vowinckel, E. and B. Taylor, 1966: Energy balance of the Arctic IV. Evaporation and sensible heat flux over the Arctic Ocean. *Archiv Für Meteorologie, Geophysik Und Bioklimatologie*, Series B, 14, 36-52.

Washington, W. M., A. J. Semtner, Jr., C. Parkinson, and L. Morrison, 1976: On the development of a seasonal change sea-ice model. *Journal of Physical Oceanography*, 6, 679-685.

Weber, J. E., 1977: Heat and salt transfer associated with formation of sea ice. *Tellus*, 29, 151-160.

Weeks, W. F., 1976a: Sea ice conditions in the Arctic. *AIDJEX Bulletin No. 34*, 173-205.

Weeks, W. F., 1976b: Sea ice properties and geometry. *AIDJEX Bulletin No. 34*, 137-171.

Welander, P., 1977: Thermal oscillations in a fluid heated from below and cooled to freezing from above. *Dynamics of Atmospheres and Oceans*, 1, 215-223.

Wilson, A. T., 1964: Origin of ice ages: an ice shelf theory for Pleistocene glaciation. *Nature*, 201, 147-149.

Wilson, C., 1969: *Climatology of the Cold Regions. Northern Hemisphere II.* Corps of Engineers, U. S. Army Cold Regions Research and Engineering Laboratory, Hanover, New Hampshire. Cold Regions Science and Engineering Monograph 1-A3b, 158 pp.

Winchester, J. W. and C. C. Bates, 1958: Meteorological conditions and the associated sea ice distribution in the Chukcki Sea during the summer of 1955. *Polar Atmosphere Symposium Part 1; Meteorology Section*, ed. by R. E. Sutcliffe, 323-334.

Wittmann, W. I. and J. J. Schule, Jr., 1966: Comments on the mass budget of Arctic pack ice. *Proceedings of the Symposium on the Arctic Heat Budget and Atmospheric Circulation*, ed. by J. O. Fletcher, 215-246.

Yakovlev, G. N., 1970: On relief forms of floating ice. *AIDJEX Bulletin No. 3*, 106-118.

Zillman, J. W., 1972: *A Study of Some Aspects of the Radiation and Heat Budgets of the Southern Hemisphere Oceans*. Meteorological Study No. 26, Bureau of Meteorology, Department of the Interior, Canberra, Australia, 562 pp.

Zubov, N. N., 1944: *Arctic Ice*, Moscow (translated by U. S. Navy Electronics Laboratory, 1963), 491 pp.

Zwally, H. J. and P. Gloersen, 1977: Passive microwave images of the polar regions and research applications. *Polar Record*, 18, 431-450.

Zwally, H. J., T. T. Wilheit, P. Gloersen, and J. L. Mueller, 1976: Characteristics of Antarctic sea ice as determined by satellite-borne microwave imagers. *Proceedings of the Symposium on Meteorological Observations from Space: Their Contribution to the First GARP Global Experiment.* Held June 8-10 at Philadelphia in conjunction with the 19th meeting of COSPAR (Committee on Space Research of the International Council of Scientific Unions), 94-97.